Università degli Studi di Udine

Dottorato di Ricerca in
Scienze dell'Ingegneria Energetica e Ambientale
XXX Ciclo - 2017

Direct numerical simulation of turbulence-interface interactions

Dr. Alessio Roccon

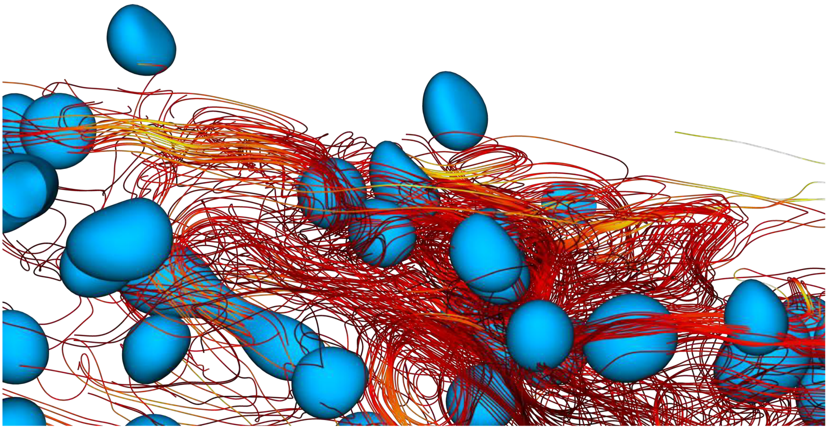

BOARD MEMBERS

Prof. Carlo Massimo Casciola	Reviewer
Prof. Hans Kuerten	Reviewer
Prof. Cristian Marchioli	Committee member
Prof. Matteo Bernardini	Committee member
Prof. Srdjan Sasic	Committee member
Prof. Alfredo Soldati	Supervisor
Prof. Alessandro Trovarelli	Doctorate Chair

Author's Web Page:
http://158.110.32.35/PEOPLE/Roccon.html

Author's e-mail:
roccon.alessio@spes.uniud.it
alessio.roccon@tuwien.ac.at

Author's address:
Dipartimento Politecnico di Ingegneria e Architettura
Università degli Studi di Udine
Via delle Scienze, 206
33100 Udine – Italia
mobile: +39 347 9599476
web: www2.diegm.uniud.it/diegm/

Last update:
Udine, February 9, 2018

Abstract

In this thesis, the interactions between a deformable interface and turbulence have been investigated using Direct Numerical Simulations (DNS). The interface and the surfactant concentration are tracked using a Phase Field Method (PFM). The turbulence-interface interactions have been analysed in two different flow configurations, a dispersed and a stratified flow.
First, a dispersed flow is considered, a swarm of large deformable drops is released in a turbulent channel flow. The coalescence and breakup rates have been characterised for different values of the surface tension and viscosity ratios. Results show that the drop size, determined by the equilibrium between coalescence and breakup, is influenced either by the surface tension, either by the internal viscosity. In particular, for small values of the surface tension values, the internal viscosity enhances the stability of the interface and prevent drop breakup.
Second, a viscosity stratified configuration is considered. This setup mimics a core annular flow; a low viscosity fluid is interposed between the core and the walls to decrease the pressure drop. Results show that the interface is able to damp the near-wall turbulence, an increase of the core flow rate is observed. For the range of viscosity ratios analysed, the turbulence-interface interactions play a key role for obtaining Drag Reduction (DR). The DR performance is slighty affected by the viscosity ratio.

Contents

Introduction

Turbulent multiphase flows are often encountered in enviroemntal and industrial applications. The different phases composing the mixture mutually interact through a deformable interface. With the aid of direct numerical simulations, the interplay between interface and turbulence has been analysed in different flow configurations.

Motivation

The understanding of turbulent behaviour in flowing fluids is one of the most important problem in all of classical physics. Turbulent flows involve non linear multi-scale phenomena which mutually interact.
When two or more phases, separated by an interface interact, the behaviour of the system can drastically change. The interface, and the linked boundary conditions that the flow must satisfied on it, modify the turbulent structures and vice versa. The induced modifications are directly linked to the thermophysical proprieties of the phases (density, viscosity and interfacial tension). The system behaviour becomes even more complex when the presence of surfactants is considered (amphiphilic compound adsorbed at liquid/gas or liquid/liquid interfaces). Surfactants are often present in real multiphase systems, as for example in the sea-surface micro layer [88] or in industrial applications [117]. Surfactants, decreasing the surface tension, alter the interface dynamics. In addition, an inhomogeneous surfactant distribution produces surface tension gradients and gives rise to tangential stresses at the interface.
Overall, the turbulence-interface-surfactant interactions play a crucial role in all the physical phenomena in which the exchange of momentum, heat, and/or chemical species through an interface is important [78, 150, 98].

Numerical simulations

Numerical simulations are a powerful tool to investigate turbulent multiphase flows. The last decade has seen the development of powerful computation capabilities which have marked a turning point in the field. When dealing with multiphase flows, major challenges arise in the development of numerical methods able to: (*i*) accurately model the momentum transfer between the two fluids, (*ii*) describe the shape and the position of the interface, (*iii*) track the surfactant concentration.

The description of the momentum transfer between the two fluids must consider steep variation of thermophysical properties across the interface and the relative boundary conditions applied on it. To this purpose, a continuous [20, 90, 136] or a sharp approach [55, 17, 101] can be adopted. In the continuous approach, forces and variations of material properties are smeared over a finite volume region across the interface using smoothed delta functions; in the sharp approach, the discontinuous nature of the changes are treated as moving boundaries. The approaches used to describe the shape and the position of the interface can be roughly divided in interface tracking and interface capturing methods. In the framework of the interface tracking methods, the interface is represented by a set of connected points advected by the flow [174, 173]. When interface capturing methods are considered, a colour function is used to mark the different phases, well-known approaches are Volume-Of-Fluid (VOF) [70, 63], Level-Set (LS) [129, 127], and Phase Field Method (PFM) [5, 10, 103]. To describe the surfactant concentration, different approaches have been proposed depending on the method used to represent the interface. Different techniques have been proposed for FT [187, 125], for LS [186, 189, 188] and for the PFM [104, 171].

In this work, the multiphase system is described performing Direct Numerical Simulations (DNS) of the Navier-Stokes equation coupled with a Phase Field Method (PFM) to track the interface and the surfactant concentration. The DNS technique is able to solve all the length and time scales involved in the turbulent flow, giving a complete and predictive description of the complex turbulent motions [123, 77, 92]. The PFM is a comprehensive theoretical framework able to efficently describe the behaviour of deformable interfaces. In particular the PFM is one of the most accurate method for the numerical analysis of breakup [139, 135] and coalescence [194, 46, 152, 142] phenomena. In addition, the PFM can be extended in a straightforward manner to consider a surfactant [168, 171]. Overall, the PFM is a powerful mathematical framework able to accurately describe the turbulence-interface-surfactant interactions.

Thesis outline

This thesis is organised as follows:

- Chap. 1: Methodology. The governing equations used to obtain the temporal and spatial evolution of the multiphase flow are derived. The phase field method is used to track the interface and the surfactant concentration. The flow field is obtained using a continuous approach and solving and opportunely modified Navier-Stokes equation. The numerical procedure used to discretise the equations is presented and the mathematical model is validated against literature benchmarks.

- Chap. 2: Breakup and coalescence of drops. The phase field method is used to analyse the dynamics of a swarm of large deformable drops released in a turbulent channel flow. Assuming a clean system, the effects of the surface tension and of the drop viscosity in the drop-drop and drop-turbulence interactions are studied. The behaviour of the coalescence and breakup rates are analysed for different values of the parameters.

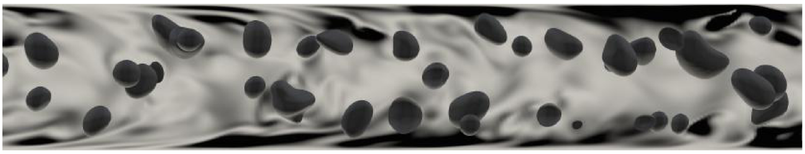

- Chap. 3: Interaction between surfactant-laden droplets. The effects of the surfactant on the droplet-droplet interaction have been analysed. Different surfactant concentrations and elasticity numbers have been considered. The increased deformability and the presence of tangential stresses at the interface can prevent the coalescence.

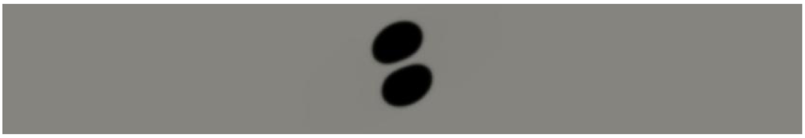

- Chap. 4: Viscosity stratified fluids in turbulent channel flow. A configuration in which a low viscosity thin layer flows on top of a thick fluid layer has been considered. The interactions between the deformable interface and the near-wall turbulence structures, together with the low viscosity of the thin layer, leads to an increase of the flow rate. Since the mean pressure gradient driving the flow is fixed, Drag Reduction (DR) is obtained.

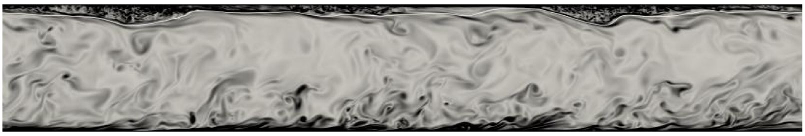

Chap. 2: Swarm of droplets released in a turbulent channel flow. Drops interface is coloured in dark grey.

Chap. 3: Surfactant-laden droplets interacting. The two droplets are driven towards collision by the shear flow.

Chap. 4: Viscosity stratified fluids in turbulent channel flow. A thin white line identifies the interface position. The contour map shows the Turbulent Kinetic Energy (TKE).

1

Methodology

Reproduced in part from:

G. Soligo, A. Roccon, and A. Soldati, Phase Field Method to predict coalescence of clean and surfactant-laden droplets, J. Comput. Phys., in preparation.

In the first part of this chapter, the numerical methods used to compute the flow field and to track the interface and the surfactant concentration are presented, Sec. 1.1 - 1.4. In the second part, the numerical schemes are derived and the implementation is validated, Sec. 1.5 - 1.6.

1.1 Interface tracking

The principal methods available to track the interface shape are briefly presented. They can be classified in two classes: (*i*) Interface tracking methods, the interface is described following the movement of a set of marker points (Front Tracking) (*ii*) Interface capturing methods, the two phases are identified by the value of a specific function which is advected by the flow (Volume Of Fluid, Level Set, Phase Field Method).

1.1.1 Front tracking

In the Front Tracking (FT) method, a set of marker points located at the interface is used to describe its shape. The points are advected by the flow and the position of the i-th marker point can be obtained solving the following equation:

$$\frac{\partial \mathbf{x}^i}{\partial t} = \mathbf{u}^i \tag{1.1}$$

Where $\mathbf{x}^i$ is the position vector of the i-th marker position and $\mathbf{u}^i$ is the velocity vector at the marker position. Once the new position is calculated, the shape of the front can be reconstructed. The interface is represented by elements connecting the marker points. From the connections, the curvature of the interface can be computed. Once is known, surface tension force can be computed and applied into the Navier-Stokes equation. This force is defined only on the marker points and has to be smeared out on the eulerian grid where the flow is solved (”smoothing” operation). This operation requires communications between the two grids (Lagrangian grid of the marker points and Eulerian grid of the fluid). This method has been proposed by [174, 173, 22] where bubbly flows were investigated. One of the main drawbacks is the low accuracy in the computation of the interface curvature. In addition, the method requires specific closure models when coalescence and/or breakage phenomena are present [138].

1.1.2 Volume of fluid

The main idea of the Volume Of Fluid (VOF) method is to capture the interface on the same grid used for the flow. The whole domain can be marked with a function f defined as:

$$f = \begin{cases} f = 0 & \text{Fluid 1} \\ f = 1 & \text{Fluid 2} \end{cases} \tag{1.2}$$

Since a discrete domain is considered, the value f_i is the average value of f in the cell volume:

$$f_i = \frac{1}{V_i} \int_V f(x, y, z) dV \tag{1.3}$$

Where V_i is the volume of the i-th cell. The function f is then advected by the flow:

$$\frac{\partial f}{\partial t} + \mathbf{u} \cdot \nabla f = 0 \tag{1.4}$$

The initial shape of f is an Heaviside function. The transport of f through Eq. 1.4 leads to numerical diffusion problems [138]. To overcome these difficulties, specific advection algorithms are needed. These algorithms, analysing the value of f_i in the neighbour nodes, are able to reconstruct the shape of the front and correctly perform the advection. Specific details on the advection schemes can be found in [63, 70, 147, 138]. Coalescence and breakage of the interface are implicitly accounted in this method, however, since the exact positions of the interface is unknown, they can be unphysical. One of the main advantages of the method is the exact conservation of the mass of the two phases.

1.1.3 Level set

The Level Set (LS) method was introduced by [128, 129] and in the recent years has emerged as one of the main alternatives at the VOF. The main idea is to define the interface as the 0-level of a smooth function ϕ. In particular, the function ϕ is defined as the signed distance from the interface. The time behaviour of ϕ can be obtained solving the following advection equation:

$$\frac{\partial \phi}{\partial t} + \mathbf{u} \cdot \nabla \phi = 0 \tag{1.5}$$

The main advantage is that complex algorithms to reconstruct the interface shape and perform the advection are not anymore needed (ϕ has a smooth profile). In addition, all the topological changes are automatically handled and the computation of the curvature is very accurate. The main drawback is the time degradation of the ϕ profile due to the hyperbolic character of Eq. 1.5. Specific time-integration schemes are needed [127]. To preserve the ϕ profile, a reinitialisation operation can be executed; the iso-level $\phi = 0$ is kept fixed and ϕ is modified to restore its signed-distance characteristic. This operation can be performed solving the following equation:

$$\frac{\partial \phi}{\partial \tau} = \mathrm{sgn}(\phi_0)(1 - |\nabla \phi|) \tag{1.6}$$

Where ϕ_0 is the old profile and ϕ the new one. This operation can leads to mass leakage phenomena. To improve this last aspect, LS method has been coupled with VOF [122], or a different profile for ϕ has been used [47]. This method is the common choice when a sharp approach is adopted for the solution of the flow field [166, 101, 150, 59, 122].

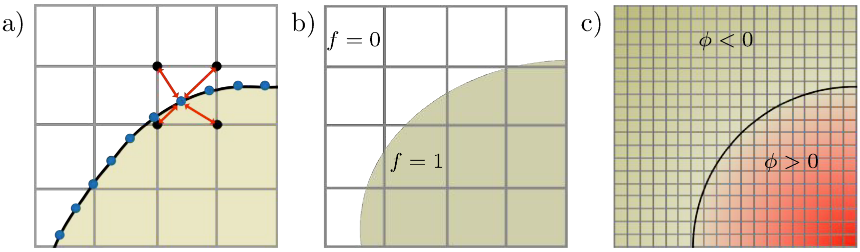

FIGURE 1.1 – Schematic representation of Front Tracking, Volume Of Fluid and Level Set methods. Panel (a), Front Tracking, in blue the marker points, the red arrows identify the smoothing operation. The surface tension forces are distributed on the nodes of the eulerian grid. Panel (b), Volume of Fluid, the values of f identifies the two different phases. Panel (c), Level Set, the sign of ϕ identifies the two phases, ϕ is the signed distance from the interface (iso-level $\phi = 0$, black line).

1.1.4 Phase field method

The Phase Field Method (PFM) was initially proposed by [23, 24, 25]; the method was employed to analyse the time-evolution of the alloy microstructure during the spinodal decomposition. This method has been then

extended to the study of incompressible multiphase flow [5, 79]. The Cahn-Hilliard equation has been modified introducing an advection term and coupled with the Navier-Stokes equation.
Cahn-Hilliard equation describes the evolution of the order parameter ϕ. The function ϕ is uniform in the bulk of the two phases and it undergoes a smooth transition across the interface. The time evolution of the order parameter ϕ, neglecting convective phenomena, can be obtained solving the following equation:

$$\frac{\partial \phi}{\partial t} = -\nabla \cdot \mathbf{j}_\phi \tag{1.7}$$

The diffusive flux $\mathbf{j}_\phi$ is proportional to the chemical potential gradient:

$$\mathbf{j}_\phi = -\mathcal{M}_\phi(\phi)\nabla \mu_\phi \tag{1.8}$$

Where $\mathcal{M}_\phi$ is the mobility parameter and μ_ϕ is the chemical potential, defined as the variational derivative of a Ginzburg-Landau free-energy functional $\mathcal{F}[\phi, \nabla\phi]$ [79, 11]:

$$\mu_\phi = \frac{\delta \mathcal{F}[\phi, \nabla\phi]}{\delta \phi} \tag{1.9}$$

When a system of two incompressible fluids is considered, the functional $\mathcal{F}$ is composed by the sum of two different contributions f_0 and f_i:

$$\mathcal{F}[\phi, \nabla\phi] = \int_\Omega f_\phi(\phi, \nabla\phi) d\Omega = \int_\Omega (f_0(\phi) + f_i(\nabla\phi)) d\Omega \tag{1.10}$$

where Ω is the domain considered and f_0 and f_i are defined as follows:

$$f_0(\phi) = \frac{\alpha}{4}\left(\phi - \sqrt{\frac{\beta}{\alpha}}\right)^2 \left(\phi + \sqrt{\frac{\beta}{\alpha}}\right)^2 \tag{1.11}$$

$$f_i(\nabla\phi) = \frac{\kappa}{2}|\nabla\phi|^2 \tag{1.12}$$

The two contributions represent respectively: (i) the bulk free energy f_0, which is the tendency of the system to separate into two pure stable phases, (ii) the mixing free energy f_i which is the energy stored in the interfacial layer, for a liquid-liquid or liquid-gas system this energy is the surface tension. A plot of the term f_0 is reported in Fig. 1.4. The parameters α and β are two positive constants that define the bulk properties, whereas κ is a positive parameter used to describe the magnitude of the surface tension. Taking the variational derivative of the functional $\mathcal{F}[\phi, \nabla\phi]$ the following expression for the chemical potential is obtained:

$$\mu_\phi = \frac{\delta \mathcal{F}\left[\phi, \nabla\phi\right]}{\delta \phi} = \alpha\phi^3 - \beta\phi - \kappa\nabla^2\phi. \tag{1.13}$$

The equilibrium profile for a planar interface (located at $x = 0$) can be obtained imposing $\nabla\mu_\phi = 0$ and thus:

$$\mu_\phi = \alpha\phi^3 - \beta\phi - \kappa\nabla^2\phi = 0 \tag{1.14}$$

This equation has an analytical solution:

$$\phi = \phi_+ \tanh\left(\frac{x}{\sqrt{2}\xi}\right) \tag{1.15}$$

Where $\xi = \sqrt{k/\beta}$ is a ratio which defines the interface thickness and $\phi_+ = \pm\sqrt{\alpha/\beta}$ is the value of ϕ in the bulk of the two phases. When convective phenomena are considered, Eq. 1.7 can be modified introducing an advection term. The modified equation is [5, 79]:

$$\frac{\partial\phi}{\partial t} + \mathbf{u}\cdot\nabla\phi = \mathcal{M}_\phi\nabla^2\mu_\phi \tag{1.16}$$

where $\mathbf{u}$ is the velocity field, $\mathcal{M}_\phi$ is the mobility parameter driving the interface relaxation, here assumed constant, and μ_ϕ is the chemical potential. Solving Eq. 1.16 the temporal and spatial behaviour of the interface can be completely determined. Compared with the other methods, the main advantages of the Phase Field Method are: (i) automatically handling and description of coalescence and/or breakage phenomena (ii) accurate description of the interface shape and curvature (iii) specific advection schemes are not necessary. The main drawback of the method is the non conservation of the mass of each phase, small mass leakages can be present.

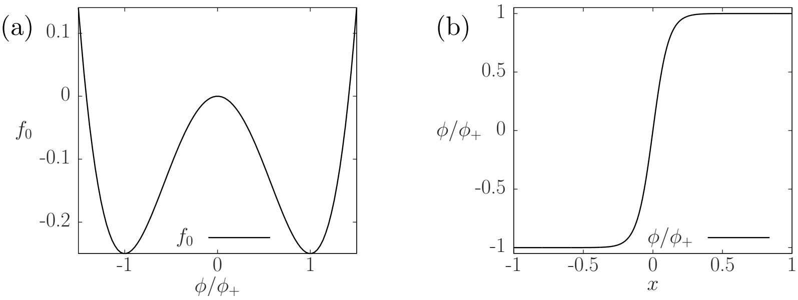

FIGURE 1.2 – In panel (a) the term f_0 of the free Ginzburg-Landau free energy functional is shown, the two minima are located at $\phi = \pm\phi_+$. In panel (b) the equilibrium profile for a planer interface is plotted, interface is located at $x = 0$, in the bulk of the two phases $\phi = \pm\phi_+$.

1.2 Flow field solution

In this section the principal methods used to obtain the solution of the flow field will be presented. The flow field inside each phase can be obtained, as

for a single phase flow, solving the Navier-Stokes equation.
The flow fields of the two phases are coupled at the interface where specific boundary conditions must be satisfied [13, 182]. For the velocity::

$$\mathbf{u}_1 \cdot \mathbf{n} - \mathbf{u}_2 \cdot \mathbf{n} = 0 \tag{1.17}$$

Where $\mathbf{u}_1$ and $\mathbf{u}_2$ are the velocity vectors at the two sides of the interface and $\mathbf{n}$ is the normal versor to the interface. Eq. 1.17 express the continuity of the velocity across the interface. A similar equation must be satisfied for the stresses:

$$\mathbf{T}_1 \cdot \mathbf{n} - \mathbf{T}_2 \cdot \mathbf{n} = \mathcal{K}\sigma\mathbf{n} - \nabla_s\sigma \tag{1.18}$$

Where $\mathbf{T}_1$ and $\mathbf{T}_2$ are the stress tensors in the two phases at the interface, σ is the surface tension, $\mathcal{K}$ is the mean curvature and ∇_s is the surface gradient operator. This equation imposes a jump condition in the stress tensor at the interface. The term $\mathcal{K}\sigma\mathbf{n}$ is a normal component whereas the term $-\nabla_s\sigma$ is a tangential component of the stress jump. The last term vanishes when surface tension is uniform.
In order to fulfil the boundary conditions imposed by the Eqs. 1.17 - 1.18, the commonly used approaches are: (i) sharp approach, one Navier-Stokes equation is solved for each phase and the jump conditions are implicitly treated (ii) continuous approach, a unique Navier-Stokes equation is solved in the whole domain and the jump conditions at the interface are enforced consdiering a source-term in the r.h.s of the NS equation.
In the following two sections, Sec. 1.2.1 and Sec. 1.2.2, the two different approaches are presented.

1.2.1 Sharp approach

When a sharp approach is considered, a Navier-Stokes equation is solved for each of the phases. Appropriate jump and boundary conditions are set at the interface. The mainly used sharp approach is the so-called Ghost Fluid Method (GFM). It was initially developed for inviscid fluid by [59] and later extended to viscus fluid by [85, 113]. The main idea is to use an interface tracking method to compute the interface position (Level-Set method is the common choice). Once the interface position is known, on the basis of ϕ a set of real and ghost nodes are defined. If the phase A is identified by $\phi > 0$, all the nodes where $\phi > 0$ will be real nodes of the phase A, by opposite the nodes where $\phi < 0$ will be ghost nodes of fluid A. When a variable is continuous across the interface, the values of ghost and real nodes match. By opposite, when dealing with a discontinuous variable, ghost and real nodes will have different values and the relative jump condition can be imposed. Using this method, since both the phases are defined in the whole domain a standard single phase solver can be used. Despite all these promising aspects, there is still a lack of knowledge on the treatment of the viscous terms and on the general accuracy provided by the method. Further details can be found in [170, 122, 166, 47, 17, 150, 101]

1.2.2 Continuous approach

When a continuous approach is considered, a unique Navier-Stokes equation is solved in the whole domain, interface is treated as a part of the fluid domain. In order fo fulfil the jump conditions imposed by Eqs. 1.17 - 1.18, surface tension forces are introduced on the r.h.s. of the NS equation. These forces, which are theoretically applied on a single line/surface, for numerical reasons must be smoothed on a thin layer using a Continuous Surface Force (CSF) method [20, 90, 136]. A similar procedure must be adopted when the proprieties (density and/or viscosity) of the two fluids are different. The proprieties can be assumed to be proportional at the value of the marker function [138]. The "smoothing" of forces and of proprieties constitutes the major drawback of this approach. Despite this, the continuous approach is the most used, indeed the same solvers of a single-phase flow, opportunely modified, can be adopted.

Treatment of surface tension forces

The presence of the surface tension introduce a jump condition for the stress along the normal and tangential direction of the interface. The normal stress jump, first term on the r.h.s. of Eq. 1.18, is proportional at the curvature $\mathcal{K}$ and at the value of the surface tension σ. The tangential jump, second term of the r.h.s., is present only when gradients of the surface tension are present. Surface tension gradients can be induced by temperature variations or by a surfactant which locally change the value of the surface tension. Therefore, in the most general case, the surface tension forces are composed by a normal $\mathbf{f}_n$ and by a tangential $\mathbf{f}_t$ component. Following [20, 81, 136], these forces can be introduced using a δ function:

$$\mathbf{f} = \underbrace{-\mathcal{K}\sigma(\mathbf{x}_s)\delta(\mathbf{x}_s)\mathbf{n}}_{\mathbf{f}_n} + \underbrace{\nabla_s\sigma(\mathbf{x}_s)\delta(\mathbf{x}_s)}_{\mathbf{f}_t} \tag{1.19}$$

Where $\mathbf{x}_s$ is the interface position, depending on the method used to describe it, the δ function can be discretised in different ways [136]. Using a PFM, the following relations based on the proprieties of ϕ are obtained [143, 162]:

$$\mathbf{n} = \frac{\nabla\phi}{|\nabla\phi|} \qquad \delta = \frac{3|\nabla\phi|^2\xi}{\sqrt{8}\phi_+^2} \qquad \mathcal{K} = \nabla\cdot\mathbf{n} \tag{1.20}$$

The coefficients used guarantee that the integral of δ across the interface is unitary. The expression used for the mean curvature can be recasted using the proprieties of the divergence operator.

$$\mathcal{K} = \nabla\cdot\frac{\nabla\phi}{|\nabla\phi|} = \frac{\nabla^2\phi}{|\nabla\phi|} - \frac{1}{|\nabla\phi|^2}\nabla\phi\cdot\nabla(|\nabla\phi|) \tag{1.21}$$

The integral of the second term, across the interface is zero and is thus neglected. The final expression of the surface tension forces can be obtained assuming an expression for the Equation Of State (EOS) [108, 2]. Details on the EOS can be found in the next section, here a general expression has been assumed:

$$\sigma(\psi) = \sigma_0 f_\sigma(\psi) \tag{1.22}$$

In Eq. 1.22, σ_0 is the surface tension of a clean interface and ψ is the surfactant concentration. Combining Eq. 1.22 and Eq. 1.19, the following expression for the normal component $\mathbf{f}_n$ can be obtained:

$$\mathbf{f}_n = -\frac{3\sigma_0 f(\psi)\xi}{\sqrt{8}\phi_+^2}\nabla^2\phi\nabla\phi \tag{1.23}$$

The same result can be obtained following the procedure proposed by [95]. A stress tensor τ_c, that accounts for the jump condition of the normal stress is introduced in the Navier-Stokes equation.

$$\mathbf{f}_n = \frac{3\sigma_0 f(\psi)\xi}{\sqrt{8}\phi_+^2}\nabla\cdot\tau_c \tag{1.24}$$

$$\tau_c = (|\nabla\phi|^2\mathbf{I} - \nabla\phi\otimes\nabla\phi) \tag{1.25}$$

The two formulations, Eq. 1.24 and Eq. 1.23, are equivalent. Using a stress formulation the gradient term present has zero contribution and the only contribution is produced by the dyadic product. In a similar way, an expression for the tangential component of the surface tension forces can be derived. This contribution, also referred as Marangoni term, is proportional to the surface tension gradients. From Eq. 1.19 and using the expressions of Eq. 1.20 the following expression can be obtained:

$$\mathbf{f}_t = \frac{3\xi\sigma_0}{\sqrt{8}\phi_+^2}(|\nabla\phi|^2\mathbf{I} - \nabla\phi\otimes\nabla\phi)\nabla f(\psi) \tag{1.26}$$

The sum of the two components is:

$$\begin{aligned}\mathbf{f} = \mathbf{f}_n + \mathbf{f}_t \quad &= \quad \frac{3\xi\sigma_0}{\sqrt{8}\phi_+^2}f_\sigma(\psi)\nabla\cdot(|\nabla\phi|^2\mathbf{I} - \nabla\phi\otimes\nabla\phi) \\ &+ \quad \frac{3\xi\sigma_0}{\sqrt{8}\phi_+^2}(|\nabla\phi|^2\mathbf{I} - \nabla\phi\otimes\nabla\phi)\nabla f_\sigma(\psi)\end{aligned} \tag{1.27}$$

The two parts can be rearranged [168]:

$$\mathbf{f} = \frac{3\xi\sigma_0}{\sqrt{8}\phi_+^2}\nabla\cdot(f_\sigma(\psi)(|\nabla\phi|^2\mathbf{I} - \nabla\phi\otimes\nabla\phi)) \tag{1.28}$$

When surface tension is uniform, $\sigma(\psi) = \sigma_0$, the tangential component of the surface tension forces vanishes.

$$\mathbf{f} = \mathbf{f}_n = \frac{3\sigma_0\xi}{\sqrt{8}\phi_+^2}\nabla\cdot(|\nabla\phi|^2\mathbf{I} - \nabla\phi\otimes\nabla\phi) \tag{1.29}$$

Equation of state for the surface tension

The surface tension can be influenced by the presence of temperature variations or surface active agents (surfactants). The effects on the surface tension can be described using an Equation Of State (EOS). In the following, we restrict to the case of the surfactant. A surfactant concentration ψ can be defined, ψ will span between $\psi = 0$ (absence of surfactant) and $\psi = 1$ (saturation of surfactant). Thanks to their amphiphilic character (hydrophilic head attached to an hydrophilic tail, Fig. 1.3), the molecules preferentially occupy the interfacial area. These molecules decrease the net force that a single molecule of fluid close to the interface undergoes. As consequence surface tension decreases. The effect of the surfactant can be described using a Langmuir EOS [108]:

$$\sigma(\psi) = \sigma_0(1 + \beta_s \ln(1 - \psi) \tag{1.30}$$

Where β_s is the elasticity number, a dimensionless parameter that quantifies the effect of the surfactant on the surface tension. When surfactant concentration is low, Eq. 1.30 can be linearised [124, 137]:

$$\sigma(\psi) = \sigma_0(1 - \beta_s\psi)) \tag{1.31}$$

Eq. 1.30 accurately model the effect of the surfactant on the surface tension until $\sigma/\sigma_0 \simeq 0.5$. Larger surfactant concentrations do not change the surface tension which reaches a plateau [28, 16].

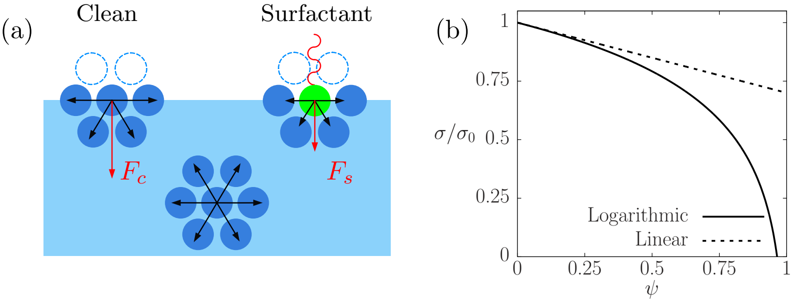

FIGURE 1.3 – Panel (a), physical mechanism behind the surface tension and the effect of the surfactant on it are graphically explained. When a molecule is close to the interface (left), the absence of the hydrogen bounds with the two dashed molecules produces a net force F_c which attracts the molecule towards the bulk. The force F_c is responsible for the surface tension. When surfactant molecules are present (right), the magnitude of the net force F_s decreases and as well the surface tension. Panel (b), Langmuir EOS (continuous line) and relative linear approximation (dashed).

Treatment of variable viscosity

Using a continuous approach, viscosity and density variations has to be incorporated in the Navier-Stokes equation. Using a PFM, the variation

can be assumed to be proportional to the order parameter ϕ [91].
Under this hypothesis, $\eta = \eta(\phi)$. Defining η_c as the viscosity of the phase identified by $\phi = -\phi_+$, η_d as the viscosity of the phase identified by $\phi = \phi_+$ and using a linear interpolation the viscosity can be rewritten as:

$$\eta(\phi) = \eta_c \frac{\phi - \phi_+}{2} + \eta_d \frac{\phi + \phi_+}{2} \tag{1.32}$$

Using Eq. 1.32 in the Navier-Stokes equation, the viscous term cannot be simplified. However, the viscous term can be splitted in a linear and a non linear part:

$$\eta(\phi) = \eta_c + \overline{\eta}(\phi) \tag{1.33}$$

The choice of η_c as reference is arbitrary. For numerical reasons, related to the time and space discretisation scheme used, greater numerical stability is achieved when the reference viscosity is set as the one of the more viscous fluid. Using Eq. 1.33, the viscous stress tensor become:

$$\nabla \cdot \left(\eta(\phi)\left(\nabla \mathbf{u} + \nabla \mathbf{u}^T\right)\right) = \eta_c \nabla^2 \mathbf{u} + \nabla \cdot \left(\overline{\eta}(\phi)\left(\nabla \mathbf{u} + \nabla \mathbf{u}^T\right)\right) \tag{1.34}$$

The first term is a linear diffusive term, the second term is a non-linear which depends on the order parameter ϕ.

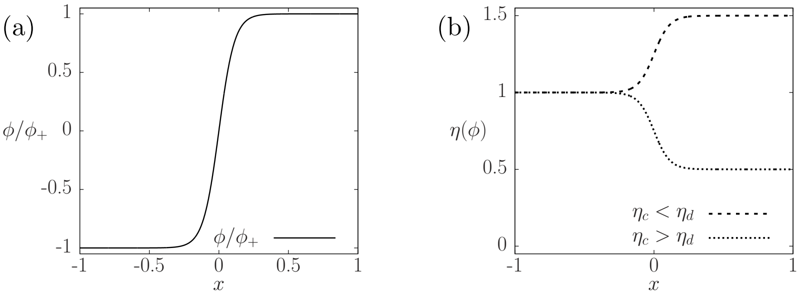

FIGURE 1.4 – In the panel (a) the equilibrium profile of ϕ for a planar interface is shown. In the panel (b) two viscosity profiles are shown. The first profile (dashed) shows a case in which the viscosity of the phase identified by $\phi = \phi_+$, η_d, is greater than the viscosity of the phase identified by $\phi = -\phi_+$, η_c. The second profile (dotted) shows the opposite situation.

Navier-Stokes with variable viscosity and surface tension force

The final form of the Navier-Stokes can be now obtained. The equation is obtained using a continuous approach, assuming two phases with matched density but different viscosity and non uniform surface tension.
The viscous term has been replaced by the one introduced in Eq. 1.34. The expression of the surface tension forces, Eq. 1.27, has been introduced on

the r.h.s. The equation reads:

$$\begin{aligned}\rho\frac{\partial \mathbf{u}}{\partial t}+\mathbf{u}\cdot\nabla\mathbf{u} &= \eta_c\nabla^2\mathbf{u}+\nabla\cdot\left(\overline{\eta}(\phi)\left(\nabla\mathbf{u}+\nabla\mathbf{u}^T\right)\right)-\nabla p \\ &+ \frac{3\xi\sigma_0}{\sqrt{8}\phi_+^2}\nabla\cdot\left(f_\sigma(\psi)(|\nabla\phi|^2\mathbf{I}-\nabla\phi\otimes\nabla\phi)\right) \qquad (1.35)\end{aligned}$$

Where ρ is the density of the two phases, η_c is the viscosity of the phase defined by $\phi=-\phi_+$, the function $\overline{\eta}(\phi)$ accounts for the viscosity contrast between the two phases, p is the pressure and $\mathbf{u}$ is the velocity field. Solving Eq. 1.35, the flow field in the whole system can be obtained. Eq. 1.35 is solved assuming an incompressible flow:

$$\nabla\cdot\mathbf{u}=0 \qquad (1.36)$$

1.3 Surfactant

The study of a multiphase system with a surfactant represents an open challenge from a numerical point of view. The problem requires an accurate description of the interface; a partial differential equation for the surfactant has to be solved on it[160]. In addition, the mathematical domain continuously changes its shape and can undergo topological transition as coalescence and/or breakup.

In the past years, different numerical techniques have been proposed, each technique has its own peculiarity and has been developed in conjunction with a specific interface tracking/capturing method. The choice of the numerical technique adopted is also influenced by the physical propriety of the surfactant (soluble or insoluble). When a insoluble surfactant is considered, the transport equation for the surfactant proposed by [160] is solved only at the interface. On the other side, if a soluble surfactant is considered, two coupled equations are solved in the bulk and along the interface [125].

The tracking of insoluble surfactant in conjunction with a LS method has been proposed by [186, 187, 189, 188] whereas a similar approach has been developed by [117] for FT. A possible overcome to these challenges is represented by the extension of the phase field method to the surfactant. A continuous variable ψ is defined in the whole domain. This approach has been initially proposed by [104] and then further developed by [94, 176, 112, 171]. In these works, convective phenomena have been neglected. Only recently, the dynamics of the phases and of the surfactant has been coupled with the flow [52, 197, 62]. In the following, the extension of the phase field method to the surfactant will be presented.

1.3.1 Phase field method for the surfactant

The Phase Field Method (PFM) can be extended to consider a surfactant introducing a new order parameter, in this case the surfactant concentration

ψ. The time evolution of the phase field ϕ and of the surfactant concentration ψ can be derived from a two-order parameter Ginzburg-Landau free energy functional. Following [94, 176], the extended free-energy functional can be written as the sum of two terms: (i) the classic free energy functional previously used for a clean system (ii) an additional part which accounts for the surfactant. Thus, the new two order parameters Ginzburg-Landau free energy functional $\mathcal{F}[\phi, \nabla\phi, \psi, \nabla\psi]$ reads:

$$\mathcal{F}[\phi, \nabla\phi, \psi, \nabla\psi] = \int_\Omega f_\phi(\phi, \nabla\phi) + f_\psi(\phi, \nabla\phi, \psi, \nabla\psi) d\Omega \tag{1.37}$$

The term f_ϕ keeps the same expression previously used in Eq. 1.10. The new term introduced, f_ψ, accounts for the surfactant, in particular controls the amphiphilicity and the solubility of the surfactant molecules. The mathematical expressions of the terms composing f_ψ is slightly different among the authors (see [112] for a brief review). The model here used is the one identified as Model-3 by [52] combined with some further modifications developed by [197].
Following [52, 197], f_ψ can be decomposed in three contributions:

$$\begin{aligned} f_\psi(\phi, \nabla\phi, \psi, \nabla\psi) &= \underbrace{\lambda_\psi(\psi \ln\psi + (1-\psi)\ln(1-\psi))}_{f_e} \\ &- \underbrace{\frac{\kappa}{2}\psi\left(1-\left(\frac{\phi}{\phi_+}\right)^2\right)^2}_{f_1} + \underbrace{\frac{s_\psi}{2}\psi\left(\frac{\phi}{\phi_+}\right)^2}_{f_s} \end{aligned} \tag{1.38}$$

The term f_e express the tendency of the surfactant to be uniformly distributed. The functional has a minimum for $\psi = 0.5$. Furthermore, this term restrict the possible value of ψ between the fully saturated state $\psi = 1$ and the absence of surfactant $\psi = 0$. The magnitude of this term can be tuned via the parameter λ_ψ. The term f_1, in the first derivation proposed by [104], is assumed to be proportional at $|\nabla\phi|^2$. This term has been then replaced by [52] with the expression present in Eq. 1.38. This term accounts for the amphiphilic character of the surfactant molecules. The last term f_s controls the solubility of the surfactant in the bulk. In the limit of $s_\psi \to +\infty$ the surfactant is insoluble in the bulk of the two phases. A plot of the different contributions is reported in Fig. 1.5. The expression of the Ginzburg-Landau free energy functional will be:

$$\begin{aligned} \mathcal{F}[\phi, \nabla\phi, \psi, \nabla\psi] &= \int_\Omega \underbrace{(f_0(\phi) + f_i(\nabla\phi))}_{f_\phi} d\Omega \\ &+ \int_\Omega \underbrace{(f_e(\psi) + f_1(\phi, \psi) + f_s(\phi, \psi))}_{f_\psi} d\Omega \end{aligned} \tag{1.39}$$

The time evolution of the two order parameter ϕ and ψ can be obtained solving the following system of equations:

$$\frac{\partial \phi}{\partial t} = -\nabla \cdot \mathbf{j}_\phi \qquad \mathbf{j}_\phi = -\mathcal{M}_\phi(\phi)\nabla\mu_\phi \tag{1.40}$$

$$\frac{\partial \psi}{\partial t} = -\nabla \cdot \mathbf{j}_\psi \qquad \mathbf{j}_\psi = -\mathcal{M}_\psi(\psi)\nabla\mu_\psi \tag{1.41}$$

Where the expressions of μ_ϕ and μ_ψ can be obtained computing the variational derivative of the Ginzburg-Landau free energy functional with respect to ϕ and ψ:

$$\mu_\phi = \frac{\delta \mathcal{F}}{\delta \phi} = \alpha\phi^3 - \beta\phi - \kappa\nabla^2\phi + \mathcal{I}(\psi,\phi) \tag{1.42}$$

$$\mu_\psi = \frac{\delta \mathcal{F}}{\delta \psi} = \lambda_\psi \ln\left(\frac{\psi}{1-\psi}\right) - \frac{\kappa}{2}\left(1-\left(\frac{\phi}{\phi_+}\right)^2\right)^2 + \frac{s_\psi}{2}\left(\frac{\phi}{\phi_+}\right)^2 \tag{1.43}$$

The term $\mathcal{I}$ is an interface sharpening term [197, 171]. This term shrinks the interface thickness depending on the surfactant concentration ψ. From a numerical point of view is preferred to maintain an uniform interface thickness, for this reason, as proposed by [197] this term is neglected. Neglecting $\mathcal{I}$, the profile of the order parameter ϕ is independent from the surfactant ψ and is the same obtained before, Eq. 1.15. The equilibrium profile for ψ can be obtained imposing $\nabla\mu_\psi = 0$:

$$\mu_\psi = \lambda_\psi \ln\left(\frac{\psi}{1-\psi}\right) \underbrace{- \frac{\kappa}{2}\left(1-\left(\frac{\phi}{\phi_+}\right)^2\right)^2 + \frac{s_\psi}{2}\left(\frac{\phi}{\phi_+}\right)^2}_{C_{\psi\phi}} = \text{const} \tag{1.44}$$

The term $C_{\psi\phi}$ identifies the effect of ϕ on μ_ψ. At the equilibrium μ_ψ is uniform in all the domain and in the bulk of the two phases $\phi/\phi_+ = \pm 1$ and $\psi = \psi_b$:

$$\mu_{\psi_b} = \lambda_\psi \ln\left(\frac{\psi_b}{1-\psi_b}\right) + \frac{s_\psi}{2} \tag{1.45}$$

The same equation can be written for a generic position x:

$$\mu_{\psi(x)} = \lambda_\psi \ln\left(\frac{\psi}{1-\psi}\right) + C_{\psi\phi}(x) \tag{1.46}$$

Subtracting Eq. 1.45 from Eq. 1.46 and defining $\psi_c(x)$ as:

$$\psi_c(x) = \frac{\psi_b}{(1-\psi_b)}\frac{(1-\psi)}{\psi} \tag{1.47}$$

The following equation for $\psi_c(x)$ is obtained:

$$\lambda_\psi \ln(\psi_c(x)) = C_{\psi\phi}(x) - \frac{s_\psi}{2} \tag{1.48}$$

This intermediate profile depends only on the profile of ϕ, once that ψ_b is fixed, the total equilibrium profile $\psi(x)$ is:

$$\psi(x) = \frac{\psi_b}{\psi_b + \psi_c(x)(1-\psi_b)} \tag{1.49}$$

The equilibrium profile for $\psi(x)$ is reported in Fig. 1.5(b). The surfactant concentration $\psi(x)$ reach the maximum value at the interface $\phi = 0$.
The time evolution of the order parameter ψ can be obtained from Eq. 1.41 and choosing an expression for the mobility $\mathcal{M}_\psi(\psi)$. To accurately describe the adsorption dynamics [52] a variable mobility has been considered:

$$\mathcal{M}_\psi(\psi) = \mathcal{M}_\psi \psi(1-\psi) \tag{1.50}$$

Using this expression, a 2^{nd} order diffusive term is obtained:

$$\frac{\partial \psi}{\partial t} = \lambda_\psi \mathcal{M}_\psi \nabla^2 \psi + \mathcal{M}_\psi \nabla \cdot ((\psi(1-\psi))C_{\psi\phi}) \tag{1.51}$$

The presence of the flow field is accounted introducing an advection term:

$$\frac{\partial \psi}{\partial t} + \mathbf{u} \cdot \nabla \psi = \lambda_\psi \mathcal{M}_\psi \nabla^2 \psi + \mathcal{M}_\psi \nabla \cdot ((\psi(1-\psi))C_{\psi\phi}) \tag{1.52}$$

Solving Eq. 1.52 the temporal and spatial behaviour of the surfactant concentration can be completely described.

1.4 Dimensional analysis

In this work, the governing equations 1.16 - 1.35 - 1.36 - 1.52 have been solved on a flat channel geometry where two infinite parallel walls are deployed at a distance $L_z = 2h$. A sketch of the geometry used is reported in Fig. 1.6. All the equations are solved in a dimensionless form. In the following the dimensionless procedure is applied at all the equations. The Cahn-Hilliard equation 1.16 can be made dimensionless using the following quantities:

$$\tilde{\mathbf{x}} = \frac{\mathbf{x}}{h} \qquad \tilde{t} = \frac{t u_\tau}{h} \qquad \tilde{\mathbf{u}} = \frac{\mathbf{u}}{u_\tau} \qquad \tilde{\phi} = \frac{\phi}{\phi_+} \tag{1.53}$$

Where u_τ is the friction velocity, defined as $u_\tau = \sqrt{\tau_w/\rho}$, with τ_w the shear stress at the wall and ρ density of the two phases. ϕ_+ is the value

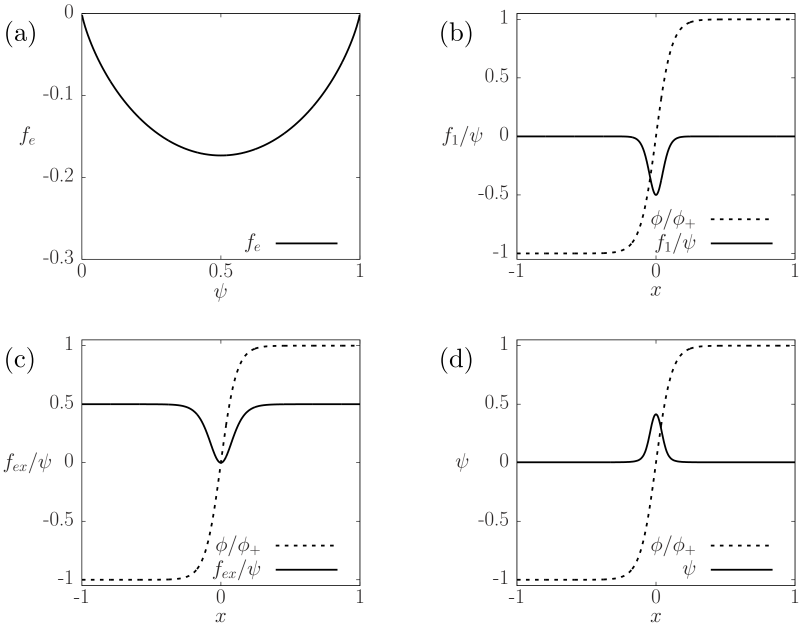

FIGURE 1.5 – In the panel (a) the shape of the term f_e is shown, increasing λ_ψ the value of the minimum located $\psi = 0.5$ decrease and the surfactant diffuse easily. In the panel (b) the term f_1 is shown, this term promote the accumulation of surfactant at the interface, its contribution is related at the shape of ϕ. In the panel (c) the term f_s is reported, this term accounts for the solubility of surfactant in the bulk. In the panel (d) the equilibrium profile of ϕ and ψ are reported. Both the profiles are obtained solving $\mu_\phi = 0$ and $\mu_\psi = 0$.

assumed by ϕ in the bulk of the two phases and defined as in Eq. 1.15. The Cahn-Hilliard equation rewritten in a dimensionless form is:

$$\frac{\partial \tilde{\phi}}{\partial \tilde{t}} + \tilde{\mathbf{u}} \cdot \nabla \tilde{\phi} = \frac{1}{Pe_\phi} \nabla^2 (\tilde{\phi}^3 - \tilde{\phi} - Ch^2 \nabla^2 \tilde{\phi}) \tag{1.54}$$

After the dimensionless treatment, the order parameter assume the values $\phi = \pm 1$ in the bulk of the two phases. In a similar way, the equilibrium profile will be:

$$\tilde{\phi} = \tanh\left(\frac{\tilde{x}}{\sqrt{2}Ch}\right) \tag{1.55}$$

The two dimensionless groups introduced in Eq. 1.54 and Eq. 1.55 are defined as follows:

$$Pe_\phi = \frac{u_\tau h}{\mathcal{M}_\phi \beta} \qquad Ch = \frac{\xi}{h} \tag{1.56}$$

The Peclet number, Pe_ϕ, is the ratio between the convective time-scale $u_\tau h$ and the diffusive time-scale $\mathcal{M}_\phi \beta$. This parameter controls the interface

relaxation time. The Cahn number, Ch, is the ratio between the interface characteristic length scale ξ and the domain length scale h. This parameter sets the thickness of the interface. When a system of immiscible fluids is analysed, the real interface thickness, order of $O(10^{-8}m)$, for computational reasons cannot be used. The common solution is to artificially enlarge the interface thickness and to use a scaling between Pe_ϕ and Ch, this guarantees the achievement of the sharp interface limit. Different scaling have been proposed in literature [116, 86, 196, 120, 106],the one proposed by [120], $Pe_\phi \propto Ch^{-1}$, has been here used. Once the grid is fixed, Ch is set to the minimum value possible according to the numerical method adopted and Pe_ϕ is set following the scaling. In this thesis, where a pseudo-spectral method has been adopted, only three mesh points across the interface are needed.
Navier-Stokes equation has been made dimensionless using the quantities introduced in Eq. 1.53 and the following ones:

$$\tilde{p} = \frac{ph}{\rho u_\tau^2} \qquad \tilde{\eta}(\phi) = \frac{\overline{\eta}(\phi)}{\eta_c} \qquad \tilde{\psi} = \psi \tag{1.57}$$

Where η_c is the viscosity of the phase identified by $\tilde{\phi} = -1$. Navier-Stokes equation is solved under the hypotheses of an incompressible flow and of two phases with matched density. Thus the dimensionless mass conservation equation reads:

$$\nabla \cdot \tilde{\mathbf{u}} = 0 \tag{1.58}$$

The Equation Of State (EOS) is made dimensionless using σ_0, the surface tension of a clean interface as reference. In the equation of state ψ is already dimensionless. The dimensionless EOS will match $f_\sigma(\tilde{\psi})$ as defined in Eq. 1.22.

$$\frac{\sigma}{\sigma_0} = f_\sigma(\tilde{\psi}) = 1 + \beta_s \ln(1 - \tilde{\psi}) \qquad \frac{\sigma}{\sigma_0} = f_\sigma(\tilde{\psi}) = 1 - \beta_s \tilde{\psi} \tag{1.59}$$

Navier-Stokes equation written in a dimensionless form is:

$$\begin{aligned} \frac{\partial \tilde{\mathbf{u}}}{\partial \tilde{t}} + \tilde{\mathbf{u}} \cdot \nabla \tilde{\mathbf{u}} &= \frac{1}{Re_\tau} \nabla^2 \tilde{\mathbf{u}} + \frac{1}{Re_\tau} \nabla \cdot (\tilde{\eta}(\tilde{\phi})(\nabla \tilde{\mathbf{u}} + \nabla \tilde{\mathbf{u}}^T)) - \nabla \tilde{p} \\ &+ \frac{3}{\sqrt{8}} \frac{Ch}{We} \nabla \cdot (f_\sigma(\tilde{\psi})(|\nabla \tilde{\phi}|^2 \mathbf{I} - \nabla \tilde{\phi} \otimes \nabla \tilde{\phi})) \end{aligned} \tag{1.60}$$

The dimensionless parameters that appears in Eq. 1.60 are defined as follows:

$$Re_\tau = \frac{\rho u_\tau h}{\eta_c} \qquad We = \frac{\rho u_\tau^2 h}{\sigma_0} \qquad \lambda = \frac{\eta_d}{\eta_c} \tag{1.61}$$

The shear Reynolds number, Re_τ, is the ratio between inertial forces $\rho u_\tau h$ and viscous forces η_c. In defining Re_τ, η_c, the viscosity of the phase identified by $\tilde{\phi} = -1$ is used as reference. The viscosity of the other phase can

be specified through the viscosity ratio λ.
The dimensionless viscosity contrast as defined in Eq. 1.57 will have the following values in the bulk of the two phases:

$$\tilde{\eta} = \begin{cases} \tilde{\eta} = 0 & \tilde{\phi} = -1 \\ \tilde{\eta} = \lambda - 1 & \tilde{\phi} = +1 \end{cases} \tag{1.62}$$

The Weber number, We, is the ratio between inertial $\rho u_\tau^2 h$ and surface tension forces, σ_0. In the definition of We, the surface tension of a clean interface has been used as reference. Large values of We identifies a low value of the surface tension and an interface which can be easily deformed. In the limit of $We \rightarrow \infty$ the surface tension force vanishes and the flow behave as a single phase flow (in the hypothesis of matched viscosity). The parameter β_s describes the effect of the surfactant on the surface tension. Large values of β_s yields to strong variations of the surface tension and larger Marangoni stresses.
Surfactant transport equation 1.52 has been made dimensionless using the quantities introduced in Eqs. 1.53 - 1.57 and will be:

$$\frac{\partial \tilde{\psi}}{\partial \tilde{t}} + \tilde{\mathbf{u}} \cdot \nabla \tilde{\psi} = \frac{Pi}{Pe_\psi} \nabla^2 \tilde{\psi} + \frac{1}{Pe_\psi} \nabla \cdot (\tilde{\psi}(1 - \tilde{\psi}) \nabla \tilde{C}_{\psi\phi}) \tag{1.63}$$

Where the term $\tilde{C}_{\psi\phi}$ is defined as:

$$\tilde{C}_{\psi\phi} = -\frac{1}{2}(1 - \tilde{\phi}^2)^2 + \frac{\phi^2}{2E_x} \tag{1.64}$$

The dimensionless equilibrium profile for $\tilde{\psi}$ can be obtained using the intermediate variable $\tilde{\psi}_c$, Eq. 1.47, and reads to:

$$Pi \ln(\tilde{\psi}_c(\tilde{x})) = \tilde{C}_{\psi\phi} - \frac{1}{2E_x} \tag{1.65}$$

The final expression is:

$$\tilde{\psi}(\tilde{x}) = \frac{\tilde{\psi}_b}{\tilde{\psi}_b + \tilde{\psi}_c(\tilde{x})(1 - \tilde{\psi}_b)} \tag{1.66}$$

The dimensionless parameters in Eqs. 1.63 - 1.64 are defined as follows:

$$Pe_\psi = \frac{\alpha u_\tau h}{\beta^2 \mathcal{M}_\psi} \qquad Pi = \frac{\lambda_\psi}{\beta^2} \qquad E_x = \frac{\beta}{s_\psi} \tag{1.67}$$

The surfactant Peclet number, Pe_ψ, is the ratio between the convective and the diffusive phenomena. Pe_ψ controls the diffusion of surfactant, high values of Pe_ψ yields to a surfactant distribution which will be dominated by the convective phenomena. By opposite, when low values are used the

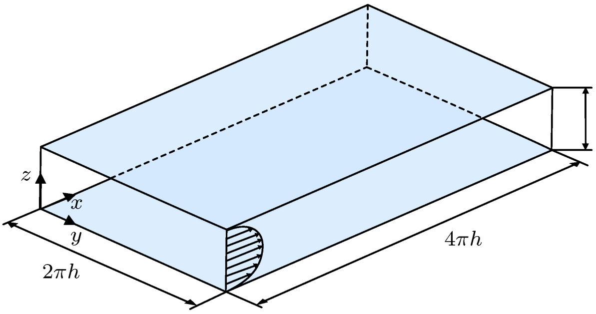

FIGURE 1.6 – Geometry of the channel used in the simulations. Two walls are present along the z axis, wall-normal direction, the channel height is $L_z = 2h$. The channel is periodic along the x and y directions. The dimensions L_x and L_y are $2\pi h$ and $4\pi h$.

diffusion is able to restore the uniform distribution. The parameter Pi is a dimensionless factor which controls the adsorption dynamics of surfactant from bulk to the interface and vice versa. The parameter E_x, controls the solubility of surfactant in the bulk of the two phases. Large values of E_x allow high concentration of surfactant in the bulk. The equilibrium profile for $\tilde{\psi}$, is influenced by both the parameters Pi and E_x.

1.5 Details on the numerical method

1.5.1 Solution algorithm

In this section the dimensionless governing equations 1.54 - 1.60 - 1.58 - 1.63 are rewritten in a formulation suitable to match the solution algorithm. The momentum and mass conservation equations are rewritten in the so-called "normal-velocity normal-vorticity" formulation; Cahn-Hilliard equation is rewritten adopting a particular "operator-splitting" technique whereas the Surfactant equation do not require particular treatment. A schematic representation of the solution procedure is shown in Fig. 1.7.

Velocity-vorticity formulation

The dimensionless momentum equation 1.60 is rewritten as follows (the superscripts have been removed for sake of brevity):

$$\frac{\partial \mathbf{u}}{\partial t} = \mathbf{S} + \frac{1}{Re_\tau}\nabla^2 \mathbf{u} - \nabla p', \tag{1.68}$$

where the pressure term p has been decomposed in fluctuating and mean components, $p = p' + \overline{p}$. The mean pressure gradient $\Pi = \nabla \overline{p}$, all the non-linear terms have been collected into the term $\mathbf{S}$:

$$\begin{aligned}\mathbf{S} = \quad & - \quad \mathbf{u}\cdot\nabla\mathbf{u} + \Pi + \frac{1}{Re_\tau}\nabla\cdot(\eta(\phi)(\nabla\mathbf{u}+\nabla\mathbf{u}^T)) \\ & + \quad \frac{3}{\sqrt{8}}\frac{Ch}{We}\nabla\cdot(f(\psi)(|\nabla\phi|^2\mathbf{I}-\nabla\phi\otimes\nabla\phi))\end{aligned} \tag{1.69}$$

To solve the system composed by the Eq. 1.58 and Eq. 1.60, the fluctuating pressure term $\nabla p'$ is removed by taking the curl of Eq. 1.68, as result the transport equation for the vorticity $\boldsymbol{\omega}$ is obtained:

$$\frac{\partial\boldsymbol{\omega}}{\partial t} = \nabla\times\mathbf{S} + \frac{1}{Re_\tau}\nabla^2\boldsymbol{\omega} \tag{1.70}$$

where the identity $\nabla\times\nabla p' = 0$ has been used. Taking twice the curl of Eq. 1.68, substituting Eq. 1.58 and the identity $\nabla\times\nabla\times\mathbf{c} = \nabla(\nabla\cdot\mathbf{c}) - \nabla^2\mathbf{c}$, the following 4^{th}-order equation for the velocity $\mathbf{u}$ is obtained:

$$\frac{\partial\nabla^2\mathbf{u}}{\partial t} = \nabla^2\mathbf{S} - \nabla(\nabla\cdot\mathbf{S}) + \frac{1}{Re_\tau}\nabla^4\mathbf{u} \tag{1.71}$$

Eqs. 1.70 - 1.71 are solved for the wall-normal components of the vorticity ω_z and velocity w, adopting the "velocity - vorticity" algorithm developed by [92]; rewritting Eqs. 1.70 - 1.71 for ω_z and w, respectively, the following equations are obtained:

$$\frac{\partial\omega_z}{\partial t} = \frac{\partial S_y}{\partial x} - \frac{\partial S_x}{\partial y} + \frac{1}{Re_\tau}\nabla^2\omega_z \tag{1.72}$$

$$\frac{\partial(\nabla^2 w)}{\partial t} = \nabla^2 S_z - \frac{\partial}{\partial z}\left(\frac{\partial S_x}{\partial x} + \frac{\partial S_y}{\partial y} + \frac{\partial S_z}{\partial z}\right) + \frac{1}{Re_\tau}\nabla^4 w \tag{1.73}$$

With a suitable set of boundary conditions, ω_z and w are computed and then the streamwise the spanwise velocity components v are obtained from the continuity equation and the vorticity definition:

$$\frac{\partial w}{\partial z} = -\frac{\partial u}{\partial x} - \frac{\partial v}{\partial y} \tag{1.74}$$

$$\omega_z = \frac{\partial v}{\partial x} - \frac{\partial u}{\partial y} \tag{1.75}$$

Once the velocity field is obtained, the fluctuating pressure p' can be obtained by solving a Poisson-type equation:

$$\nabla^2 p' = \nabla\cdot\mathbf{S} \tag{1.76}$$

Cahn-Hilliard equation splitting

The solution of the Cahn-Hilliard equation requires robust numerical schemes due to the high order operators that it involves; expanding Eq. 1.54, a 4^{th}-order operator is highlighted:

$$\frac{\partial \phi}{\partial t} = -\mathbf{u} \cdot \nabla \phi + \frac{1}{Pe_\phi} \left(\nabla^2 \phi^3 - \nabla^2 \phi - Ch^2 \nabla^4 \phi \right) \tag{1.77}$$

To reduce the stability requirements and adopt the same pseudo-spectral scheme involved for the momentum equation, Eq. 1.77 is rewritten in the following way:

$$\frac{\partial \phi}{\partial t} = S_\phi + \frac{sCh^2}{Pe_\phi} \nabla^2 \phi - \frac{Ch^2}{Pe_\phi} \nabla^4 \phi \tag{1.78}$$

The operator splitting $\nabla^2 \phi = \nabla^2 \phi (sCh^2 + 1) - sCh^2 \nabla^2 \phi$ is similar to the one adopted by [193] and is obtained through a positive coefficient s that is chosen considering the temporal discretisation; similar procedures can be found in [11, 102]. The convective term, the non-linear term and the terms rising from the operator splitting are collected in the term S_ϕ:

$$S_\phi = -\mathbf{u} \cdot \nabla \phi + \frac{1}{Pe_\phi} \nabla^2 \phi^3 - \frac{(sCh^2 + 1)}{Pe_\phi} \nabla^2 \phi \tag{1.79}$$

Surfactant equation

The solution of the surfactant transport equation, Eq. 1.63, do not require particular schemes and can be directly solved. The equation to solve is the following:

$$\frac{\partial \psi}{\partial t} = -\mathbf{u} \cdot \nabla \psi + \frac{Pi}{Pe_\psi} \nabla^2 \psi + \frac{1}{Pe_\psi} \nabla \cdot (\psi (1 - \psi) \nabla C_{\psi\phi}) \tag{1.80}$$

In this equation a second order diffusive term is present. The non-linear terms can be collected in the term S_ψ:

$$S_\psi = -\mathbf{u} \cdot \nabla \psi + \frac{1}{Pe_\psi} \nabla \cdot (\psi (1 - \psi) \nabla C_{\psi\phi}) \tag{1.81}$$

The final shape of the surfactant transport equation is:

$$\frac{\partial \psi}{\partial t} = S_\psi + \frac{Pi}{Pe_\psi} \nabla^2 \psi \tag{1.82}$$

1.5.2 Spectral approximation

The equations 1.72 - 1.73 - 1.77 and 1.82 are solved adopting a pseudo-spectral spatial discretisation: solutions are approximated by Fourier transforms along the two periodic directions of the channel geometry x and y, respectively; Chebyshev polynomials are adopted to approximate the solution along the wall-normal direction. In order to avoid convolutions in the Fourier-Chebishev space, the multiplication of spectral variables (i.e. convective terms) is obtained transforming back the variables to the physical space, taking the multiplications and the re-transforming to the Fourier-Chebyshev space. For this reason these class of algorithms is also known as "pseudo-spectral algorithms". A signal g, projected in to the Fourier space along the periodic directions x and y, can be represented by the following sum of harmonics:

$$g(x,y,z) = \sum_{n_x=-\frac{N_x}{2}+1}^{\frac{1}{2}N_x} \sum_{n_y=-\frac{N_y}{2}+1}^{\frac{1}{2}N_y} \hat{g}(k_x,k_y,z)e^{j(k_x x+k_y y)} \tag{1.83}$$

where $j = \sqrt{-1}$ is the imaginary unit of the complex representation, $\hat{g}$ is the Fourier coefficient of the signal in the modal coordinates (k_x, k_y); at this point dependence on the physical coordinate z is still present. The two periodic directions are treated with a Fast Fourier Transform (FFT) algorithm imposing periodicity lengths of L_x and L_y and projecting the velocity vector on to N_x and N_y Fourier modes in the x and y directions of the geometry of Fig. 1.6. Through the Fourier transform, the variables are mapped an a uniform grid in the physical space and the nodes spacing is:

$$\Delta x = \frac{L_x}{N_x - 1} \qquad \Delta y = \frac{L_y}{N_y - 1} \tag{1.84}$$

The signal is decomposed in a sum of periodical functions characterised by wavenumber and amplitude; the former represents the frequency of the corresponding harmonic, whereas the latter is the magnitude of the harmonic. Each mode n_x or n_y is characterised by the following wave-numbers:

$$k_x = \frac{2\pi n_x}{L_x}, \qquad k_y = \frac{2\pi n_y}{L_y} \tag{1.85}$$

Since the Fourier basis is orthogonal, the Fourier transform $\hat{g}$ can be obtained as follows:

$$\hat{g}(k_x,k_y,z) = \frac{1}{N_x N_y} \sum_{n_x=-\frac{N_x}{2}+1}^{\frac{N_x}{2}} \sum_{n_y=-\frac{N_y}{2}+1}^{\frac{N_y}{2}} g(x,y,z)e^{-j(k_x x+k_y y)} \tag{1.86}$$

Along the wall normal direction z, the transformed signal $\hat{g}(k_x,k_y,z)$ is approximated through the sum of Chebyshev polynomials $T_n(z)$:

$$\hat{g}(k_x,k_y,z) = \sum_{n_z=0}^{N_z'} h(k_x,k_y,n_z)T_n(z) \tag{1.87}$$

where the prime indicate the first term halving. The Chebyshev polynomial of order n_z in z is defined as follows:

$$T_{nz}(z) = \cos\left[n_z \arccos(z)\right] \tag{1.88}$$

where n_z is one of the N_z Chebyshev modes and $-1 \leq z \leq 1$. The orthogonality property holds also for the Chebyshev polynomials and the inverse transform is:

$$\hat{h}(k_x, k_y, n_z) = \frac{2}{N_z} \sum_{n_z=0}^{N_z'} \hat{g}(k_x, k_y, z) T_n(z) \tag{1.89}$$

The variables described in the Chebishev space are mapped in the physical space according to the following mapping:

$$z = \cos\left(\frac{n_z \pi}{N_z}\right) \tag{1.90}$$

With adoption of Chebyshev polynomials for the approximation of the solution along the wall-normal direction, the spatial discretisation is characterised by a large resolution near the walls ($z = \pm 1$), where large velocity gradients need to be resolved. A complete review of the method can be find in [19] Concluding, adopting the transformations of Eqs. 1.83 - 1.87, the spectral representation of a three-dimensional signal is the following:

$$g(x, y, z, t) = \sum_{n_x=-\frac{N_x}{2}+1}^{\frac{1}{2}N_x} \sum_{n_y=-\frac{N_y}{2}+1}^{\frac{1}{2}N_y} \sum_{n_z=0}^{N_z'} \hat{h}(k_x, k_y, n_z, t) T_{n,z}(z) e^{j(k_x x + k_y y)} \tag{1.91}$$

Due to the presence of products taken in to the physical space, the computational algorithm needs the introduction of de-aliasing procedures also in the Chebyshev transforms; following [19] a the “2/3 rule” is applied, keeping only the first two thirds of the modes after the application of the pseudo-spectral multiplications.

1.5.3 Discretisation and solution of the equations

Velocity equation

Using the spectral representation of Sec. 1.5.2, Eq. 1.73 reads:

$$\begin{aligned}
\frac{\partial}{\partial t}\left(\frac{\partial^2}{\partial z^2} - k_{xy}^2\right)\hat{w} \quad &= \quad \left(\frac{\partial^2}{\partial z^2} - k_{xy}^2\right)\hat{S}_z \\
&- \quad \frac{\partial}{\partial z}\left(ik_x\hat{S}_x + ik_y\hat{S}_y + \frac{\partial}{\partial z}\hat{S}_z\right) \\
&+ \quad \frac{1}{Re_\tau}\left(\frac{\partial^2}{\partial z^2} - k_{xy}^2\right)\left(\frac{\partial^2}{\partial z^2} - k_{xy}^2\right)\hat{w} \quad (1.92)
\end{aligned}$$

where $k_{xy}^2 = k_x^2 + k_y^2$. The equation above stresses that the z derivatives are taken in a different way, due to the adoption of Chebyshev polynomials. Eq. 1.92 is discretised in time adopting an hybrid IMplicit EXplicit (IMEX) scheme: (i) a second-order Adams-Bashfort explicit scheme is adopted for the non-linear convective terms; (ii) the implicit Crank-Nicholson implicit scheme is applied to the diffusive operators. The time-discretised form of Eq. 1.92 reads:

$$\begin{aligned}
& \frac{1}{\Delta t}\left[\left(\frac{\partial^2}{\partial z^2} - k_{xy}^2\right)\hat{w}^{n+1} - \left(\frac{\partial^2}{\partial z^2} - k_{xy}^2\right)\hat{w}^{n}\right] = \\
& \frac{3}{2}\left(\frac{\partial^2}{\partial z^2} - k_{xy}^2\right)\hat{S}_z^{n} - \frac{1}{2}\left(\frac{\partial^2}{\partial z^2} - k_{xy}^2\right)\hat{S}_z^{n-1} \\
- & \frac{3}{2}\frac{\partial}{\partial z}\left(ik_x\hat{S}_x^{n} + ik_y\hat{S}_y^{n} + \frac{\partial}{\partial z}\hat{S}_z^{n}\right) \\
+ & \frac{1}{2}\frac{\partial}{\partial z}\left(ik_x\hat{S}_x^{n-1} + ik_y\hat{S}_y^{n-1} + \frac{\partial}{\partial z}\hat{S}_z^{n-1}\right) \\
+ & \frac{1}{Re_\tau}\left(\frac{\partial^2}{\partial z^2} - k_{xy}^2\right)\left(\frac{\partial^2}{\partial z^2} - k_{xy}^2\right)\frac{\hat{w}^{n+1} - \hat{w}^{n}}{2}
\end{aligned} \tag{1.93}$$

where superscripts $n-1$, n, $n+1$ indicate the three consecutive time levels $t - \Delta t$, t and $t + \Delta t$, respectively and Δt is the time-step. Eq. 1.93 is rearranged and, introducing the coefficient $\gamma = \Delta t / 2Re$, the following is obtained:

$$\begin{aligned}
& \left[1 - \gamma\left(\frac{\partial^2}{\partial z^2} - k_{xy}^2\right)\right]\left(\frac{\partial^2}{\partial z^2} - k_{xy}^2\right)\hat{w}^{n+1} = \\
+ & \frac{3\Delta t}{2}\left(\frac{\partial^2}{\partial z^2} - k_{xy}^2\right)\hat{S}_z^{n} - \frac{\Delta t}{2}\left(\frac{\partial^2}{\partial z^2} - k_{xy}^2\right)\hat{S}_z^{n-1} \\
- & \frac{3\Delta t}{2}\frac{\partial}{\partial z}\left(ik_x\hat{S}_x^{n} + ik_y\hat{S}_y^{n} + \frac{\partial}{\partial z}\hat{S}_z^{n}\right) \\
+ & \frac{\Delta t}{2}\frac{\partial}{\partial z}\left(ik_x\hat{S}_x^{n-1} + ik_y\hat{S}_y^{n-1} + \frac{\partial}{\partial z}\hat{S}_z^{n-1}\right) \\
+ & \left[\gamma\frac{\partial^2}{\partial z^2} + (1 - k_{xy}^2)\right]\left(\frac{\partial^2}{\partial z^2} - k_{xy}^2\right)\hat{w}^{n}
\end{aligned} \tag{1.94}$$

The discretized form ot the continuity equation is:

$$ik_x\hat{u} + ik_y\hat{v} + \frac{\partial w}{\partial z} = 0 \tag{1.95}$$

substituting Eq. 1.95 into Eq. 1.94 and introducing the coefficient $\lambda^2 = (1+\gamma k_{xy}^2)/\gamma$, the following is obtained:

$$\begin{aligned}
- & \gamma\left(\frac{\partial^2}{\partial z^2}-\lambda^2\right)\left(\frac{\partial^2}{\partial z^2}-k_{xy}^2\right)\hat{w}^{n+1} = \\
- & k_{xy}^2\left(\frac{3}{2}\hat{S}_z^n-\frac{1}{2}\hat{S}_z^{n-1}\right)\Delta t - k_{xy}^2\left[\gamma\frac{\partial^2}{\partial z^2}+\left(1-\gamma k_{xy}^2\right)\right]\hat{w}^n \\
- & \frac{\partial}{\partial z}ik_x\left(\frac{3}{2}\hat{S}_x^n-\frac{1}{2}\hat{S}_x^{n-1}\right)\Delta t - \frac{\partial}{\partial z}ik_x\left(\gamma\frac{\partial^2}{\partial z^2}+\left(1-\gamma k_{xy}^2\right)\right)\hat{u}^n \\
- & \frac{\partial}{\partial z}ik_y\left(\frac{3}{2}\hat{S}_y^n-\frac{1}{2}\hat{S}_y^{n-1}\right)\Delta t - \frac{\partial}{\partial z}ik_y\left(\gamma\frac{\partial^2}{\partial z^2}+\left(1-\gamma k_{xy}^2\right)\right)\hat{v}^n
\end{aligned} \tag{1.96}$$

The historical terms $\hat{H}_x^n$, $\hat{H}_y^n$ and $\hat{H}_z^n$ are defined as follows:

$$\begin{aligned}
\hat{H}_x^n &= \left(\frac{3}{2}\hat{S}_x^n-\frac{1}{2}\hat{S}_x^{n-1}\right)\Delta t+\left[\gamma\frac{\partial^2}{\partial z^2}+\left(1-\gamma k_{xy}^2\right)\right]\hat{u}^n \\
\hat{H}_y^n &= \left(\frac{3}{2}\hat{S}_y^n-\frac{1}{2}\hat{S}_y^{n-1}\right)\Delta t+\left[\gamma\frac{\partial^2}{\partial z^2}+\left(1-\gamma k_{xy}^2\right)\right]\hat{v}^n \\
\hat{H}_z^n &= \left(\frac{3}{2}\hat{S}_z^n-\frac{1}{2}\hat{S}_z^{n-1}\right)\Delta t+\left[\gamma\frac{\partial^2}{\partial z^2}+\left(1-\gamma k_{xy}^2\right)\right]\hat{w}^n
\end{aligned} \tag{1.97}$$

introducing Eq. 1.97, Eq. 1.96 reads:

$$\left(\frac{\partial^2}{\partial z^2}-\lambda^2\right)\left(\frac{\partial^2}{\partial z^2}-k_{xy}^2\right)\hat{w}^{n+1}=\frac{1}{\gamma}\left[k_{xy}^2\hat{H}_z^n+\frac{\partial}{\partial z}\left(ik_x\hat{H}_x^n+ik_y\hat{H}_y^n\right)\right] \tag{1.98}$$

Collecting $\hat{H}^n = k_{xy}^2\hat{H}_z^n + \frac{\partial}{\partial z}(ik_x\hat{H}_x^n + ik_y\hat{H}_y^n)$ the final form of the discretised Eq. 1.73 is obtained:

$$\left(\frac{\partial^2}{\partial z^2}-\lambda^2\right)\left(\frac{\partial^2}{\partial z^2}-k_{xy}^2\right)\hat{w}^{n+1}=\frac{\hat{H}^n}{\gamma} \tag{1.99}$$

We can introduce the auxiliary variable $\hat{\theta} = \left(\frac{\partial^2}{\partial z^2}-k_{xy}^2\right)\hat{w}^{n+1}$ and the 4^{th}-order equation can be split in two 2^{nd}-order equations:

$$\left(\frac{\partial^2}{\partial z^2}-\lambda^2\right)\hat{\theta}=\frac{\hat{H}^n}{\gamma} \tag{1.100}$$

$$\left(\frac{\partial^2}{\partial z^2}-k_{xy}^2\right)\hat{w}^{n+1}=\hat{\theta} \tag{1.101}$$

Eq. 1.100 and Eq. 1.101 can be solved imposing different boundary conditions, for a closed channel (no-slip at both the walls) the following BC are applied.

$$\hat{w}^{n+1}(\pm 1)=0 \qquad \frac{\partial \hat{w}^{n+1}}{\partial z}(\pm 1)=0 \tag{1.102}$$

While for an open channel the following boundary conditions are applied.

$$\hat{w}^{n+1}(-1) = 0, \qquad \frac{\partial \hat{w}^{n+1}}{\partial z}(-1) = 0 \tag{1.103}$$

$$\hat{w}^{n+1}(+1) = 0, \qquad \frac{\partial^2 \hat{w}^{n+1}}{\partial z^2}(+1) = 0 \tag{1.104}$$

Both the boundary conditions are obtained from the non-slip or free-slip condition at the wall coupled with the continuity equation. The solution of Eq. 1.99 requires a set of boundary conditions on $\hat{\theta}$ that lack in the physical model definition, only for the free-slip we can have a boundary condition on $\hat{\theta}$, to circumvent this problem, $\hat{\theta}$ is rewritten as follows:

$$\hat{\theta} = \hat{\theta}_1 + \hat{A}\theta_2 + \hat{B}\theta_3 \tag{1.105}$$

where $\hat{A}$ and $\hat{B}$ are complex constants to be determined. The three components, $\hat{\theta}_1$, θ_2 and θ_3 are the particular solution and two homogeneous solution of Eq. 1.100, respectively. Their solution is obtained as follows:

$$\left(\frac{\partial^2}{\partial z^2} - \lambda^2\right)\hat{\theta}_1 = \frac{\hat{H}^n}{\gamma} \qquad \hat{\theta}_1(-1) = 0 \qquad \hat{\theta}_1(+1) = 0 \tag{1.106}$$

$$\left(\frac{\partial^2}{\partial z^2} - \lambda^2\right)\theta_2 = 0 \qquad \theta_2(-1) = 1 \qquad \theta_2(+1) = 0 \tag{1.107}$$

$$\left(\frac{\partial^2}{\partial z^2} - \lambda^2\right)\theta_3 = 0 \qquad \theta_3(-1) = 0 \qquad \theta_3(+1) = 1 \tag{1.108}$$

In a similar way, also $\hat{w}^{n+1}$ is rewritten as a sum of a particular solution $\hat{w}_1$ and two homogeneous solutions w_2, w_3:

$$\hat{w}^{n+1} = \hat{w}_1 + \hat{A}w_2 + \hat{B}w_3 \tag{1.109}$$

Similarly to the solution of $\hat{\theta}$, the solutions for $\hat{w}_1$, w_2 and w_3 can be obtained applying the no-slip BC:

$$\left(\frac{\partial^2}{\partial z^2} - k_{xy}^2\right)\hat{w}_1 = \hat{\theta} \qquad \hat{w}_1(-1) = 0 \qquad \hat{w}_1(+1) = 0 \tag{1.110}$$

$$\left(\frac{\partial^2}{\partial z^2} - k_{xy}^2\right)w_2 = \theta_1 \qquad w_2(-1) = 0 \qquad w_2(+1) = 0 \tag{1.111}$$

$$\left(\frac{\partial^2}{\partial z^2} - k_{xy}^2\right)w_3 = \theta_2 \qquad w_3(-1) = 0 \qquad w_3(+1) = 0 \tag{1.112}$$

The unknown constants $\hat{A}$ and $\hat{B}$ are determined, for a closed channel, applying the $\partial\hat{w}^{n+1}/\partial z = 0$ boundary condition:

$$\frac{\partial\hat{w}_1}{\partial z}(-1) + \hat{A}\frac{\partial w_2}{\partial z}(-1) + \hat{B}\frac{\partial w_3}{\partial z}(-1) = 0 \tag{1.113}$$

$$\frac{\partial\hat{w}_1}{\partial z}(+1) + \hat{A}\frac{\partial w_2}{\partial z}(+1) + \hat{B}\frac{\partial w_3}{\partial z}(+1) = 0 \tag{1.114}$$

Or for an open channel:

$$\frac{\partial\hat{w}_1}{\partial z}(-1) + \hat{A}\frac{\partial w_2}{\partial z}(-1) + \hat{B}\frac{\partial w_3}{\partial z}(-1) = 0, \tag{1.115}$$

$$\frac{\partial^2\hat{w}_1}{\partial z^2}(+1) + \hat{A}\frac{\partial^2 w_2}{\partial z^2}(+1) + \hat{B}\frac{\partial^2 w_3}{\partial z^2}(+1) = 0 \tag{1.116}$$

Alternatively the boundary conditions at the free-slip wall (1.116) can be directly forced on the solution of $\hat{\theta}$. From Eqs. 1.113 - 1.116, $\hat{w}^{n+1}$ is obtained, the solutions of Eqs. 1.100 - 1.100 are obtained adopting the Chebysev-Tau solution algorithm proposed in [92] and the resulting tridiagonal equations system is solved adopting the Gauss elimination procedure.

Vorticity equation

Using the spectral representation of Sec. 1.5.2, Eq. 1.72 reads:

$$\frac{\partial\hat{\omega_z}}{\partial t} = ik_x\hat{S}_y - ik_y\hat{S}_x + \frac{1}{Re_\tau}\left(\frac{\partial^2}{\partial z^2} - k_{xy}^2\right)\hat{\omega_z} \tag{1.117}$$

Where as before $k_{xy}^2 = k_x^2 + k_y^2$. Vorticity equation as the velocity equation is discretised in time adopting an hybrid IMplicit EXplicit (IMEX) scheme. i) a second-order Adams-Bashfort scheme is used for the non-linear terms; ii) an implicit Crank-Nicholson is used for the diffusive term. Using this time discretisation scheme, the equation became:

$$\begin{aligned}\frac{\hat{\omega_z}^{n+1} - \hat{\omega_z}^{n}}{\Delta t} &= \frac{3}{2}\left(ik_x\hat{S_y^n} - ik_y\hat{S_x^n}\right)\\ &- \frac{1}{2}\left(ik_x\hat{S_y^{n-1}} - ik_y\hat{S_x^{n-1}}\right)\\ &+ \frac{1}{2Re}\left(\frac{\partial^2}{\partial z^2} - k_{xy}^2\right)\left(\hat{\omega_z}^{n+1} - \hat{\omega_z}^{n}\right)\end{aligned} \tag{1.118}$$

Where superscripts $n-1$, n, $n+1$ indicate the three consecutive time levels $t-\Delta t$, t and $t+\Delta t$, respectively. Using the definition of $\hat{\omega_z} = ik_x\hat{u}_2 - ik_y\hat{u}_1$

the equation can be rewritten as:

$$\begin{aligned}\frac{\hat{\omega_z}^{n+1}-\hat{\omega_z}^{n}}{\Delta t} &= ik_x\left[\left(\frac{3}{2}\hat{S_y}^{n}-\frac{1}{2}\hat{S_y}^{n}\right)\Delta t+\frac{1}{2Re}\left(\frac{\partial^2}{\partial z^2}-k_{xy}^2\right)\hat{v}^n\right]\\ &- ik_y\left[\left(\frac{3}{2}\hat{S_x}^{n}-\frac{1}{2}\hat{S_x}^{n}\right)\Delta t+\frac{1}{2Re}\left(\frac{\partial^2}{\partial z^2}-k_{xy}^2\right)\hat{u}^n\right]\\ &+ \frac{1}{2Re}\left(\frac{\partial^2}{\partial z^2}-k_{xy}^2\right)\hat{\omega_z}^{n+1}\end{aligned} \tag{1.119}$$

Defining γ as before, using the previously defined historical terms $\hat{H}_y^n$ and $\hat{H}_x^n$ and collecting $\widehat{\omega^{n+1}}$ on the left size we obtain:

$$\left(\frac{\partial^2}{\partial z^2}-\beta^2\right)\hat{\omega}_z^{n+1}=-\frac{1}{\gamma}\left[ik_x\hat{H}_y^n-ik_y\hat{H}_x^n\right] \tag{1.120}$$

Where β has been defined as:

$$\beta^2=\frac{1+\gamma k_{xy}^2}{\gamma} \tag{1.121}$$

The solution of Eq. 1.120 is obtained adopting the Chebyshev-Tau algorithm with the following BC for a closed channel:

$$\hat{\omega}_z^{n+1}(\pm 1)=0 \tag{1.122}$$

Or for an open channel:

$$\hat{\omega}_z^{n+1}(-1)=0 \qquad \frac{\partial\hat{\omega}_z^{n+1}}{\partial z}(+1)=0 \tag{1.123}$$

The resulting tridiagonal equations system is then solved adopting a Gauss elimination technique. Once the wall-normal vorticity component $\hat{\omega}_z$ is known, the other two velocity components $\hat{u}^{n+1}$ and $\hat{v}^{n+1}$ can be derived from the spectral representation of the vorticity definition and the spectral representation of the continuity equation:

$$-ik_y\hat{u}^{n+1}+ik_x\hat{v}^{n+1}=\hat{\omega}_z^{n+1} \tag{1.124}$$

$$-ik_x\hat{u}^{n+1}+ik_y\hat{v}^{n+1}=\frac{\partial\hat{w}^{n+1}}{\partial z} \tag{1.125}$$

Cahn-Hilliard equation

Eq. 1.79 is discretised in space adopting the spectral representation shown in Sec. 1.5.2 and applied in Sec. 1.5.3:

$$\begin{aligned}\frac{\partial\hat{\phi}}{\partial t} &= \hat{S}_\phi+s\frac{Ch^2}{Pe}\left(\frac{\partial^2}{\partial z^2}-k_{xy}^2\right)\hat{\phi}\\ &- \frac{Ch^2}{Pe}\left(\frac{\partial^2}{\partial z^2}-k_{xy}^2\right)\left(\frac{\partial^2}{\partial z^2}-k_{xy}^2\right)\hat{\phi}\end{aligned} \tag{1.126}$$

The solution of the Cahn-Hilliard is characterised by high frequency harmonics that need to be damped in order to keep the solution bounded. The adoption of weakly damping schemes, such as the Crank-Nicholson adopted for the velocity field equations leads to aliased solutions [8]. For this reason, following [193], a 1^{st}-order Backward Difference Formula (BDF) is adopted. In particular the non linear convective S_ϕ term is discretised adopting a 2^{nd} order Adams-Bashfort:

$$\begin{aligned}\frac{\hat{\phi}^{n+1}-\hat{\phi}^{n}}{\Delta t} &= \frac{3}{2}\hat{S}_\phi^{n}-\frac{1}{2}\hat{S}_\phi^{n-1}+s\frac{Ch^2}{Pe}\left(\frac{\partial^2}{\partial z^2}-k_{xy}^2\right)\hat{\phi}^{n+1}\\ &- \frac{Ch^2}{Pe}\left(\frac{\partial^2}{\partial z^2}-k_{xy}^2\right)\left(\frac{\partial^2}{\partial z^2}-k_{xy}^2\right)\hat{\phi}^{n+1} \qquad (1.127)\end{aligned}$$

Introducing the coefficient $\gamma_\phi = (\Delta t Ch^2)/Pe$, Eq. 1.127 yields:

$$\left[\frac{1}{\gamma_\phi}-s\left(\frac{\partial^2}{\partial z^2}-k_{xy}^2\right)+\left(\frac{\partial^2}{\partial z^2}-k_{xy}^2\right)^2\right]\hat{\phi}^{n+1}=\frac{\hat{H}_\phi}{\gamma_\phi} \qquad (1.128)$$

where the historical term $\hat{H}_\phi$ has been introduced:

$$\frac{\hat{H}_\phi}{\gamma_\phi}=\frac{1}{\gamma_\phi}\left(\hat{\phi}^{n}+\frac{3\Delta t}{2}\hat{S}_\phi^{n}-\frac{\Delta t}{2}\hat{S}_\phi^{n-1}\right) \qquad (1.129)$$

We can decompose Eq. 1.128, a 4^{th} order equation, in two equivalent second order equations.

$$\begin{aligned}&\left[\frac{1}{\gamma_\phi}-s\left(\frac{\partial^2}{\partial z^2}-k_{xy}^2\right)+\left(\frac{\partial^2}{\partial z^2}-k_{xy}^2\right)^2\right]=\\ &\left[\left(\frac{\partial^2}{\partial z^2}-k_{xy}^2-\lambda_1\right)\left(\frac{\partial^2}{\partial z^2}-k_{xy}^2-\lambda_2\right)\right] \qquad (1.130)\end{aligned}$$

The values of λ_1 and λ_2 can be obtained from the equation:

$$\gamma_\phi\lambda^2 - s\gamma_\phi\lambda + 1 = 0 \qquad (1.131)$$

Obtaining:

$$\lambda_{1/2} = -\frac{s}{2} \pm \frac{\sqrt{s^2\gamma_\phi^2-4\gamma_\phi}}{2\gamma_\phi} \qquad (1.132)$$

The root square poses some constraints on the choice of the value of s, in particular for having two real solutions must be:

$$s \geq \sqrt{\frac{4}{\gamma}} = \sqrt{\frac{4Pe}{\Delta t Ch^2}} \qquad (1.133)$$

The choice of two coincident solutions $\lambda_1 = \lambda_2 = -s/2 = \sqrt{Pe/\Delta t Ch^2}$ guarantees the achievement of the maximum stability, under this assumption the equation for ϕ is:

$$\left(\frac{\partial^2}{\partial z^2} - k_{xy}^2 + \frac{s}{2}\right)^2 \hat{\phi}^{n+1} = \frac{\hat{H}_\phi}{\gamma_\phi} \tag{1.134}$$

Defining the auxiliary variable $\theta_\phi = s\phi/2 + \nabla^2\phi$, the 4^{th} order Eq. 1.128 is now splitted in two 2^{nd} order equations:

$$\left(\frac{\partial^2}{\partial z^2} - \delta^2\right) \hat{\theta}_\phi = \frac{\hat{H}_\phi}{\gamma_\phi} \tag{1.135}$$

$$\left(\frac{\partial^2}{\partial z^2} - \delta^2\right) \hat{\phi}^{n+1} = \hat{\theta}_\phi \tag{1.136}$$

Where $\delta^2 = k_{xy}^2 - s/2$. Eqs. 1.135 and 1.136 are solved imposing the following boundary conditions that emerge imposing a normal contact angle for the interface at the walls and a no-flux of chemical potential through the walls.

$$\frac{\partial \hat{\phi}^{n+1}}{\partial z}(\pm 1) = 0 \qquad \frac{\partial^3 \hat{\phi}^{n+1}}{\partial z^3}(\pm 1) = 0 \tag{1.137}$$

The boundary conditons on $\hat{\theta}_\phi$ are on the first and third derivative, so there is no need to apply the influence matrix method, since:

$$\frac{\partial}{\partial z}\left(\frac{\partial^2}{\partial z^2} - \delta^2\right)\hat{\phi}^{n+1} = \frac{\partial^3 \hat{\phi}^{n+1}}{\partial z^3} = \frac{\partial \hat{\theta}_\phi^{n+1}}{\partial z} \tag{1.138}$$

As consequence, Eq. 1.135 is solved using the following boundary conditions:

$$\frac{\partial \hat{\theta}_\phi^{n+1}}{\partial z}(\pm 1) = 0 \tag{1.139}$$

and Eq. 1.136 is solved using the following boundary conditions:

$$\frac{\partial \hat{\phi}}{\partial z}(\pm 1) = 0 \tag{1.140}$$

The solutions of Eqs. 1.135 - 1.136 are obtained adopting the Chebyshev-Tau solution algorithm proposed in [92] and the resulting tridiagonal equations system is solved through a Gauss elimination procedure.

Surfactant equation

The transport equation of the surfactant is discretised in space adopting the spectral representation shown in Sec. 1.5.2 and applied in Sec.1.5.3:

$$\frac{\partial \hat{\psi}}{\partial t} = \hat{S}_\psi + \frac{Pi}{Pe_\psi}\left(\frac{\partial^2}{\partial z^2} - k_{xy}^2\right)\hat{\psi} \tag{1.141}$$

The equation for the surfactant is a second order equation which is coupled via the non linear term to the Navier-Stokes and Cahn-Hiliard equation, furthermore the use of a non linear mobility can lead to high frequency harmonics, that need to be damped in order to keep the solution bounded. For this reason, following the same procedure used for the Cahn-Hilliard equation a 1^{st}-order Backward Difference Formula (BDF) is adopted. In particular the non linear convective S_ψ term is discretised adopting a 2^{nd} order Adams-Bashfort:

$$\frac{\hat{\psi}^{n+1}-\hat{\psi}^{n}}{\Delta t} = \frac{3}{2}\hat{S}_{\psi}^{n}-\frac{1}{2}\hat{S}_{\psi}^{n-1}+\frac{Pi}{Pe}\left(\frac{\partial^2}{\partial z^2}-k_{xy}^2\right)\hat{\psi}^{n+1} \tag{1.142}$$

Defining the coefficient $\gamma_\psi = (\Delta t Pi)/Pe_\psi$ the equation can be recasted as::

$$\left[\frac{1}{\gamma_\psi}-\left(\frac{\partial^2}{\partial z^2}-k_{xy}^2\right)\right]\hat{\psi}^{n+1}=\frac{\hat{H}_\psi}{\gamma_\psi} \tag{1.143}$$

Where the historical term $\hat{H}_\psi$ has been defined:

$$\hat{H}_\psi=\left(\hat{\psi}^{n}+\frac{3\Delta t}{2}\hat{S}_{\psi}^{n}-\frac{\Delta t}{2}\hat{S}_{\psi}^{n-1}\right) \tag{1.144}$$

We can define $\iota^2=(\gamma_\psi k_{xy}^2+1)/\gamma_\psi$ and we finally obtain an equation that can be solved using an Helmotz-solver with suitable boundary conditions:

$$\left(\frac{\partial^2}{\partial z^2}-\iota^2\right)\hat{\psi}^{n+1}=-\frac{\hat{H}_\psi}{\gamma_\psi} \tag{1.145}$$

Eq. 1.145 has been solved using a no-flux boundary conditions either for ψ that for μ_ψ as previously done in other works [153, 112].

$$\frac{\partial\hat{\psi}}{\partial z}(\pm 1)=0 \tag{1.146}$$

Boundary conditions of Eq. 1.146 leads to a no-flux boundary conditions for μ_ψ.

$$\frac{\partial \mu\psi}{\partial z}(\pm 1)=0 \tag{1.147}$$

Boundary conditions proposed by Eqs. 1.146 - 1.147 leads at the time conservation of the total mass of surfactant over time.

Code Implementation

The numerical algorithm presented in Sec. 2.3 for the solution of equations presented in Sec. 1.4 has been implemented in a in-house code using Fortran as programming language. The code is parallelised using a MPI paradigm. The parallelisation is based on a 2D domain decomposition. Considering a

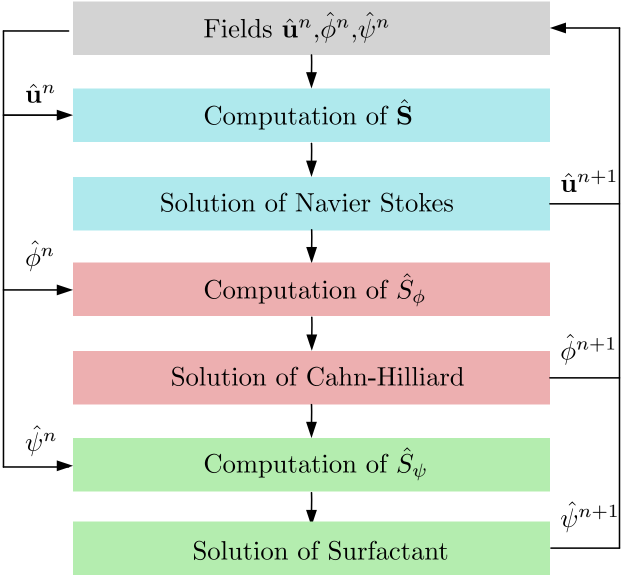

FIGURE 1.7 – Scheme of the numerical solver used. From the initial fields $\hat{\mathbf{u}}^n$, $\hat{\psi}^n$,$\hat{\psi}^n$ at the step n, for each equation the non linear terms are computed in physical space and then back-transformed in the spectral space. Once this operation is completed, the unkown of the equation at the time step $n+1$ can be obtained using the Helmholtz solver.

generic variable θ, in the physical space, each process will have a pencil of the domain with dimension $N_x \times N_{yp} \times N_{zp}$. Where N_{yp} and N_{zp} are a fraction of the total number of nodes used along y and z directions respectively. Since a global method is used to describe the unknown, to perform a 3D transform (Fourier-Fourier-Chebyshev) the pencil must be reoriented along the three directions. The pencils are reoriented using MPI-communications; this operation is required during the computation of the non linear terms $\mathbf{S}$, S_ϕ and S_ψ. A schematic representation of the steps required to compute a 3D transform is shown in Fig. 1.8.

1.6 Validation

In this section, the governing equations are solved using the numerical method proposed in Sec. 1.5. The code implementation is validated considering the problem of a droplet in shear flow.

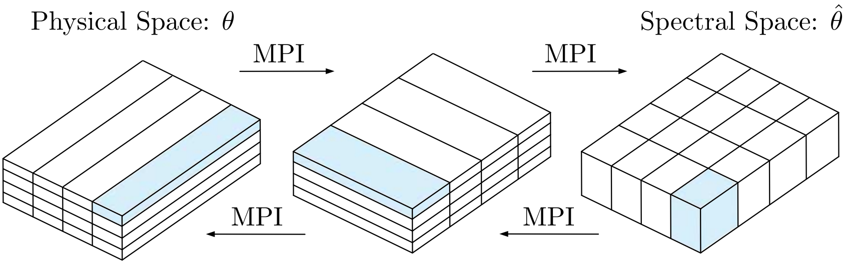

FIGURE 1.8 – From the right, the unknown is in the physical space, θ, the FFT along the x direction is computed. Then, through MPI-communications, the pencil is reoriented and the FFT along the y direction is performed. Last, the pencil is again reoriented and the Chebyshev transform along the z direction is computed. After these steps, the unknown is described in the spectral space, $\hat{\theta}$. The inverse transform can be computed following the same steps but in the opposite direction.

1.6.1 Droplet in shear flow

The method proposed is used to analyse the behaviour of a single droplet posed in a laminar shear flow. A spherical droplet is released in the centre of a channel bounded by two walls, $z = \pm h$ which move at constant velocity but in opposite directions, Fig.1.9. The shear flow modifies the droplet's shape and after an initial transient, the droplet reaches a new steady-state shape. The new shape is determined by the competition between surface tension forces, which try to restore the spherical shape, and the viscous forces that elongate the droplet. The relative importance of these forces is expressed by two parameters, the capillary number, Ca, and the viscosity ratio, λ, defined as follows:

$$Ca = \frac{We}{Re_\tau}\frac{d}{2h} = \frac{u_\tau \eta_c d}{\sigma 2h} \qquad \lambda = \frac{\eta_d}{\eta_c} \tag{1.148}$$

The capillary number, Ca, describes the relative importance of the viscous forces compared to the surface tension ones. The viscosity ratio λ is the ratio between the droplet's viscosity, η_d, and the external fluid viscosity, η_c. An analytical solution of the problem was obtained by [167, 39] and was subsequently corrected by [151] to consider the wall effects. Taylor, using a sharp interface approach, solved the unbounded creeping flow equations in the limit of vanishing droplet's deformation. Under these hypothesis, the steady-state shape of the droplet is an ellipsoid, with major axes contained in the shear gradient plane. The droplet is tilted according to the velocity profile. To estimate the magnitude of the deformation, a deformation parameter, D, is defined as:

$$D = \frac{L - B}{L + B} \tag{1.149}$$

Where L and B are the dimensions of the two principal axis of the deformed droplet, Fig. 1.9. Once the droplet's shape is known, the following expression for the parameter D is obtained [167, 39, 151]

$$D = \frac{16 + 19\lambda}{16(1+\lambda)} Ca \left[1 + C_{SH} \frac{3.5}{2} \left(\frac{d}{4} \right)^3 \right] \tag{1.150}$$

where C_{SH} is a numerical coefficient equal to 5.6996 [151]. As can been seen from Eq. 1.150, the droplet deformation parameter D is a function of the Ca and of the viscosity ratio λ. The equation is valid in the limit of vanishing deformations, $D < 0.3$. From Eq. 1.150 can be observed that the deformation parameter D is a linear function of Ca. For small Ca (high surface tension) the droplet will keep a quasi-spherical shape. By opposite, considering large Ca (low surface tension), higher deformations are obtained. If the capillary exceeds a threshold, $Ca > Ca_{cr}$, the droplet can undergoes a breakage [64]. The viscosity ratio λ enters into the picture modifying the coefficient. For $\lambda < 1$, deformation is reduced since less shear stress is transmitted through the interface, vice-versa for $\lambda > 1$ is increased. When surfactant is taken into account, the droplet's shape is influenced by three new additional effects: (i) surfactant decreases the average surface tension and deformation will increase, (ii) surfactant accumulates on the droplet tips (stagnation points) and further increases the deformation, (iii) inhomogeneous surfactant distribution gives rise to tangential stresses at the interface which hinder the deformation [161, 159, 177]. When a surfactant-laden droplet is considered, as in previous works [161, 159], an effective capillary $Ca_e = (\sigma_0/\sigma_{av})Ca$ is used to compute the theoretical value of the deformation. The effective capillary number, Ca_e, accounts for the average reduction of the surface tension produced by the surfactant.

1.6.2 Problem definition

A spherical droplet, diameter $d = 0.8h$, is released in the centre of the channel, Fig. 1.9. A linear velocity profile $u(z)$ is imposed. The two walls move in opposite directions with a velocity $|u(\pm h)| = 1$ along the x direction, the other two velocity components are zero, $v(\pm h) = w(\pm h) = 0$. The value of the Reynolds number has been chosen to ensure complete creeping flow conditions: $Re_\tau = 0.1$. The computational domain used is two-dimensional channel with dimensions $2\pi h \times 2h$ along the x and z direction. A number of collocation points, $N_x \times N_y$ equal to 512×513 has been used. In order to describe the interface with at least three mesh points, Cahn number has been set to $Ch = 0.02$, following [120], Peclet number has been set to $Pe_\phi = 3/Ch^{-1} = 150$. When a surfactant-laden droplet is considered, a Peclet number, $Pe_\psi = 100$ has been used. This value of Pe_ψ leads to a surfactant distribution dominated by the convective phenomena. This behaviour is common for the surfactants [159]. Following [52], $Pi = 1.35$

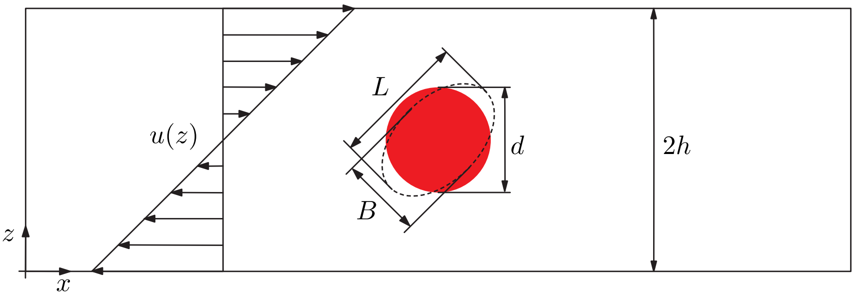

FIGURE 1.9 – Single droplet of diameter $d = 0.8h$ in shear flow. The initial shape of the droplet is reported with a full red circle. The final steady-state shape (dashed line) and the relative principal axis of the deformed droplet, L and B, are reported. The flow field is a linear velocity profile, $v(z)$.

and $E_x = 0.117$ have been set. The amount of surfactant present in the system is tuned acting on the bulk surfactant concentration ψ_b, two different values of ψ_b have been considered, $\psi_b = 0.01$ and $\psi_b = 0.02$. The elasticity number has been set to $\beta_s = 0.50$. The parameters Re_τ, Ch and Pe_ϕ are kept constant in all the cases considered. Both the order parameters ϕ and ψ are initialised with their equilibrium profiles.

1.6.3 Results

The results obtained are here presented and discussed. We first consider a clean droplet, Sec. 1.6.3. The effect of Ca and λ on the droplet's deformation are analysed and compared against the analytical relation [167, 39, 151]. Then, surfactant-laden droplets with different bulk surfactant concentrations ψ_b have been considered, Sec. 1.6.4

Clean droplet

The surface tension and viscosity contrast representations are here validated. Different values of Ca and λ have been used. After an initial transient, the droplet reaches a new steady-state shape and the deformation parameter D is computed. The values obtained are compared against the analytical relation of [167, 39, 151]. Following [167, 39, 151], for both the λ, the analytic relation between D and Ca is linear but with a different coefficient. For the two values of λ considered the relations are the following:

$$D = \begin{cases} \lambda = 1.0 & 1.1813Ca \\ \lambda = 0.1 & 1.0982Ca \end{cases} \tag{1.151}$$

A summary of the parameters used is reported in Tab. 1.1, for each Ca, two different values of λ have been tested, $\lambda = 1.0$ and $\lambda = 0.1$. The results

	Ca					
	0.0625	0.125	0.1875	0.250	0.375	0.500
$\lambda = 1.0$	X1	X2	X3	X4	X5	X6
$\lambda = 0.1$	Y1	Y2	Y3	Y4	Y5	Y6

TABLE 1.1 – Parameters used for the simulations of a single droplet in shear flow. For each value of the Ca, two different viscosity ratio λ have been considered.

obtained are reported in Fig. 1.1. In Fig. 1.1(a) the results for $\lambda = 1.0$ are shown, for these cases in the whole range of Ca, an excellent agreement is found. Despite the small deformation theory limits the validity to $D < 0.3$, good results are found up to $D < 0.4$, at $Ca = 0.50$ the analytical relation slightly overestimate the deformation. A similar behaviour is obtained for $\lambda = 0.1$, Fig. 1.1(b). For these cases, Y-series, the numerical results are slight larger than the ones predicted by the theory but a good agreement can be still observed. The slight increase of the error, especially for $\lambda = 0.1$, can be addressed to possible wall effects [53] and to the minor accuracy offered by the theoretical relation. The results obtained match the ones obtained numerically with different interface tracking methods, as VOF [111], LS [186] or PFM [163] and experimentally [44, 64, 155, 29].

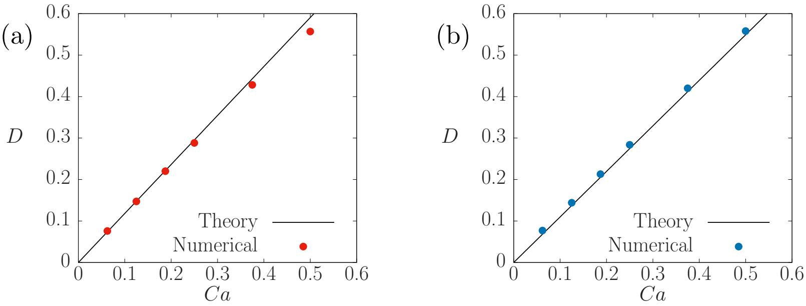

FIGURE 1.10 – In panel (a) and panel (b) the deformation parameter D is plot against Ca. Panel (a) refers to $\lambda = 1.0$, matched viscosity. Panel (b) refers to $\lambda = 0.1$, the droplet's fluid is less viscous than the external one. Numerical results are reported with spherical markers (red for $\lambda = 1$ and blue for $\lambda = 0.1$). The analytical relation is reported with a continuous black line.

1.6.4 Surfactant-laden droplet in shear flow

The extension of PFM to the surfactant tracking is here tested. In order to fulfil the hypothesis of small deformations only the four lowest Ca have been considered, from $Ca = 0.0625$ to $Ca = 0.250$, cases X1-X4 of Tab. 1.1. For each Ca, two bulk surfactant concentrations have been considered, $\psi_b = 0.01$ and $\psi_b = 0.02$. Since the parameters Pi and E_x are kept fixed, the bulk surfactant concentration ψ_b sets the amount of surfactant present

	Ca			
	0.0625	0.125	0.1875	0.250
Clean	X1	X2	X3	X4
Surfactant-laden ($\psi_b = 0.01$)	A1	A2	A3	A4
Surfactant-laden ($\psi_b = 0.02$)	B1	B2	B3	B4

Table 1.2 – Parameters used for the simulations of a single droplet in shear flow. For each Ca, a clean and two surfactant-laden cases have been considered. The surfactant-laden cases differ for the amount of surfactant present, tuned acting on the bulk surfactant concentration ψ_b.

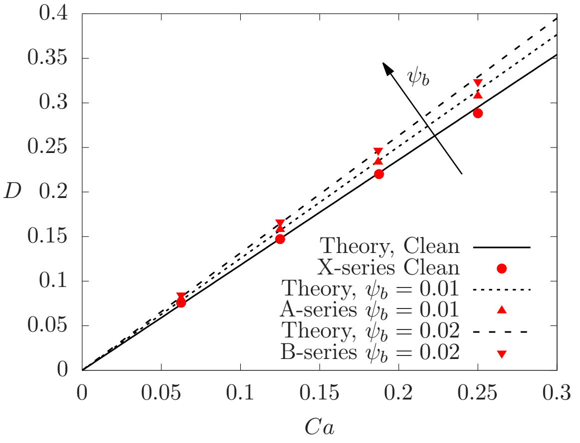

Figure 1.11 – Comparison of numerical and analytical results for the deformation parameter D; analytical results for a clean droplet are reported with black line, whereas numerical ones are identified by red circles. For $\psi_b = 0.01$, a double dashed line identifies the analytical results and the numerical ones are identified by upward red triangles. Similarly for $\psi_b = 0.02$, a dashed line identifies the theoretical results and the numerical ones are reported whit downward red triangles.

in the system. An overview of the parameters is reported in Tab. 1.2. The results obtained for the deformation parameter D are reported in Fig. 1.11. The ones obtained from the clean droplets (red spherical markers), X-series, have been already discussed and are reported as reference. The results obtained from the cases A1-A4 and B1-B4, surfactant-laden droplets, have been compared with the ones predicted by the analytic relation using Ca_e, Eq. 1.150. For both the surfactant-laden cases the analytical relation well predicts the results obtained from the simulations. Even for these cases, at the highest Ca (A4-B4), the analytic relation slightly over-predicts the numerical result. Interestingly, the three surfactant-induced effects offset each other. Using the effective capillary, Ca_e, in Eq. (1.150), a good prediction of the deformation parameter D can be obtained. The results match those obtained using different numerical approaches [18, 54, 168, 87, 58] and experiments [172, 75, 74].

2

Viscosity-modulated breakup and coalescence of drops in bounded turbulence

Reproduced in part from:

A. Roccon, M. De Paoli, F.Zonta and A. Soldati, Viscosity-modulated breakup and coalescence of large drops in bounded turbulence, Phys. Rev. Fluids, (2017).

2.1 Problem definition

Prediction of breakup and coalescence rates of a swarm of liquid drops immersed in a turbulent liquid flow (liquid/liquid emulsion) is crucially dependent on a number of hard-to-tackle factors. Among many others these include turbulence, turbulence/interface interactions, surface tension effects and viscosity gradients. Each single of these effects has a specific action on breakup and coalescence, and we can envision drops dynamics as the ultimate result of a complex competition between destabilising and stabilising effects. Destabilising effects are primarily due to the combined effects of fluctuating inertial and shear terms acting at the drops interface. Stabilising effects are due to surface tension, which is a restoring force acting to preserve drops sphericity. The outcome of this competition determines drops deformation, breakup and coalescence. In this picture, viscosity gradients across the interface of the drops can act as modulators of the localised shear stresses and can amplify or damp the initial turbulence perturbations to the point of changing profoundly the final result. Drops coalescence and breakup is of paramount importance in many environmental and industrial applications, from transport of pollutant drops in water bodies [184] to hydrocarbon separation or oil-water emulsions in chemical plants and petroleum industry [82, 32, 3]. Here, the focus is on the liquid-liquid emulsions, in which drops of one phase are dispersed within the other phase. In this instance, the knowledge of the drops number density and/or the drops interface extension is a key parameter to optimise the design of efficient oil separators, in which drops coalescence should be promoted and drops fragmentation reduced. For drops breakup in turbulence, literature dates back to the seminal work of [69], who modelled the mechanism of liquid drops splitting in a turbulent gas environment. Since the fundamental physics of drops splitting in gas-liquid or liquid-liquid configurations is controlled by the same parameters, results obtained for the gas-liquid case have been historically (and successfully) applied to the liquid-liquid case as well. In accordance with [69], drop breakup occurs when the Weber number We exceeds a critical value, We_{cr}. Assuming a drop size in the inertial range of turbulence (so that Kolmogorov's law can be used to define turbulence fluctuations at the drop scale), [69] was able to predict the maximum size of a drop that will not be broken by turbulence in a given flow. Based on available experimental data [35, 36], [69] finally proposed $We_{cr} = 1.18$, even though a general agreement on the value of We_{cr} is still to be found (the value of We_{cr} ranges between 1 and 12, largely depending on the employed fluids and on the flow configuration). Many subsequent theoretical and experimental studies (see [31, 26, 179, 180, 158, 38], among others) have been performed on drops size distribution in engineering-relevant situations (liquid-liquid emulsions in pipelines and stirred tanks), with most of these studies conducted in dilute conditions, so to neglect drops coalescence. However, in any practical situation, drops breakup and coalescence occur simultaneously and cannot be neglected when a complete characterisation of the drop swarm dynamics is required [154]. Unlike the case of drops breakup, drops coalescence has been the subject of relatively fewer studies, most of which focused on the binary collision of two separate drops in still fluid [140, 9, 133]. Although these studies have definitely provided useful insights to understand the fundamental physics of drops collisions and merging, their extension to more complex situations like drops moving inside turbulent pipes or reactors is not straightforward and still requires a leap forward [71, 178]. From the previous literature survey it is apparent that a large proportion of the work on drops breakup and coalescence is based on experimental or theoretical approaches. This is due to the complex nature of drops interactions that has hindered the development of accurate numerical simulations of the phenomenon. Only recently, numerics has become available to analyse complex multiphase flows situations. Accurate numerical simulations can help providing the time evolution of the drops deformation together with the description of the entire flow field inside and outside of the drop. This is extremely important for unsteady turbulent flow conditions, where it is essential to record the coupled drops/turbulence interactions in time and space. In the literature only few available Direct Numerical Simulations [139, 135, 145, 93, 157, 49, 56] of the collective drop dynamics in turbulence are available. The aim of the work here presented is to extend the available literature results on collective drops dynamics in wall-bounded turbulence considering the case of fluids with the same density but different viscosity. In particular, a wide range of drops-to-fluid viscosity ratio $\lambda = \eta_d/\eta_c$ (with η_d the viscosity of drops and η_c the viscosity of the carrier fluid), from $\lambda = 0.01$ to $\lambda = 100$ has been considered.

2.2 Simulation setup

The simulations have been performed considering a system which is composed by a large number of deformable drops, with density ρ_d and dynamic viscosity η_d dispersed in a turbulent channel flow (with the carrier fluid being characterised by density ρ_c and dynamic viscosity η_c). For these simulations two phases which have the same density $\rho = \rho_d = \rho_c$ but different viscosity $\eta_d \neq \eta_c$ have been considered. The fluids are assumed to be newtonian and surfactant is absent and thus $\sigma = \sigma_0$. The time behaviour of the system can be obtained solving Cahn-Hilliard, Navier-Stokes and continuity equations. Under these assumptions the equations proposed in Sec. 1.5 can be simplified as follows:

$$\nabla \cdot \mathbf{u} = 0 \tag{2.1}$$

$$\begin{aligned}\frac{\partial \mathbf{u}}{\partial t} + \mathbf{u} \cdot \nabla \mathbf{u} &= \frac{1}{Re_\tau}\nabla^2 \mathbf{u} + \frac{1}{Re_\tau}\nabla \cdot (\eta(\phi)(\nabla \mathbf{u} + \nabla \mathbf{u}^T)) - \nabla p \\ &+ \frac{3}{\sqrt{8}}\frac{Ch}{We}\nabla \cdot (|\nabla \phi|^2 \mathbf{I} - \nabla \phi \otimes \nabla \phi)\end{aligned} \tag{2.2}$$

$$\frac{\partial \phi}{\partial t} + \mathbf{u} \cdot \nabla \phi = \frac{1}{Pe_\phi}\nabla^2(\phi^3 - \phi - Ch^2 \nabla^2 \phi) \tag{2.3}$$

The main parameters of the system are:

$$Re_\tau = \frac{\rho u_\tau h}{\eta_c} \quad We = \frac{\rho u_\tau^2 h}{\sigma_0} \quad \lambda = \frac{\eta_d}{\eta_c} \quad Ch = \frac{\xi}{h} \quad Pe_\phi = \frac{u_\tau h}{\mathcal{M}_\phi \beta} \tag{2.4}$$

Eqs. 2.3 - 2.2 and 2.1 have been solved in a closed channel geometry, Fig. 1.6, with dimensions $L_x \times L_y \times L_z$ equal to $4\pi h \times 2\pi h \times 2h$. The x, y and z axes point respectively in the streamwise, spanwise and wall normal direction. The flow is driven along the streamwise direction by a constant mean pressure gradient. The initial velocity field is obtained from a Direct Numerical Simulation (DNS) of a single phase turbulent channel flow at $Re_\tau = 150$ and is the same for all the simulations. The initial conditions used for the order parameter ϕ, is made of two arrays of drops. Each array contains 128 drops with a diameter $d = 0.6h$. The phase field is equal $\phi = \pm 1$ inside the drops and in the carrier flow respectively.

Considering the time and length-scale of the flow, and the interface behaviour a grid with a number of nodes $N_x \times N_y \times N_z$ equal to $512 \times 256 \times 257$ has been adopted. The choice of Ch is linked to the grid. From previous simulations (not reported here), it has been observed that using the scaling proposed by [120] the results are independent from Ch. However, to limit the mass leakage [195], Ch must be set to the lowest value possible. Thanks to the accuracy of the spectral method, the accurate resolution of the thin interfacial layer requires 3 nodes across it, consequently $Ch = 0.0185$ and $Pe_\phi = 162.2$ [120] have been set. The effect of We (deformability) and of the drop-to-fluid viscosity ratio λ are analysed through a series of simulations. In particular three values of We and five different λ are considered. An overview of the simulations parameters is given in Tab. 2.1.

$We \backslash\lambda$	0.01	0.10	1.00	10.0	100.
0.75	S1	S2	S3	S4	S5
1.50	S6	S7	S8	S9	S10
3.00	S11	S12	S13	S14	S15

TABLE 2.1 – Summary of the parameters of the simulations. For each We, five different values of the viscosity ratio are used, from $\lambda = 0.01$ to $\lambda = 100$.

In the next section, results obtained from the simulations S1-S15 will be analysed. Results are reported using the wall unit scaling system. Starting from the dimensional analysis presented in Sec. 1.4, the results for a closed channel using the wall units can be obtained as follows:

$$\mathbf{x}^+ = Re_\tau \mathbf{x} \qquad \mathbf{u}^+ = \mathbf{u} \qquad t^+ = Re_\tau t^- \tag{2.5}$$

These changes will affect only the channel dimensions, $\mathbf{u}$ and ϕ will keep the same values. In wall units the channel dimensions $L_x^+ \times L_y^+ \times L_x^+$ are $1885 \times 942 \times 300$ $w.u.$ and the initial drop diameter is $d^+ = 90$ $w.u.$

2.3 Results and discussion

2.3.1 Mean velocity of the multiphase mixture

In a multiphase mixture, the transport of large drops with a given surface tension and with an internal viscosity different from that of the carrier flow may influence the macroscopic behaviour of the system. In the experiments, for all cases reported in Tab. 2.1, a modest drag reduction corresponding to an overall flow rate increase in the range $2 - 4\%$ has been observed. In Fig. 2.1, the wall-normal behaviour of the mean velocity profile of the multiphase mixture (drops and carrier flow) is shown at four different time instants ($t^+ = 0$, $t^+ = 500$, $t^+ = 1000$ and $t^+ = 1500$). Panels (a), (b) and (c) refer to $We = 0.75$, $We = 1.50$ and $We = 3.00$ respectively. For each

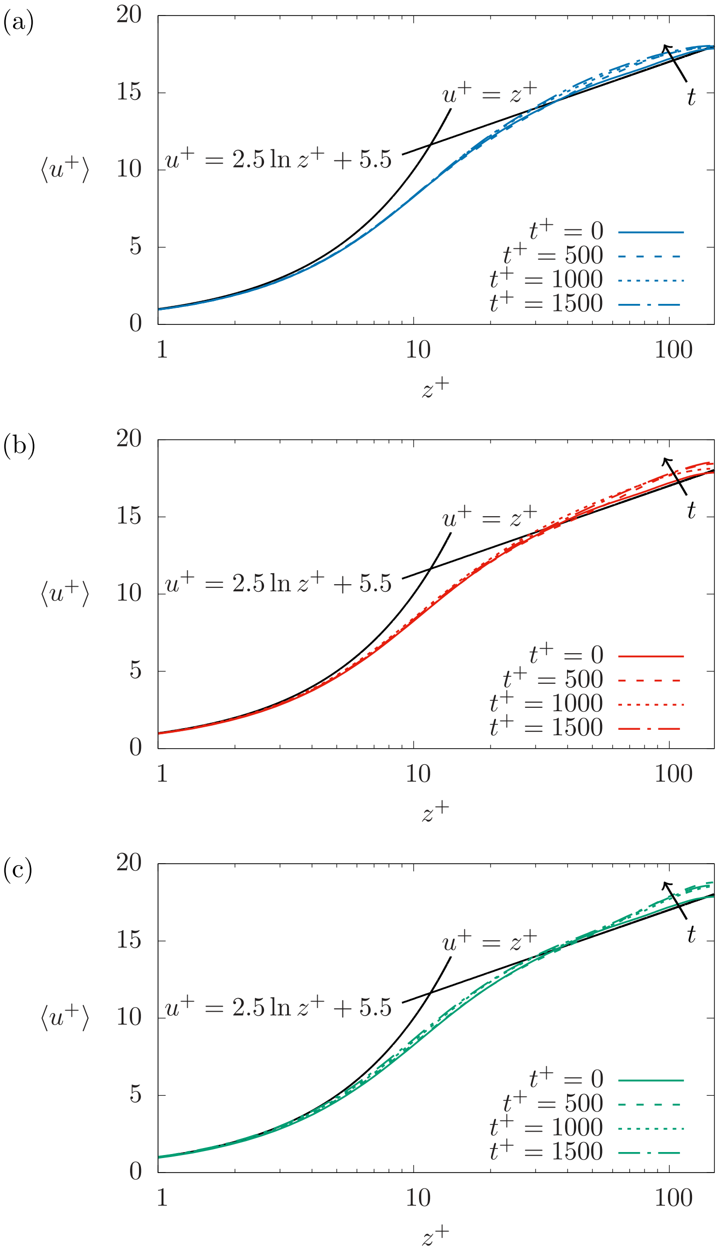

FIGURE 2.1 – Wall-normal behaviour of the mean streamwise velocity of the mixture (drops and carrier flow) at four different time instants. Panel (a) refers to $We = 0.75$, panel (b) to $We = 1.5$ and panel (c) to $We = 3$. For each value of We results are only shown for $\lambda = 1$. The initial velocity profile (solid line, $t^+ = 0$) is obtained from a preliminar simulation of a single phase flow at the same Re_τ. The behaviour of the analytical profile describing the law of the wall is also shown for comparison.

value of We, only results at $\lambda = 1$ has been shown (results at different λ bear only minor quantitative changes that do not add to the discussion). The mean velocity is obtained by averaging the entire flow field (velocities in both phases) along the streamwise and the spanwise directions. All the simulations are initialised with the same velocity field taken from a preliminary simulation of a single phase channel flow at the same Re_τ. As a consequence, at $t^+ = 0$ (solid line), the mean velocity profile for all the simulations collapses onto the classical law of the wall ($u^+ = z^+$ and $u^+ = 2.5 \log z^+ + 5.5$). As soon as drops are injected inside the channel, they interact with the carrier flow increasing the mean velocity in the central part of the channel (overshooting of the mean velocity for $z^+ > 30$). Note that, since the driving pressure gradient is kept constant in all our simulations, an increase in the mean velocity indicates a decrease of the friction factor at the wall (drag reduction). By contrast, only negligible flow modifications close to the wall have been observed (only for $We = 3$ a slight increase of $\langle u^+ \rangle$ is observed, which however does not represent a significant variation). According with previous observations [119] and to this present work, deformable drops tend to stay away from the walls, suggesting that the applied pressure drop is balanced just by the fluid shear stresses at the two walls. In this way, our previous plots on the average velocity of the mixture can have a general significance from the drag reduction viewpoint.

2.3.2 Drops dynamics in turbulence

The dynamics of liquid drops immersed in a turbulent flow field is the result of a complex interaction between destabilising actions due to shear and normal stresses at the drops interface and the stabilising ones due to surface tension (which tends to preserve drop sphericity). Depending on the relative magnitude of destabilising and stabilising actions, drops deform, break and coalesce. When a viscosity difference between the liquid drops and the external fluid ($\lambda \neq 1$) exists, the picture becomes more complex and the internal viscosity of the drops (η_d) plays an active role in controlling the overall drops dynamics [6, 37]. A qualitative representation of such a complex mutual interaction between drops and turbulence is given in Fig. 2.2. It is apparent that drops (coloured in blue) are deformed and advected by the carrier flow (here represented by the flow streamtraces coloured by the local value of the Turbulent Kinetic Energy of the flow, TKE). At the same time, they try to maintain their minimal energy, spherical shape, and they actively modify the flow field. In the following, specifically focus will be put on the role of surface tension (We) and viscosity ratio (λ) on the drops dynamics in a turbulent wall-bounded flow.

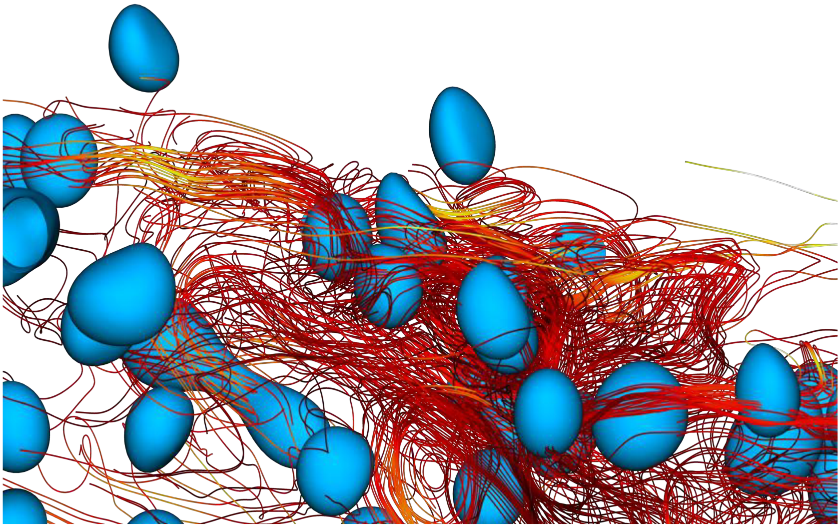

FIGURE 2.2 – Instantaneous realisation of drop-drop and drop-turbulence interaction. Turbulent flow outside the droplets is highlighted by the streamtraces coloured by Turbulent Kinetic Energy (TKE) level (yellow-low and red-high).

Influence of viscosity on the number of drops

When a swarm of liquid drops is injected in a turbulent liquid flow, simultaneous coalescence and breakup events are likely to occur [154, 145] with their balance ultimately determining the number of drops. To visualise the relative importance of these phenomena we therefore compute the time behaviour of the number of drops $N(t)$ for the different cases considered. Results for $N(t)$ are shown in Fig. 2.3 and are normalised by the initial number of drops, N_0. Fig. 2.3(a), Fig. 2.3(b) and Fig. 2.3(c) refer to $We = 0.75$, $We = 1.5$ and $We = 3$ respectively. For each value of We, the drops behaviour for all the viscosity ratios ($\lambda = 0.01$, $\lambda = 0.10$, $\lambda = 1.00$, $\lambda = 10.0$ and $\lambda = 100.$) is considered. For $We = 0.75$, and regardless of the value of λ, $N(t)/N_0$ decreases monotonically in time. In particular, there is an initial stage (up to $t^+ \simeq 1000$) in which $N(t)/N_0$ decreases sharply in time, indicating a strong predominance of coalescence over breakup events with the consequent formation of few large drops. After this initial stage, the number of drops $N(t)/N_0$ achieves and almost constant value, which indeed barely depends on the value of λ; possibly we observe that the final number of drops, represented by the final plateau, is slightly larger for smaller λ. At this We, the large value of the surface tension compared to inertia hinders drops fragmentation (small deformability), even for small values of their internal viscosity. In Fig. 2.3(b) we observe the behaviour for $We = 1.5$: as expected, coalescence events dominate during the initial transient, and a statistically steady state is finally achieved in which the number of drops fluctuates around an average value. The effect of viscosity becomes larger in this case: for drops of small viscosity we observe a final number of drops which is about an order of magnitude bigger compared to the case in which the carrier fluid is less viscous than the drops. In Fig. 2.3(c) we can appreciate the role of drop viscosity at the highest We ($We = 3$). Drops coalescence dominates (i.e. the number of drops $N(t)/N_0$ decreases in time), until a critical drops size is attained, after which the number of drops achieves a plateau that does depend on λ. It is clear that when the drops viscosity is smaller than that of the carrier fluid ($\lambda < 1$), breakup is favoured. By contrast, when the drops viscosity is larger ($\lambda > 1$), coalescence is favoured. Of course, viscosity is not surface tension, and even if the effect of increasing drop viscosity (increasing λ) act as an increase of the surface tension (decrease of We), we must look for the physical mechanism which is ultimately related to turbulence modulation by viscosity [199]. Lower values of the drops viscosity induce larger deformations that eventually cause drops fragmentation (i.e., small drops viscosity is a destabilising factor). By contrast, large values of drops viscosity represent an extra stability factor for drops dynamics, which indeed induces smaller drops deformation and favours the occurrence of coalescence events. Only for $\lambda = 100$ the dynamics appears somehow different, with the initial transient decay extending up to $t^+ \simeq 800$ and an asymptotic condition characterised by a definitely smaller number of drops. However this represents an extreme case for which the stabilising effect due to the large drops viscosity completely balances the small value of the surface tension, resulting in drops having an overall small deformability.

A qualitative representation of the physical mechanism described above is given in Fig. 2.4-2.5 for the two limiting values of We: Fig. 2.4 refers to the case $We = 0.75$, whereas Fig. 2.5 refers to the case $We = 3$. For both $We = 0.75$ and $We = 3$, we show the drops dispersion and deformation in time (at three different time instants $t^+ = 300$, $t^+ = 600$ and $t^+ = 900$) for the two extreme cases $\lambda = 0.01$, Figs. 2.4-2.5(a)-(c), and $\lambda = 100$, Figs. 2.4-2.5(d)-(f). Together with the drops deformation, we also show the contour map of the Turbulent Kinetic Energy TKE, a quantity that may be related to drops deformation and dynamics. Note that $TKE = {u'}^2 + {u''}^2 + {u'}^2$ is shown on the channel centre plane. In these figures, we observe that the number of drops reduces in time (time increases from (a) to (c)), regardless of the value of We and λ. For $We = 0.75$, the drops shape is rather smooth and slightly dependent on λ. However, for $We = 3$ (Fig. 2.5) the situation is remarkably different. The most striking feature observed in this case is the increased drop deformation and the formation of small drops fragments (particularly for $\lambda = 0.01$), as a result of recurring and intensive breakup phenomena [51, 6]. From the underlying contour maps of TKE (shown in grayscale), we clearly identify the strong coupling between drops deformation and turbulence. Drops, which are first deformed

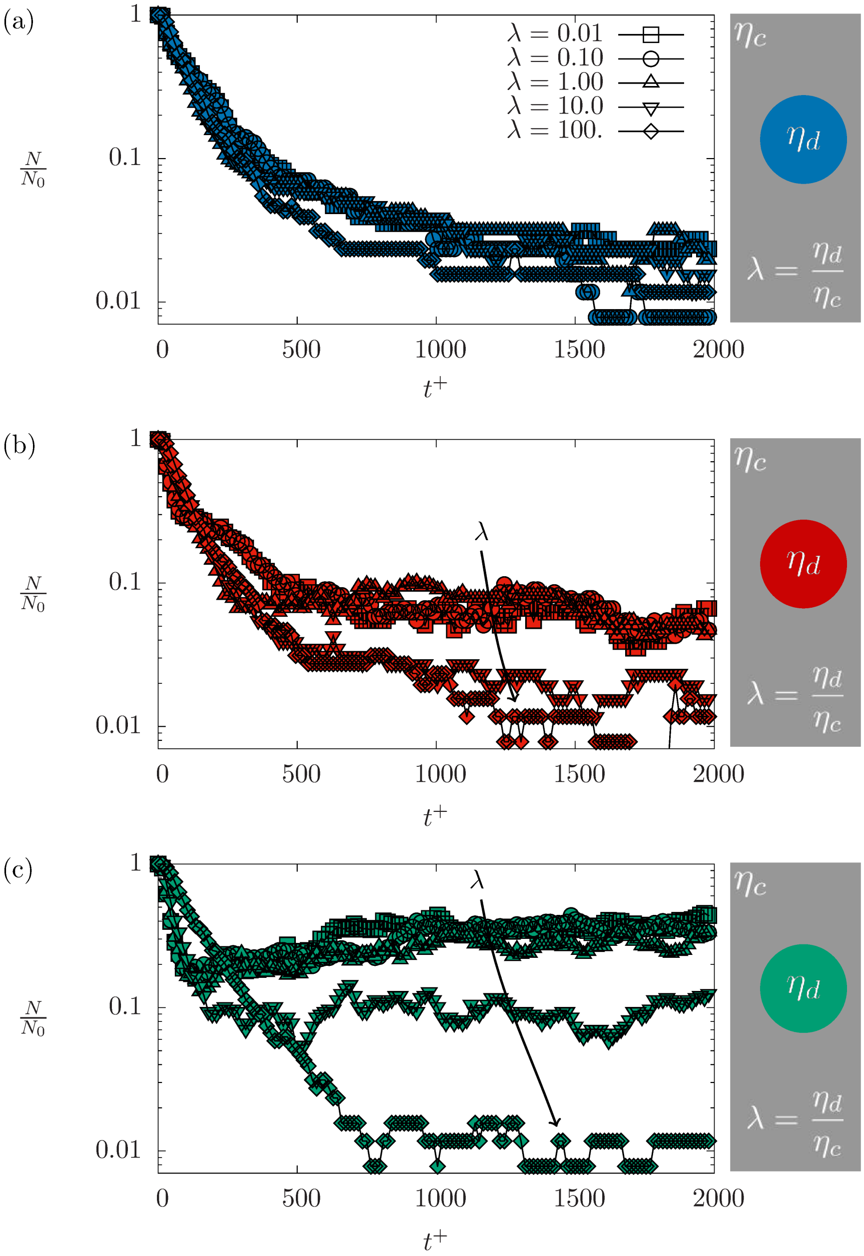

FIGURE 2.3 – Time evolution of the normalised number of drops $N(t)/N_0$ for the three different values of We ($We = 075$, $We = 1.5$ and $We = 3$) considered in the present study. Panel (a) refers to $We = 0.75$, panel (b) to $We = 1.5$ and panel (c) to $We = 3$. In each panel, results for five different values of λ ($\lambda = 0.01$, $\lambda = 0.1$, $\lambda = 1$, $\lambda = 10$ and $\lambda = 100$) are shown. A sketch with the definition of λ and the colour code is given beside each plot (right part of the figure).

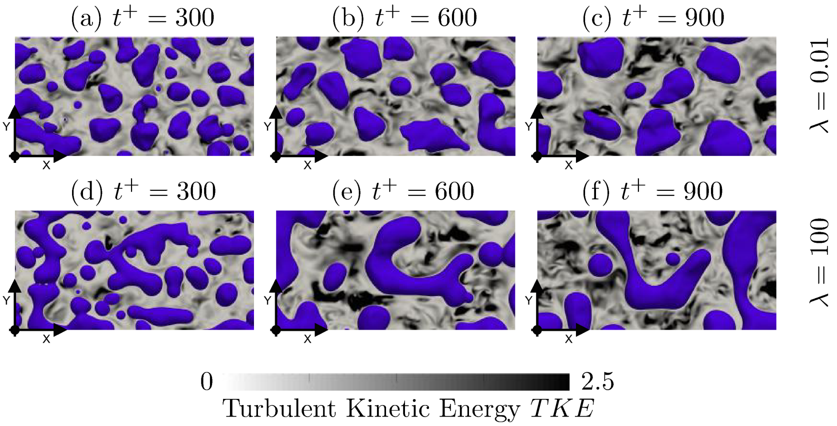

FIGURE 2.4 – Drops evolution for $We = 0.75$ and for the two limiting cases $\lambda = 0.01$, panels (a)-(c) and $\lambda = 100$, panels (d)-(f). Each panel refers to a given time instant ($t^+ = 300$, $t^+ = 600$ and $t^+ = 900$). Contour maps of the Turbulent Kinetic Energy (TKE) computed on a plane passing through the channel centre is also shown.

by turbulence fluctuations, induce a turbulence modulation that is somehow linked to drops viscosity, size and deformation (which in turn depends on We and λ). In general, the larger is λ, the larger is the drops effect on the background turbulence.

Influence of viscosity on the mean curvature

The mechanism by which a reduction of drop viscosity favours drop breakup can be elucidated further by examining the local interface curvature, since it closely characterises drop deformation under the action of turbulence, surface tension and drop-to-fluid viscosity ratio. To compute the surface curvature, we first identify the drop surface as the iso-surface characterised by $\phi = 0$. For each point lying on the drop surface $\phi = 0$, we compute the mean curvature $\mathcal{K}$ as the divergence of the local normal vector $\mathbf{n}$ [143, 162]:

$$\mathbf{n} = -\frac{\nabla\phi}{|\nabla\phi|}, \qquad \mathcal{K} = \nabla \cdot \left(- \frac{\nabla\phi}{|\nabla\phi|} \right). \tag{2.6}$$

The mean curvature $\mathcal{K}$ can either be positive or negative, depending on the drop topology (deformation): positive values of $\mathcal{K}$ identify a local convex interface (e.g., a spheroid) whereas negative values of $\mathcal{K}$ identify a local concave shape (e.g., a hyperboloid). Small values of $\mathcal{K}$ indicate a flat interface (or, alternatively, the presence of a saddle point), while large values of $\mathcal{K}$ (both positive or negative) characterise a surface with bumps (positive $\mathcal{K}$) or dimples (negative $\mathcal{K}$), likely indicating possible drops fragmentation. A qualitative picture showing the behaviour of the local surface curvature is given in Fig. 2.6 for the simulation at $We = 3$ and for the two extreme

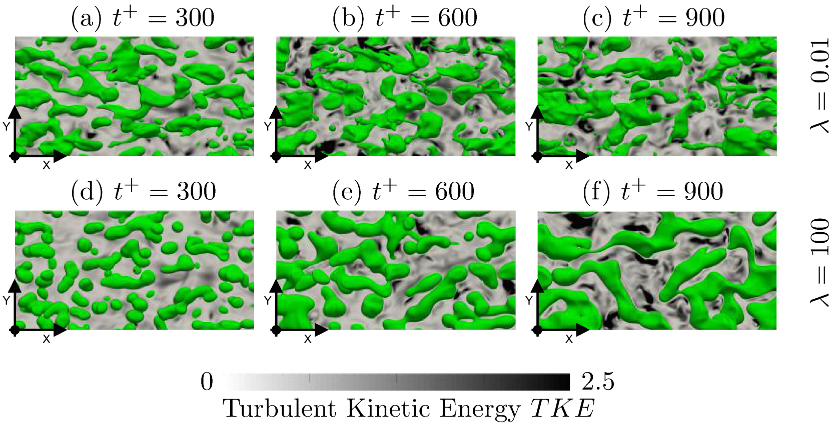

FIGURE 2.5 – Drops evolution for $We = 3$ and for the two limiting cases $\lambda = 0.01$, panels (a)-(c) and $\lambda = 100$, panels (d)-(f). Each panel refers to a given time instant ($t^+ = 300$, $t^+ = 600$ and $t^+ = 900$). Contour maps of the Turbulent Kinetic Energy (TKE) computed on a plane passing through the channel centre is also shown.

cases $\lambda = 0.01$ and $\lambda = 100$. Red regions are bumps or small satellite drops, whereas blue regions are dimples and scars at the drops interface. Green regions refer instead to relatively flat interfaces (or saddle points). Unlike the case of small drops viscosity ($\lambda = 0.01$, Fig. 2.6(a)) where drops fragmentation and increased surface roughness are clearly seen, for large drops viscosity ($\lambda = 100$, Fig. 2.6(b)), drops are characterised by a smooth surface with small curvature values. This indicates that large drops viscosity increases drops stability against breakup through the increase of drops viscous dissipation [7, 41].

To give these observations a more quantitative slant, in Fig. 2.7 we compute the PDF of the mean curvature $\mathcal{K}$ for all simulated cases. Fig. 2.7(a) refers to the case $We = 0.75$, whereas Fig. 2.7(b) and Fig. 2.7(c) refer to the case $We = 1.5$ and $We = 3$, respectively. For each value of We, all λ are shown. We first consider the case $We = 0.75$ (Fig 2.7(a)). We clearly observe that the PDF is asymmetric, with the most probable value occurring for $\mathcal{K} \simeq 0.5$ and with positive curvatures being larger and more probable than negative curvatures . This reflects the observation that at small We the drops shape is not significantly deformed and departs only slightly from its equilibrium (spherical) shape. The effect of changing drops viscosity (λ) is negligible in this case, with all the PDF curves collapsing nicely onto each other. Few differences are observed only for $\lambda = 100$, a case for which the increased drops viscosity hinders drops deformation and reduces the occurrence of large curvature events. Overall, we can safely conclude that, for $We = 0.75$, effects of drops viscosity on the local curvature remain generally small. The situation changes sharply when larger

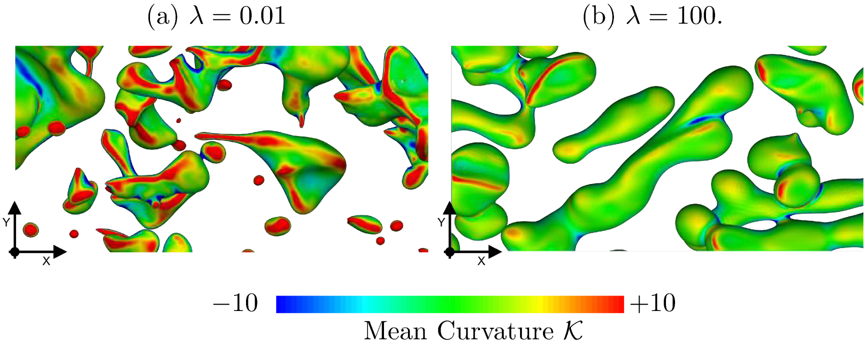

FIGURE 2.6 – Mean curvature $\mathcal{K}$ of the drops surface for $We = 3$ and for the two limiting values of λ. Panel (a) refers to $\lambda = 0.01$, whereas panel (b) refers to $\lambda = 100$.

values of We are considered. In particular, we will refer to $We = 3$, since all the effects we wish to discuss are emphasised in this case (results for $We = 1.5$ are qualitatively similar, albeit less pronounced). Considering the case $We = 3$ (Fig. 2.7(c)), we notice that for small values of the drops viscosity ($\lambda < 1$) there is a remarkable increase of the probability of having large curvature events ($|\mathcal{K}^+| > 5$). This is linked to the physical intuition that for large We and small drops viscosity (small λ) the surface tension is simply too weak to balance the combined effects of external turbulence and small internal viscosity, which ultimately cause a sharp increase of the drops breakup frequency. Interestingly, for large drops viscosity ($\lambda = 10$ and $\lambda = 100$) the shape of the PDF becomes rather similar to that observed for $We = 0.75$: this indicates that the increased drops viscosity balances the small value of surface tension ($We = 3$) and prevents drops breakup while promoting drops coalescence. These findings have profound effects on the parametrisation and modelling of drops breakup and coalesce in turbulence, which is a very important field of research [158, 31, 38]. It is well established [69] that a critical Weber number We_{cr} can be defined such that for $We > We_{cr}$ breakup events dominate, whereas for $We < We_{cr}$ coalesce events dominate. Now, it turned out that for small drops viscosity ($\lambda \leq 1$), We_{cr} does not significantly depend on λ (negligible viscous dissipation) and $We_{cr} \simeq 1.18$ [69]. For small drops viscosity ($\lambda < 1$), we can still retain $We_{cr} \simeq 1.18$, since viscous dissipation inside the drop becomes negligible. By contrast, We_{cr} is sensitive to an increase of the drops viscosity ($\lambda > 1$). In this case, the large drops viscosity increases drops dissipation and drops stability, a circumstance that ultimately leads to a monotonic increase of We_{cr} with λ [69, 37, 72, 159, 41].

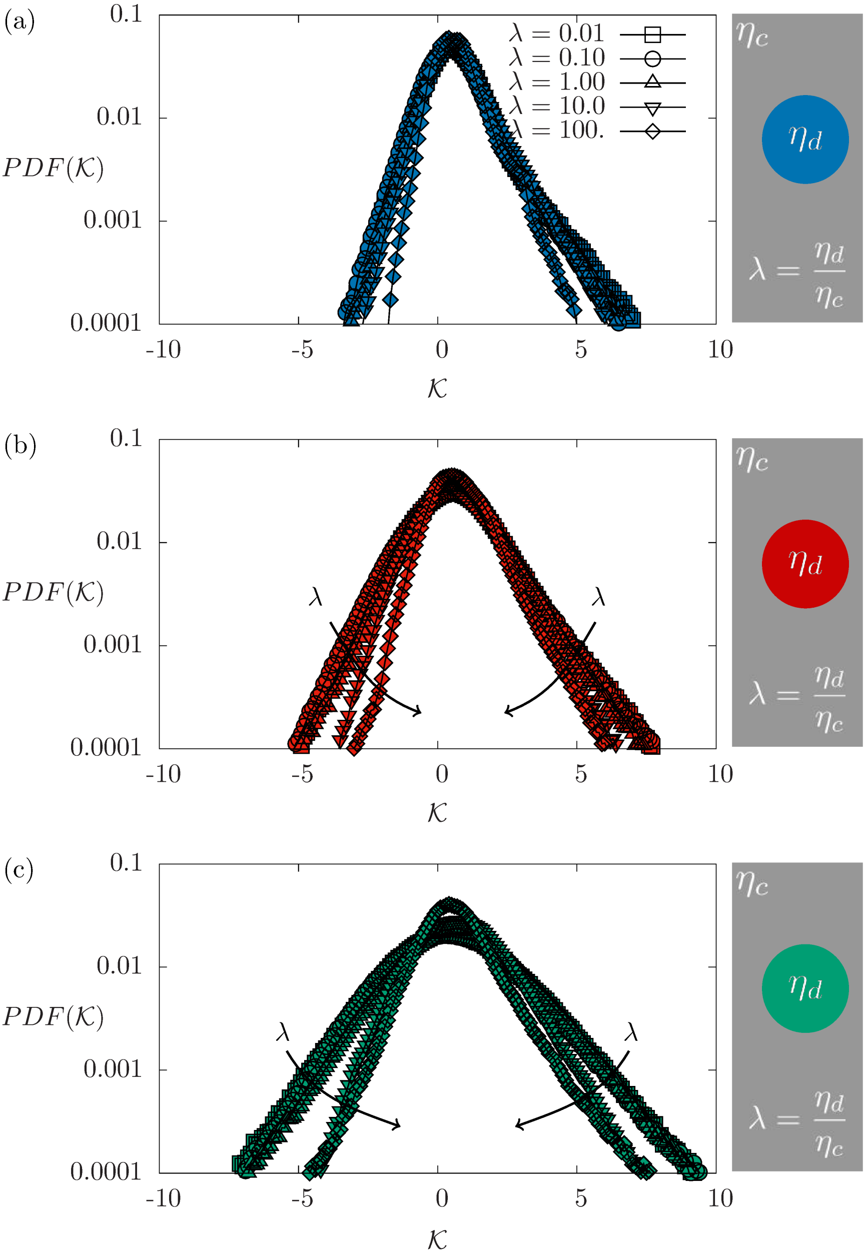

FIGURE 2.7 – Probability density function (PDF) of the Mean Curvature $\mathcal{K}$ for the three different values of We ($We = 075$, $We = 1.5$ and $We = 3$) considered in the present study. Panel (a) refers to $We = 0.75$, panel (b) to $We = 1.5$ and panel (c) to $We = 3$. In each panel, results for five different values of λ ($\lambda = 0.01$, $\lambda = 0.1$, $\lambda = 1$, $\lambda = 10$ and $\lambda = 100$) are shown. A sketch with the definition of λ and the colour code is given beside each plot (right part of the figure).

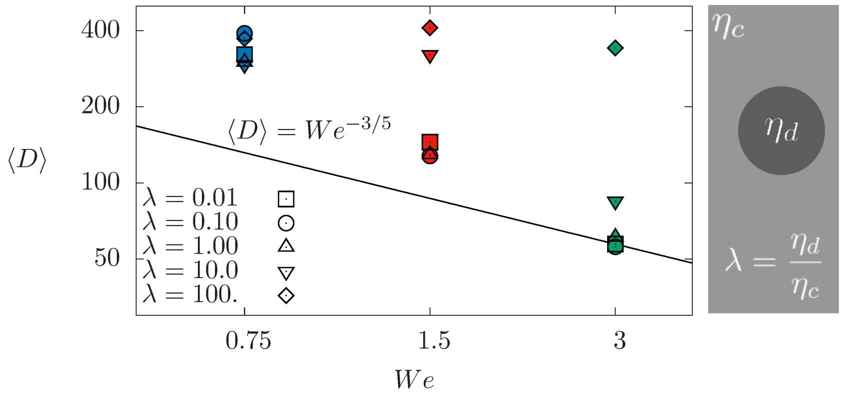

FIGURE 2.8 – Mean drop diameter $\langle D \rangle$ obtained for each simulated case (symbols) as a function of We. The theoretical prediction $\langle D \rangle \propto We^{-3/5}$ given by [69] is also shown for comparison (solid line). A sketch with the definition of λ is given beside the main panel.

Influence of viscosity on critical drops diameter

As already discussed above, quantifying and controlling drops size distribution in a liquid-liquid mixture is extremely important for the design of efficient emulsification or atomisation processes in turbulence [69, 158, 31, 38, 7, 26, 179, 180]. A sound estimate for the diameter of the largest drop (D_{max}) that can be transported without fragmentation in a turbulent environment was given by [69] for very dilute mixtures (so to neglect possible side effects of coalescence) and assuming that the major contribution to drop breakup is due to velocity fluctuations (dynamic pressure) having wavelength of the order of the drop diameter. For homogeneous isotropic turbulence,

$$D_{max} = 0.725 \left(\frac{\rho}{\sigma} \right)^{-3/5} \varepsilon^{-2/5}. \tag{2.7}$$

However, for the general case of liquid-liquid mixtures at larger volume fractions, coalescence and breakup events occur simultaneously, a situation which must be taken into consideration to obtain accurate estimates of the collective drops dynamics. In such a complex situation, in which coalescence and breakup may balance each other, a more precise indicator for the drop size is the average drop diameter [135]. From the above considerations, Eq. (2.7) written for the average drop diameter and expressed in wall units (with the superscript '+' being dropped for ease of notation), becomes:

$$\langle D \rangle = 0.725 \left(\frac{We}{Re_\tau} \right)^{-3/5} \varepsilon^{-2/5}, \tag{2.8}$$

where the dissipation ϵ, which is in general a function of the wall distance, is here evaluated in the carrier phase at the centre of the channel (where drops preferentially stay [145, 146]). The theoretical behaviour of $\langle D \rangle$ described by Eq. (2.8) is shown in Fig. 2.8 as a function of We for all the simulated cases. We immediately notice that our results support the validity of Hinze's models, but only for large We and small drops viscosity (when breakups essentially control the dynamics). This is reasonable since the model is developed assuming negligible coalescence effects (large We) and negligible viscous dissipation (small λ). By contrast, a more complex dependency of the results on We and λ is observed for small We and large λ. Further experimental and numerical campaigns are therefore required to obtain a reliable value of this prefactor for different flow configurations (at present, indicative values of the prefactor can be found for liquid-liquid emulsions in stirred tank reactors [7, 41]).

2.4 Conclusions

Drops dynamics in turbulence is a complex phenomenon characterised by the competition between the destabilising action of turbulence (which deforms and eventually brings the drops to breakup) and the stabilising action of surface tension (which tends to preserve the drops integrity). When drops viscosity is different from that of the carrier fluid, the picture becomes even more complex since drops viscous dissipation can become important. Here, the focus has been put on the complex interplay between surface tension (We) and drop-to-fluid viscosity ratio (λ), which determines breakage and coalescence of large deformable drops in turbulence. Specifically, the drops dynamics has been studied using Direct Numerical Simulations (DNS) of turbulence coupled with a Phase Field Model (PFM). We considered three different We ($We = 0.75$, $We = 1.5$ and $We = 3$), and five different values of λ ($\lambda = 0.01$, $\lambda = 0.10$, $\lambda = 1.00$, $\lambda = 10.0$ and $\lambda = 100$). In all the cases analysed in the present study, a small increase of the flow-rate of the mixture, in the range $2-4\%$ has been observed. The effect of drops, on the average velocity of the mixture (drops and carrier flow) has been analysed, regardless of the value of the physical parameters (λ and We), the average velocity of the mixture increase in time. This is an indication that turbulent kinetic energy is absorbed by drops (i.e. kinetic energy is converted into drops deformation) and induces an overall drag reduction of the flow. Then, the focus has been put on drops dynamics. For the base case $\lambda = 1$, we observed that drops dynamics is dominated by coalescence for small We ($We < 1$), with breakup events entering the picture only for increasing We ($We > 1$). Interestingly, we found that this situation is selectively modified for $\lambda \neq 1$. For small We ($We < 1$), drops deformability remains small and the viscosity ratio λ does not influence the coalescence/breakup rate. For larger We ($We > 1$), drops deformability is increased and the viscosity ratio λ can significantly alter the coalescence and breakup dynamics. In particular, increasing drops viscosity reduces strongly the breakup rate (and increase the coalescence rate), very much like a reduction of We does. We linked this result to the increased value of the drops viscous dissipation which ultimately increases drops stability. Viscosity gradients across the interface of the drops act as modulators of the local shear stresses and can amplify or damp the inertial turbulence perturbations. Finally, the results have been compared against the theory developed by Hinze [69] to predict the size of a swarm of droplets in turbulence. Our data confirm the predictions [69] at small λ, (drop viscosity smaller than fluid viscosity) which is the case analysed by Hinze. Further analyses are required to examine the phenomena at larger values of drops to fluid viscosity ratios.

3

Coalescence of clean and surfactant-laden droplets in shear flow

Reproduced in part from:

G. Soligo, A. Roccon, and A. Soldati, Phase Field Method to predict coalescence of clean and surfactant-laden droplets, J. Comput. Phys., in preparation.

3.1 Problem definition

The coalescence of droplets plays a central role in various disciplines of nature and industrial interest, such as the formation of raindrops [66], spray combustion [78, 84] and emulsification processes [48].
The coalescence's efficiency depends on a large number of parameters as the density and viscosity ratios between the two phases, the surface tension, the presence of surface active agents (surfactants) and the geometrical configuration. The coalescence process can be divided in three main stages: (*i*) approach, the droplets get close and starts to interact and deform, (*ii*) Draining, the thin liquid film present in the gap between the two droplets starts to drain, (*iii*) breakage of the liquid film, when the film's thickness reaches a critical values, attractive intermolecular forces can break it and the two droplets merge [121]. The surfactants, compounds made of molecules with an hydrophilic head and a hydrophobic tail [126], are often used to prevent the coalescence [161, 75]. These molecules, decreasing the surface tension, introduce in the system non-uniform capillary and tangential stresses which can hinder the draining process [42, 34, 152]. As a consequence, the surfactants can drastically change the behaviour of

the multiphase flow [165, 164, 109].

The efficient and accurate computational modelling of interfacial flows with surfactant is a challenging task. From a numerical point of view, a coupled system of equations must be solved on a moving and deforming interface which may undergo topological changes such as breakup and coalescence.

The nmerical methods used to simulate interfacial flows with surfactant can be roughly divided in two categories: interface tracking and interface capturing methods. Interface tracking methods use a separate grid or mesh to track the interface. The most popular are the Front-Tracking (FT) method [198, 45, 118, 125, 14], the Boundary Integral Method (BIM) [161, 40, 114] and the Immersed Boundary Method (IBM) [99, 100]. Initially developed for insoluble surfactants, extensions to soluble surfactants have been proposed by [198, 124]. In general, these methods offer a good accuracy but the description of topological changes requires complex algoritms, especially in three dimensions. Interface-capturing methods use an indicator function to implicitly represent the interface using an Eulerian grid. This greatly simplifies the discretisation and the handling of topological changes. The commonly used interface capturing methods are the Volume-Of-Fluid (VOF) [70, 148] and the Level-Set method (LS) [128, 149]. For the VOF method, possible approaches for insoluble surfactants have been proposed by [50, 141, 80, 16] and then further extended to soluble surfactants and 3D flows by [4]. Considering the LS method, a possible approach has been proposed by [190] and then further developed to consider flow and contact line dynamics [186, 189, 188, 57, 144]. Recently, alternative approaches, which combine interface capturing and interface tracking methods or which are based on different frameworks, have been developed. In the work of [27] LS and FT are used together whereas [191, 175, 192] proposed techniques based on the so-called Arbitrary Lagrangian-Eulerian (ALE) method. Considering other frameworks, a Smooth-Particle Hydrodynamics (SPH) method has been proposed by [1] whereas for the colour-gradient Lattice Boltzmann (LB) method [67] an approach for insoluble surfactants has been proposed by [54].

Here, a Phase Field Method (PFM) [5, 79] for the simulation of interfacial flows with soluble surfactants is considered. The method, based on an interface capturing technique, implicitly represents the interface and the surfactant concentration using two order parameters, the phase field ϕ and the surfactant concentration ψ. The transport equations for the two order parameters are derived from a single Ginzburg-Landau free energy functional [104, 94, 171]. The two order parameters and their relative transport equations are defined in all the domain and thus simpler numerical methods can be used. Moreover, absorption/desorption of surfactants and topological changes are implicitly handled. The effect of surfactant on surface tension is included using an Equations Of State (EOS). Here, the phase field method is coupled with Direct Numerical Simulation (DNS) of the Navier-Stokes equations.

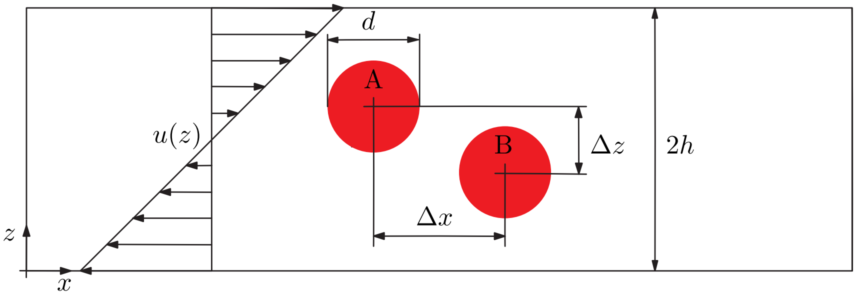

FIGURE 3.1 – sketch of the configuration used to analyse the effects of the surfactant on the droplet-droplet interaction. The droplets, with diameter $d = 0.7h$, are separated by a distance $\Delta x = h$ and $\Delta z = 0.5h$. The walls, $z = \pm h$, move at constant velocity in opposite directions. A linear velocity profile $u(z)$ is imposed.

3.2 Simulation setup

The capabilities of the proposed method has been tested considering the interaction between two droplets posed in shear flow, Fig. 3.1. This problem has been previously investigated with experiments by [65, 181] and using numerical simulations by [115, 15, 43, 152]. When surfactant is not considered, the outcome of the collision is determined by the capillary number Ca, defined as:

$$Ca = \frac{u_\tau \eta_c}{\sigma_0} \frac{d}{2h} \tag{3.1}$$

which is the ratio between viscous and surface tension forces. Considering large Ca, the droplets' interfaces during the interaction flatten hindering the draining of the thin liquid film. The decreased draining speed inhibit the coalescence and the two droplets slide away. By opposite, as the capillary number is reduced, the lower deformability leads to a complete draining of the fluid film. Thus, the interfaces come close enough that intermolecular forces dominate and the droplets merge.

The surfactant, introducing tangential stresses and increasing the interface deformability, can drastically changing the outcome of the interaction [40, 130]. We start considering the interaction between two clean droplets, $Ca = 0.10$. Then a wide range of bulk surfactant concentrations ψ_b and elasticity number β_s have been considered. The first parameter, ψ_b defines the amount of surfactant present in the system while the elasticity number β_s determines the influence of the surfactant on the surface tension.

The system is composed by a continuous external phase and a dispersed phase (droplets). The density and the viscosity of the two phases are assumed to be matched, $\rho = \rho_c = \rho_d$ and $\eta = \eta_c = \eta_d$. The spatial and temporal evolution of the system can be obtained solving continuity, Navier-

Stokes, Cahn-Hilliard and surfactant equations:

$$\nabla \cdot \mathbf{u} = 0 \tag{3.2}$$

$$\frac{\partial \mathbf{u}}{\partial t} + \mathbf{u} \cdot \nabla \mathbf{u} = \frac{1}{Re_\tau} \nabla^2 \mathbf{u} - \nabla p + \frac{3}{\sqrt{8}} \frac{Ch}{We} \nabla \cdot (f(\psi)(|\nabla \phi|^2 \mathbf{I} - \nabla \phi \otimes \nabla \phi)) \tag{3.3}$$

$$\frac{\partial \phi}{\partial t} + \mathbf{u} \cdot \nabla \phi = \frac{1}{Pe_\phi} \nabla^2 (\phi^3 - \phi - Ch^2 \nabla^2 \phi) \tag{3.4}$$

$$\frac{\partial \psi}{\partial t} + \mathbf{u} \cdot \nabla \psi = \frac{Pi}{Pe_\psi} \nabla^2 \psi + \frac{1}{Pe_\psi} \nabla \cdot (\psi(1 - \psi) \nabla C_{\psi\phi}) \tag{3.5}$$

Since a surfactant is considered, in the Navier-Stokes equation, the general formulation of the surface tension term has been used. The formulation used implicitly accounts for the non-uniform capillary and tangential stresses present at the interface. All the equations are already written in the dimensionless form as shown in Sec. 1.4. The clean system can be analysed considering $\psi = 0$ throughout all the domain. A linear approximation of the Langmuir EOS [108] has been used:

$$f(\psi) = 1 - \beta_s \psi \tag{3.6}$$

This approximation is valid in the limit of low surfactant concentrations. The dimensionless parameters that appear in the Navier-Stokes and Cahn-Hilliard equations are defined as follows:

$$Re_\tau = \frac{\rho u_\tau h}{\eta} \quad We = \frac{\rho u_\tau^2 h}{\sigma_0} \quad Ch = \frac{\xi}{h} \quad Pe_\phi = \frac{u_\tau h}{\mathcal{M} \beta} \tag{3.7}$$

For the surfactant, the parameters are:

$$Pe_\psi = \frac{\alpha u_\tau h}{\beta^2 \mathcal{M}_\psi} \quad Pi = \frac{\lambda_\psi}{\beta^2} \quad E_x = \frac{\beta}{s_\psi} \tag{3.8}$$

In addition the bulk surfactant concentration ψ_b and the elasticity number β_s must be also set. Equations 3.2 - 3.3 - 3.4 and 3.5 are solved in a two dimensional channel geometry, Fig. 1.9, with dimensions $L_x \times L_z$ equal to $2\pi h \times 2h$. The two walls move along the x direction at constant velocity but in opposite directions $u_x(\pm h) = \pm 1$. A no-slip boundary condition is used for the velocity at the walls, $w(\pm h) = 0$. For the order parameters, no-flux boundary conditions have been enforced on ϕ and ψ and on the 2^{nd} derivative of ϕ:

$$\frac{\partial \phi}{\partial z}(\pm h) = 0 \qquad \frac{\partial^3 \phi}{\partial z^3}(\pm h) = 0 \qquad \frac{\partial \psi}{\partial z}(\pm h) = 0 \tag{3.9}$$

These boundary conditions lead to a no-flux boundary condition even for the two chemical potentials μ_ϕ and μ_ψ; as a consequence the integral of the two order parameters is conserved over time:

$$\frac{\partial}{\partial t}\int_\Omega \phi d\Omega = 0 \qquad \frac{\partial}{\partial t}\int_\Omega \psi d\Omega = 0 \tag{3.10}$$

where Ω is the domain considered. Along the x direction periodic boundary conditions for all the variables have been used. The initial flow field is a linear velocity profile for the streamwise velocity, $u(z) = z/h$, the wall-normal velocity w has been set to zero. A laminar shear flow is considered, the shear Reynolds number is $Re_\tau = 0.5$. The initial condition used for the order parameter ϕ consists of of two spherical droplets of diameter $d = 0.7h$. The order parameter ϕ is set to $\phi = +1$ inside the droplets and to $\phi = -1$ in the continuous phase. The centres of the two droplets are separated by a distance $\Delta x = h$ and $\Delta z = h/2$ and are located at $x_c = L_x/2 \pm \Delta x/2$ and $z_c = \mp \Delta z/2$. Weber number has been set to $We = 0.15$, which leads to a capillary number $Ca = 0.10$. Considering the time and length-scale of flow, interface and surfactant, the domain has been discretised using a number of collocation points $N_x \times N_z$ equal to 512×513. Once the grid is set, Ch and Pe can be obtained. For the accurate solution of the interface and the surfactant dynamics, at least 4 nodes across the interface are needed. Thus a Cahn number $Ch = 0.02$ has been chosen. Following the scaling proposed by [120], $Pe_\phi = 150$ has been set.

For the surfactant, $Pe_\psi = 100$ has been used: with this value convective phenomena will dominate over the diffusion phenomena. This case is quite common in real applications where the surfactant diffusion along the interface is slow if compared to the flow convection. The parameter Pi has been set to $Pi = 1.35$, the parameter E_x, which controls the bulk solubility, has been set to $E_x = 0.117$, same values used by [52]. For these simulations, Pi and E_x have been kept fixed and the amount of surfactant and its effect on the surface tension have been tuned changing the bulk surfactant concentration ψ_b and the elasticity number β_s.

A total of 20 simulations has been performed. Five bulk surfactant concentrations: $\psi_b = 0.1 \times 10^{-2} - 0.25 \times 10^{-2} - 0.5 \times 10^{-2} - 0.75 \times 10^{-2} - 1. \times 10^{-2}$ and four elasticity number $\beta_s = 0.25 - 0.5 - 0.75 - 1$ have been considered. An additional case, $\psi_b = 0$ and $\beta_s = 0$, has been considered; this case identify the clean configuration. For the order parameter ψ, the equilibrium profile has been used as initial condition, in the bulk $\psi = \psi_b$ and $\psi = \psi(\phi)$ across the interface. An overview of the parameters used for the simulations is reported in Tab. 3.1.

		Bulk surfactant concentration $\psi_b \times 10^2$				
		0.10	0.25	0.50	0.75	1.00
β_s	0.25	A1	B1	C1	D1	E1
	0.50	A2	B2	C2	D2	E2
	0.75	A3	B3	C3	D3	E3
	1.00	A4	B4	C4	D4	E4

Table 3.1 – Parameters used for the simulations of the droplet-droplet interaction in shear flow. For each value of the bulk surfactant concentration, ψ_b, four different values of the elasticity number β_s have been considered.

3.3 Results and discussion

The results obtained from the interaction between two surfactant-laden droplets will be here presented and discusses. First, we consider the outcome of the interaction for different values of the surfactant bulk concentrations and elasticity numbers. Then, the role played by the increased deformability and by tangential stresses at the interface on the droplet-droplet will be considered.

3.3.1 Outcome of the droplet-droplet interaction

We start considering the outcome of the droplet-droplet interaction. After the release, the shear flow deforms and drives the droplets towards collision. The droplet A has a positive velocity (and moves from left to right), while droplet B has a negative mean velocity (and moves from right to left). After the initial approaching stage, the droplets can interact, as the droplets get closer the thin liquid film between them starts to drain. If the liquid film reaches a critical thickness, the attractive intermolecular forces can break it and the two droplets coalesce. The presence of a surfactant can drastically affects the interaction, indeed the increased deformability and the tangential stresses at the interface can hamper the draining of the thin liquid film and alter the final interaction's outcome [40]. The results for different combinations of the parameters ψ_b and β_s are reported in Fig. 3.2. For each combination of the parameters, a filled dot identifies a coalescence event while an empty dot identifies a non-coalescence event. Considering the clean case, $\psi_b = 0$ and $\beta_s = 0$ (blue-dot), the two droplets coalesce; the absence of tangential stresses at the interface and the low deformability allow the draining of the thin liquid film and the subsequent merging. When surfactant is added, for the lowest concentration, A-series ($\psi_b = 0.1 \times 10^{-2}$), and for each β_s, surfactant effects are small and the two droplets coalesce. Increasing the bulk surfactant concentration, B-series ($\psi_b = 0.25 \times 10^{-2}$), the surfactant influences the behaviour, and for $\beta_s = 0.75$ and $\beta_s = 1.00$ the droplets do not coalesce. Further increasing the bulk surfactant concentration, C-D-E series, surfactant changes the outcome of the interaction, and

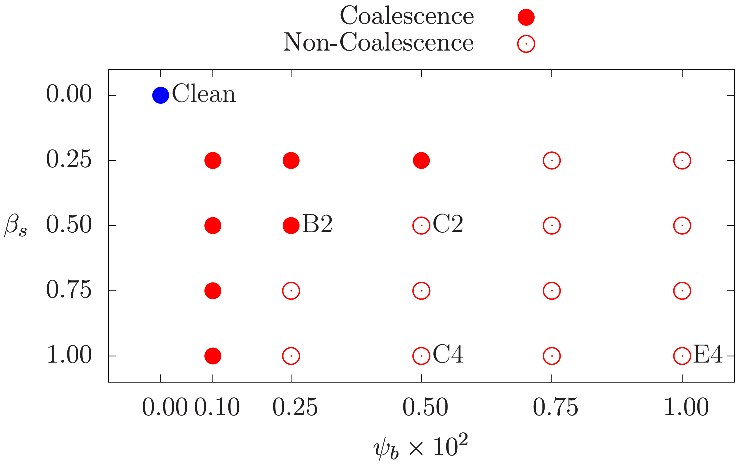

FIGURE 3.2 – Outcome of the interaction. A filled dot identifies a coalescence event while an empty dot identifies a non-coalescence event. The blue dot, located in the point β_s and $\psi_b = 0$ identifies the outcome of the interaction of two clean droplets. It can be observed that either an increase of the surfactant bulk concentration ψ_b, either an increase of the elasticity number, β_s, inhibit coalescence.

regardless of the case C1, droplets slide away without coalescing. Overall, an increase of the bulk surfactant concentration ψ_b, together with an increase of the elasticity number β_s prevent the coalescence.

To give a better insight of the droplet-droplet interaction, the time evolutions of the system for two cases (B2 and C4) are reported in Figs. 3.3-3.4. In both the figures, the column on the left, panels (a)-(c)-(e)-(g), refers to simulation B2, $\beta_s = 0.5$ and $\psi_b = 0.25 \times 10^{-2}$, while the column on the right, panels (b)-(d)-(f)-(h), refers to simulation C4, $\beta_s = 1.0$ and $\psi_b = 0.5 \times 10^{-2}$. Time increases from the top to the bottom. In these two figures only a central section of the channel is reported, between $L_x = \pi/2$ and $L_x = 3\pi/2$, while the whole z axis is shown.

Starting from $t = 1.0$, the droplets move and get closer, Fig. 3.3(a)-(b). The droplets deform and the surfactant migrate towards the droplets' tips, Fig. 3.4(a)-(b). Later, at $t = 2.0$, the droplets are separated by a thin liquid film. The draining process produce two regions with high vorticity $\omega_x = \partial w/\partial y - \partial v/\partial z$, Fig. 3.3(c)-(d). In this stage, the droplets are more deformed, Fig. 3.3(c)-(d), and more surfactant gathers at the tips, Fig. 3.4(c)-(d). Then, Fig. 3.3(e)-(f), the difference between the two cases in more evident. For the case B2, the draining is faster, the fluctuations of the vorticity ω_x in the gap are lager and the gap between the two droplets is smaller. At $t = 4.0$, for the case B2, the draining process is over and the two droplets merge, Fig. 3.3(g). The surface tension forces reshape the droplet and the surfactant is redistributed, Fig. 3.4(g). By opposite, for the case C4, the surfactant, increasing the deformability and producing tangential stresses at the interface, Fig. 3.4(h), slows down the draining of the thin liquid film and the two droplets do not coalesce.

3.3.2 Deformation during the droplet-droplet interaction

To analyse the effect of the surfactant on the deformability, we compute the deformation parameter D of the two droplets during the interaction. The time evolution of D during the interaction for different bulk surfactant concentrations ψ_b and elasticity numbers β_s are reported in Fig. 3.5. Since the two droplets evolve in time in the same way, only the deformation parameter of the droplet A has been plotted.

The five mini-panels (A-B-C-D-E) are used to show the generic configuration of the system at the different times. We start by considering the results reported In Fig. 3.5(a): we compare $D(t)$ for different simulations, starting from the clean case (blue line) up to the case with the highest amount of surfactant, E4, (dash-dotted red line). The droplets, initially spherical ($D = 0$), start to deform and move according to the shear flow. After $t = 1.5$, the droplets are close enough and strongly interact, the deformation parameter reaches a maximum (mini panel A). Then, the presence of the other droplet leads to a reduction of the deformation parameter D that reaches a minimum for, $t \simeq 3$ (mini panel C). The minimum value of D is smaller for the clean case (blue line) and it is larger when ψ_b and/or β_s are increased (from the case B2 to the case E4). This stage of the interaction is crucial for determining the outcome, indeed higher deformations slow down the draining of the thin liquid film. After point C, for the clean and the B2 cases, the droplets coalesce (blue/red dots) and D is not anymore computed. Considering the cases C2-C4-E4, after $t \simeq 3$, the two droplets separate; the deformation parameter D increases and reaches a new maximum at $t \simeq 4$. After $t \simeq 4$, D decreases and reaches an asymptotic value, $t > 5$ (not reported here).

In Fig. 3.5(b), The results of the case E4 are compared with the ones obtained from a simulation which consider two droplets with an equivalent deformability but without surfactant. The equivalent Ca has been computed considering the problem of a single droplet in shear flow, obtaining $Ca = 0.12$. The clean case with $Ca = 0.10$ is also reported as reference. We can see that for $Ca = 0.12$, despite the clean interface, the two droplets do not coalesce. For the cases $Ca = 0.12$ and E4, the time behaviour of D is similar and the only difference is a slight delay of the case E4, probably due at the tangential stresses at the interface. Comparing the cases $Ca = 0.12$ and E4 with the case $Ca = 0.10$, it can be observed how the minimum value of D is smaller for the case $Ca = 0.10$.

Overall, from Fig. 3.5(a)-(b), it is clear how the deformability plays a crucial role in determining the outcome of the interaction. The surfactant, decreasing the surface tension, increases the deformation of the droplets and hampers the draining of the thin liquid film. The coalescence is favoured

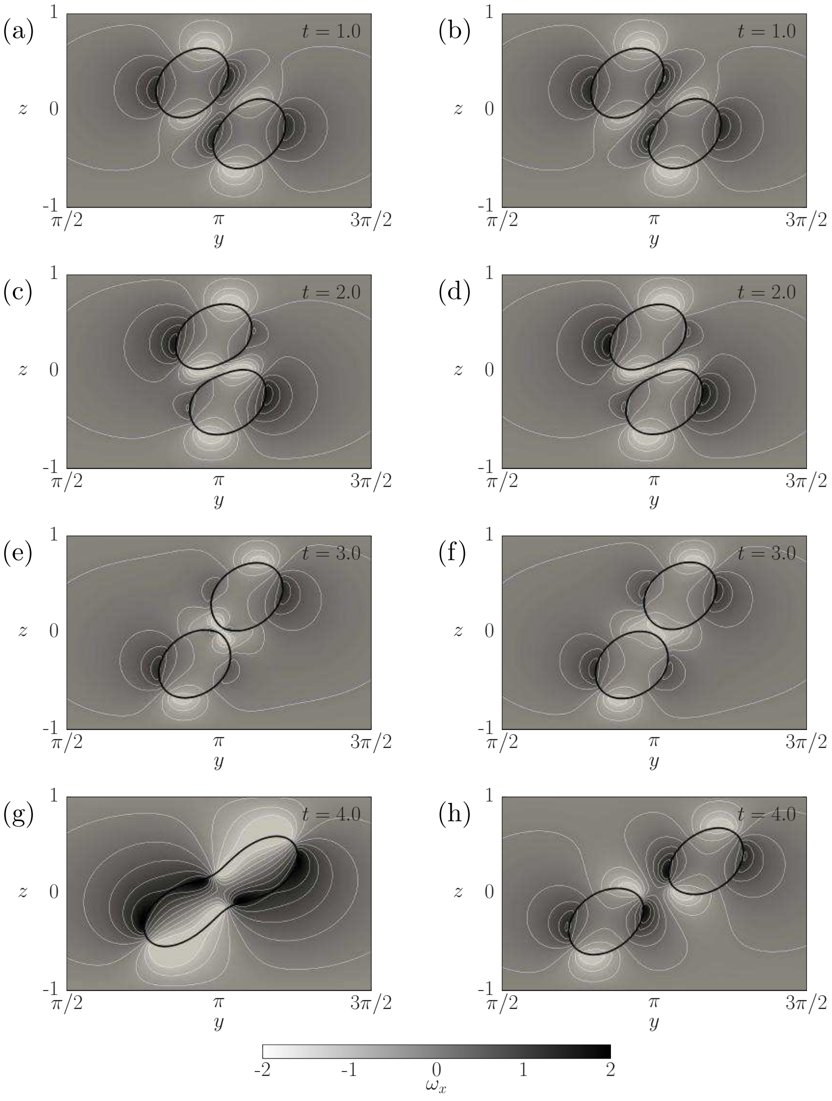

FIGURE 3.3 – Time evolution of the two droplets during the interaction. The left column, panels (a)-(c)-(e)-(g), refers to simulation B2, $\beta_s = 0.5$ and $\psi_b = 0.25 \times 10^{-2}$, while the right column, panels (b)-(d)-(f)-(h), refers to simulation C4, $\beta_s = 1.0$ and $\psi_b = 0.5 \times 10^{-2}$. The black solid line shows the instantaneous droplet interface, iso-contour $\phi = 0$. Droplets coalescence occurs for simulation B2; by opposite surfactant prevents the coalescence for the case C4. On the background, the vorticity field $\omega_x = \partial w/\partial y - \partial v/\partial z$ is plotted; iso-levels of ω_x are reported in white.

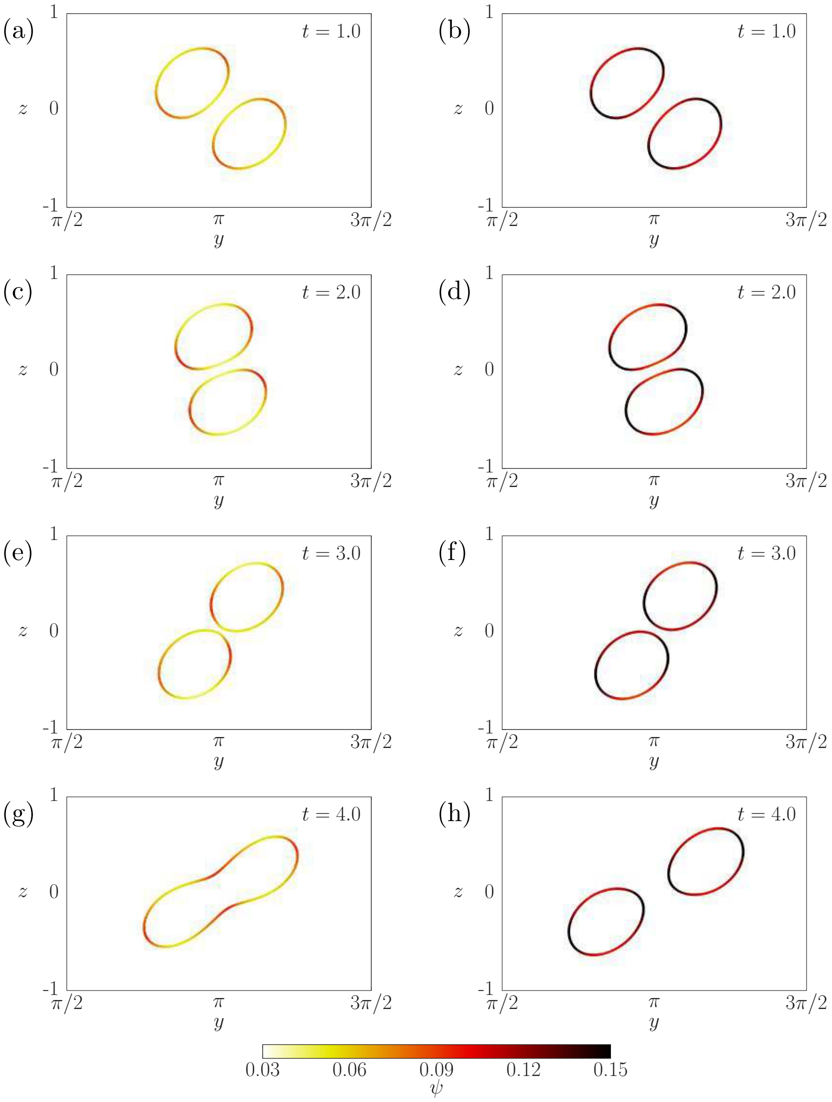

FIGURE 3.4 – Time evolution of the surfactant concentration at the droplet interface, iso-contour $\phi = 0$, during the droplet-droplet interaction. The left column, panels (a)-(c)-(e)-(g), refers to simulation B2, $\beta_s = 0.5$ and $\psi_b = 0.25 \times 10^{-2}$, while the right column, panels (b)-(d)-(f)-(h), refers to simulation C4, $\beta_s = 1.0$ and $\psi_b = 0.5 \times 10^{-2}$. For the case B2, surfactant concentration is lower, by opposite for the case C4, higher ψ_b, surfactant concentration is higher. For both the cases, surfactant accumulates at the droplets' tips. For the case B2, after the coalescence, surface tension forces reshape the droplet and surfactant redistributes.

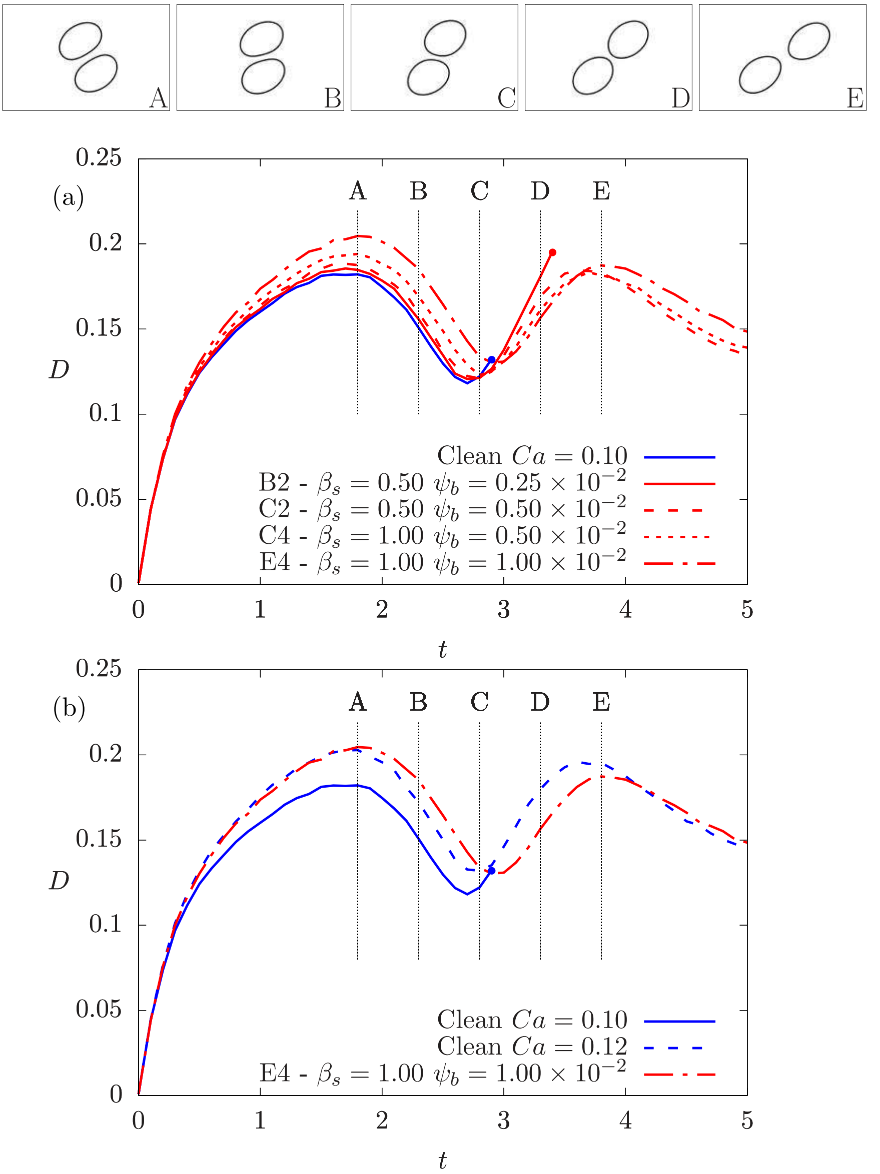

FIGURE 3.5 – Deformation parameter D of the droplets during the interaction. Panel (a) compare the results obtained at $Ca = 0.10$ and different ψ_b and β_s. As β_s and ψ_b increase, the deformation during the interaction increases as well. At $t = 2.9$, the two clean droplets coalesce (blue dot), similarly for the case B2 (red dot). For cases C2-C4-E4, droplets do not coalesce and the generic positions of the droplets are reported in the mini-panels A-B-C-D-E. In Panel (b), the case E4 (highest amount of surfactant) is compared against a clean case with an equivalent deformability.

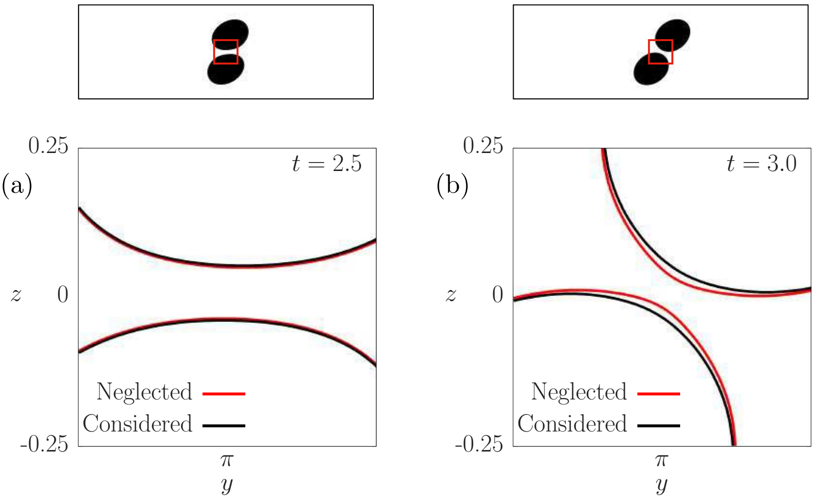

FIGURE 3.6 – Instantaneous position of the interface (iso-contour $\phi = 0$) at $t = 2.5$ in panel (a), and $t = 3.0$ in panel (b) for the simulation C2. The panels shows a close-up view of the area highlighted by the red rectangle. In black the interface location when the tangential stresses are computed, in red when the stresses are neglected. Neglecting the stresses, the distance between the two droplets is smaller.

when the droplets are less deformed (clean at $Ca = 0.10$ and case B2) and is prevented when the droplets are more deformed (clean at $Ca = 0.12$ and cases C2-C4-E4). The time behaviours of the deformation parameter D obtained are in good agreement with experiments [65] and numerical studies [156, 187, 14]. A slight difference is present in the initial stage because in the cases analysed here, droplets are released at a much shorter distance than the one used in the experiments.

3.3.3 Effect of the tangential stresses at the interface

The effect of the tangential stresses at the interface on the droplet-droplet interaction has been studied considering the case C2, $\beta_s = 0.5$ and $\psi_b = 0.5 \times 10^{-2}$. For this case the droplets do not coalesce, but when the bulk surfactant concentration ψ_b and/or of the elasticity number β_s are reduced a coalescence is obtained. For this border-line case, the simulation has been recomputed considering only the non-uniform capillary stresses and neglecting the tangential ones. Interestingly, in this new setup the two droplets coalesce. To understand the role played by the tangential stresses, the instantaneous positions of the interface ($\phi = 0$) when the stresses are considered (black) and neglected (red) have compared in Fig. 3.6(a)-(b). At $t = 2.5$, Fig. 3.6(a), the difference between the position of the interfaces is small, when the stress are neglected the two droplets are slight closer. Later, at $t = 3.0$, Fig. 3.6(b), the difference between the two interfaces is

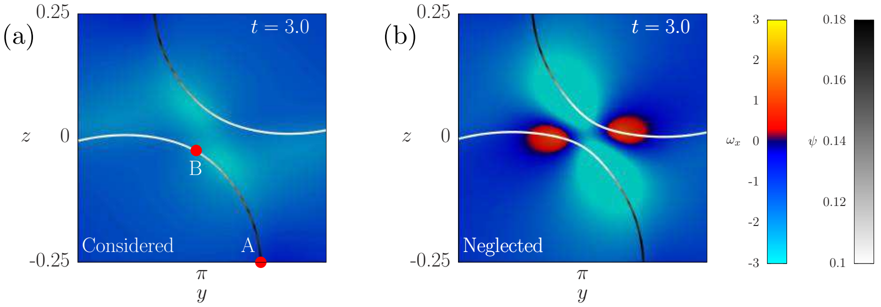

FIGURE 3.7 – Contour map of the vorticity ω_x for the simulation C2. In panel (a) the simulation is performed considering the tangential stresses while in panel (b) the stresses are neglected. The interface, iso-contour $\phi = 0$, is coloured by the surfactant concentration (white-low and black-high). The tangential stresses hamper the draining of the thin liquid film and suppress the formation of high-vorticity regions. When neglected, panel (b), the draining process is faster and regions with large fluctuations of ω_x are present (red and light-blue areas).

larger. When the tangential stresses are neglected, the two droplets are closer, whereas when considered the draining of the thin liquid film is hampered and its thickness is bigger. The different draining speed leads to a coalescence (stresses neglected) or prevent it (stresses considered).

The effect of the tangential stresses on the droplet-droplet interaction can be further elucidated considering the flow field in the gap between two droplets. In Fig. 3.7(a)-(b) the instantaneous streamwise vorticity field ω_x is shown for $t = 3.0$. In panel (a) the tangential stress are considered while in panel (b) are neglected. The interface, iso-contour $\phi = 0$, is coloured by the surfactant concentration. The tangential stresses affect the flow in the thin gap; considering Fig. 3.7(a), the stresses drive fluid from the point A (high surfactant concentration-low surface tension) towards point B (low surfactant concentration-high surface tension) and as well for the other droplet. The stresses hampering the draining avoid the formation of high-vorticity zones, indeed in the gap between the two droplets, ω_x has a value similar at the one obtained considering the mean shear flow, $\omega_x = -1$. By opposite, when neglected, Fig. 3.7(b), draining is faster and larger fluctuations of ω_x are present (red and light-blue regions).

Overall, from the results obtained the effects of the surfactant on the interaction between two droplets in shear flow have been analysed. The surfactant, decreasing the average value the surface tension, increases the deformability of the droplets. The increased deformability produces a flatter gap and this reduces the draining speed of the thin liquid film. Similarly, the tangential stresses, induced by the inhomogeneous surfactant distribution, further hinder the draining. These two effects, the increased deformability and the tangential stresses, work in the same direction hampering the draining of the liquid film and preventing the coalescence. The results obtained are in agreement with those obtained experimentally [105, 40, 181, 130] and numerically [187] for head-on and offset collision of droplets.

3.4 Conclusions

The off-centre collision of clean and surfactant-laden droplets in shear flow has been analysed. The time evolution of the system has been obtained using a Phase Field Method to track the phase field and the surfactant distribution coupled with DNS of the Navier-Stokes equation.

For a fixed value of the reference capillary number, $Ca = 0.10$, based on the surface tension of a clean interface, a wide range of bulk surfactant concentrations ψ_b and elasticity numbers β_s have been considered. From the results obtained a map of the outcome of the droplet-droplet interaction has been drawn. When surfactant is absent or low bulk surfactant concentrations ψ_b are considered the two droplets coalesce. By opposite, increasing the bulk surfactant concentration ψ_b and the elasticity number β_s, the surfactant is able to prevent the coalescence. Indeed, the increased deformability (lower surface tension) and the tangential stresses at the interface (inhomogeneous surfactant distribution) hamper the draining of the thin liquid film present between the two droplets. Both the effects, induced by the surfactant, have a positive effect in preventing the coalescence.

4

Viscosity stratified turbulent flow

Reproduced in part from:
S. Ahmadi, A. Roccon, F.Zonta and A. Soldati, Turbulent drag reduction in channel flow with viscosity stratified fluids, Computers & Fluids, (2017).

S. Ahmadi, A. Roccon, F.Zonta and A. Soldati, Turbulent drag reduction by a near wall surface tension active interface, Flow, Turbulence & Combustion, submitted.

A. Roccon, F.Zonta and A. Soldati, Turbulence annihilation with viscosity stratified fluids, Journal of Fluid Mechanics, in preparation.

4.1 Problem definition

Turbulent flows of two immiscible and stratified fluids are often observed in the process and petroleum industry. Important examples include oil-water separators and hydrocarbon transportation pipelines. In these situations, two-immiscible phases, are driven inside pipelines/channels, the interaction between the two phases, and in particular the exchange of momentum through the interface can change the behaviour of the system. The prediction of the flow configuration is crucial to optimise the design of these systems and depends on different parameters, as the relative speed of the two phases, viscosity and density contrast and the magnitude of the interfacial forces. From a practical point of view, stratified condition has several advantages: *i*) the power required to transfer the oil/water flow is lower (due to the lower viscosity of water wetting a wall compared to that of the

oil) *ii*) oil can be easily separated from water.
Following this idea, in the last decades, several studies have focused on this topic and have tried to understand the stability and the performance of such a configuration [60, 68, 73, 30]. Most of them has been performed experimentally using very low viscosity ratios [33, 12, 33, 83, 96]. Only recently this problem has been studied numerically [110, 185]. The use of a numerical approach imposes a series of challenges to overcome, from the interface description to the treatment of the different thermophysical proprieties. The viscosity stratified flow has been analysed performing Direct Numerical Simulation (DNS) of the Navier-Stokes equation coupled with a Phase Field Method (PFM) to track the interface. Starting from the case where only the role of the interface is considered, i.e. matched density and viscosity, different levels of viscosity stratification have been considered.

4.2 Simulation setup

The system considered is made of a thin layer, thickness $t_1 = 0.15h$, which flows on the top of a thicker layer, thickness $t_2 = 1.85h$, Fig. 4.1. The two layers have the same density, $\rho = \rho_1 = \rho_2$, but different viscosity, $\eta_1 \leq \eta_2$. The setup adopted try to mimic a core annular flow where a low viscosity fluid, as for example water, is used to help the transport of crude oil. The use of the real water-oil viscosity ratio, $\lambda = \eta_1/\eta_2 \simeq 10^{-3}$, would require computational resources nowadays not available. For this reason, the values of λ used span from $\lambda = 1$ to $\lambda = 0.25$. The two phases are separated by an interface with surface tension $\sigma = \sigma_0$, here assumed constant. The time behaviour of the system can be described solving continuity, Navier-Stokes and Cahn-Hilliard equations:

$$\nabla \cdot \mathbf{u} = 0 \tag{4.1}$$

$$\begin{aligned} \frac{\partial \mathbf{u}}{\partial t} + \mathbf{u} \cdot \nabla \mathbf{u} &= \frac{1}{Re_\tau} \nabla^2 \mathbf{u} + \frac{1}{Re_\tau} \nabla \cdot (\eta(\phi)(\nabla \mathbf{u} + \nabla \mathbf{u}^T)) - \nabla p \\ &+ \frac{3}{\sqrt{8}} \frac{Ch}{We} \nabla \cdot (|\nabla \phi|^2 \mathbf{I} - \nabla \phi \otimes \nabla \phi)) \end{aligned} \tag{4.2}$$

$$\frac{\partial \phi}{\partial t} + \mathbf{u} \cdot \nabla \phi = \frac{1}{Pe_\phi} \nabla^2 (\phi^3 - \phi - Ch^2 \nabla^2 \phi) \tag{4.3}$$

The following dimensionless groups appear:

$$Re_\tau = \frac{\rho u_\tau h}{\eta_2} \quad We = \frac{\rho u_\tau^2 h}{\sigma_0} \quad \lambda = \frac{\eta_1}{\eta_2} \quad Ch = \frac{\xi}{h} \quad Pe_\phi = \frac{u_\tau h}{\mathcal{M}_\phi \beta} \tag{4.4}$$

Equations 4.3 - 4.2 and 4.1 are solved in a closed channel geometry with dimensions $L_x \times L_y \times L_z = 4\pi h \times 2\pi h \times 2h$. The flow is driven along the streamwise direction by a constant mean pressure gradient. All the simulations start from a flow field obtained from a Direct Numerical Simulation (DNS) of a single phase fully developed turbulent channel flow at $Re_\tau = 300$. The reference shear Reynolds number, based on the viscosity of the fluid 2, η_2, has been fixed to $Re_\tau = 300$ and three values of the viscosity ratio λ have been considered, $\lambda = 1.00 - 0.50 - 0.25$. Considering the time and length-scale of the flow, different grid resolutions have been used. Indeed, when viscosity ratios, $\lambda < 1$, are considered, at the top wall the local shear Reynolds number increases and thus the grid requirements. To ensure the resolution of all the relevant scales of the flow, different grid resolutions have been used, from $N_x \times N_y \times N_z = 512 \times 256 \times 257$ for the single phase case up to $N_x \times N_y \times N_z = 1024 \times 512 \times 513$ for $\lambda = 0.25$. For the worst scenario, $\lambda = 0.25$, the grid spacing (based on the semi-local Reynolds number Re^*, as defined by [132, 131, 134] for variable proprieties turbulent channel flow) is equal to $\Delta x^* = \Delta y^* = 11.41$ along the homogenous directions and $\Delta z^*_w = 0.018$ along the wall-normal direction (wall). Considering the value of the surface tension of an oil-water mixture [169, 89], the Weber number has been set to $We = 0.5$. The initial condition used for ϕ, is a flat interface located at a distance $\Delta z = 0.15h$ from the top wall. The Cahn number has been chosen considering the coarsest grid and the requirement to have at least 3 nodes across the interface. In order fo fulfil these requirements $Ch = 0.0185$ has been adopted. Along the wall normal direction, where the grid is finer, at least 5 nodes are always present across the interface. Following [120], the Peclet number is set to $Pe_\phi = 162.2$ In the following, the results obtained are presented using the wall units scaling system. Starting from the dimensional analysis presented in Sec. 1.4; the new results expressed in the wall units can be obtained as follows:

Sim.	We	λ	N_x	N_y	N_z
SP	-	-	512	256	257
S1	0.5	1.00	512	256	257
S2	0.5	0.50	512	256	513
S3	0.5	0.25	1024	512	513

Table 4.1 – Summary of the parameters used for the simulations. SP identifies a single phase simulation. The cases S1-S2-S3 refer to viscosity stratified flows.

$$\mathbf{x}^+ = Re_\tau \mathbf{x} \qquad \mathbf{u}^+ = \mathbf{u} \qquad t^+ = Re_\tau t \qquad \phi^+ = \phi \tag{4.5}$$

These changes will affect only the channel dimensions, $\mathbf{u}$ and ϕ keep the same values. In wall units the dimensions of the channel are $L_x^+ \times L_y^+ \times L_x^+ = 3770 \times 1885 \times 600\ w.u.$ The thickness of the two liquids layers are respectively $t_1^+ = 45\ w.u.$ (top layer) and $t_2^+ = 555\ w.u.$ (bottom layer).

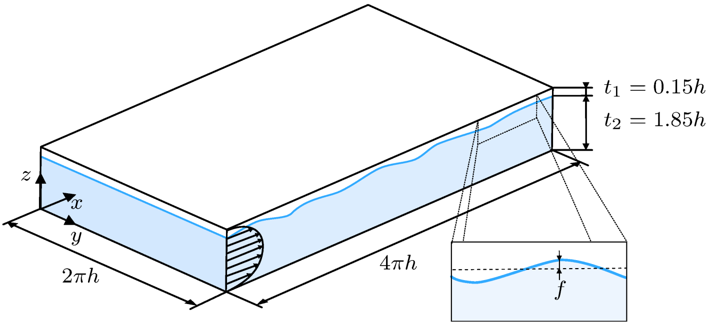

FIGURE 4.1 – Geometry considered in the simulations. Two liquid layers, one on top of each other, flow inside a channel along the streamwise direction. The bottom layer has a thickness $t_2 = 1.85h$ and the top layer has a thickness $t_1 = 0.15h$. In the close-up view the interface elevation f is highlighted.

4.3 Results and discussion

The results obtained from the viscosity stratified turbulent flow will be here discussed and analysed. First, the macroscopic behaviour of the flow has been analysed considering the flow rate and mean wall shear stress behaviour. Then, the effects of the deformable interface and of the viscosity ratio on the turbulence have been analysed.

4.3.1 Flow rates and mean wall shear stress

Simulations are run starting from a single phase turbulent flow at $Re_\tau = 300$. For all the multiphase simulations, an initial transient is present. Indeed, the flow must adapt to the interface and to the different viscosity of the thin layer. After $t^+ \simeq 5000$, a new statistical steady-state configuration is reached for all the cases. Once obtained, the normalised flow rate $(Q - Q_{SP})/Q_{SP}$ and the mean wall shear stress at the two walls, $\langle \tau_w^1 \rangle$ and $\langle \tau_w^2 \rangle$, are computed. In the following, angular brackets $\langle \cdot \rangle$ denote averaging in time and over the homogeneous directions.
First, the time evolution of the flow rate Q of the thicker fluid layer (fluid 2) across the channel section has been considered. Results are normalised by the reference volume flow rate of the single phase case, Q_{SP}, at the same reference Re_τ. From Tab. 4.2, it can be observed that even for $\lambda = 1$, the presence of a deformable interface separating the two fluid layers induces an overall increase of the volume flow rate (up to $\simeq 19\%$). This indicates that the wall normal transport of momentum is reduced, with a significant proportion of the mean flow energy being lost into interface deformation. Reducing λ, the volume flow rate slightly decrease ($\simeq 15\%$ for $\lambda = 0.25$). Since our simulations are run with an imposed pressure gradient, an in-

Sim.	λ	$(Q - Q_{SP})/Q_{SP}$	$\langle\tau_w^1\rangle/\lvert\langle\tau_w^{SP}\rangle\rvert$	$\langle\tau_w^2\rangle/\lvert\langle\tau_w^{SP}\rangle\rvert$
SP	-	0.000	-1.000	1.000
S1	1.00	0.196	-0.595	1.405
S2	0.50	0.151	-0.635	1.365
S3	0.25	0.153	-0.606	1.394

TABLE 4.2 – Normalised flow rate $(Q - Q_{SP})/Q_{SP}$ for the different simulations. Q is the flow rate of the crude oil (fluid 2). Compared to the single phase case, an increase of the flow rate is observed. Decreasing λ, the flow rate slightly decreases. In the 4^{th} and 5^{th} columns the mean wall shear stress at the two walls are reported. $\langle\tau_w^1\rangle$ refers to the top wall (fluid 1) and $\langle\tau_w^2\rangle$ refers to the bottom wall (fluid 2). At the top wall, the mean wall shear stress are decreased. By opposite, at the bottom wall are increased.

crease of the mean volume flow rate is directly related to modifications in the mean wall shear stress. The explicit computation of the wall shear stress (normalised with the wall shear stress of a single phase flow, $|\langle\tau_w^{SP}\rangle|$) for the different simulations (at the bottom and the top wall), are summarised in Tab. 4.2. It's important to note, that since the viscosity η_2 has been chosen as reference, the mean wall shear stress at the two walls is computed as follows:

$$\tau_w^1 = \lambda \frac{\partial u^+}{\partial z^+} \qquad \tau_w^2 = \frac{\partial u^+}{\partial z^+} \tag{4.6}$$

The superscripts used refer to top (fluid 1) and bottom wall (fluid 2). From Tab. 4.2, it can be observed that for all the multiphase simulations the mean wall shear stresses at the bottom wall are increased. By opposite, since the flow is driven by a constant mean pressure gradient and thus: $|\langle\tau_w^1\rangle| + |\langle\tau_w^2\rangle| = \text{const}$, at the top wall the mean wall shear stresses are reduced.

4.3.2 Fluid velocity statistics

Linked to the observed changes of the volume flow rate and of the mean wall shear stress, large modifications of the mean streamwise velocity are expected. In Fig. 4.2, the wall-normal behaviour of the mean streamwise velocity $\langle u^+\rangle$ has been explicitly shown for the different λ considered. The wall-normal coordinate is expressed in wall units, the reference position of the interface is explicitly shown by a dashed line. Compared to the reference case of a single phase flow (thin black line) the presence of two different fluid layers separated by a deformable interface alters the symmetry of the profile. Larger values of the velocity characterise the thick fluid layer ($0 < z^+ < 555$). For the thin layer, only for $\lambda = 1$, smaller values of the velocity characterise the first part of the thin fluid layer ($570 < z^+ < 600$). Considering the cases $\lambda = 0.50$ and $\lambda = 0.25$, the low viscosity leads to larger values of the mean velocity.

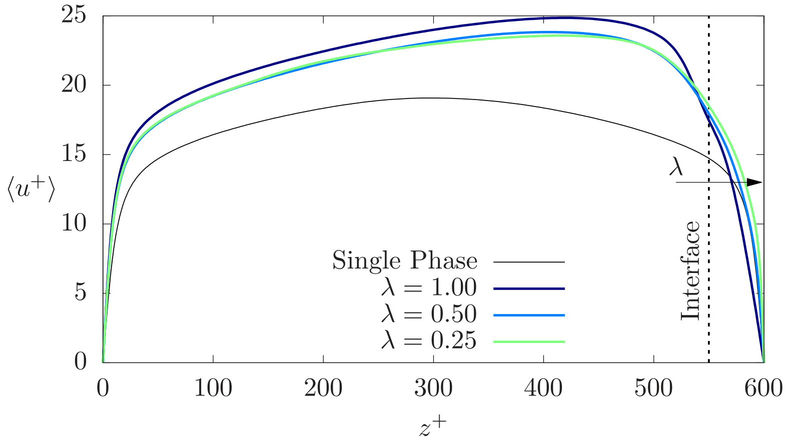

FIGURE 4.2 – Mean streamwise velocity profile. The continuous thin line refers to the single phase flow. The thick lines refer to the multiphase simulations: $\lambda = 1.00$ (blue), $\lambda = 0.50$ (light blue) and $\lambda = 0.25$ (green). For all the viscosity ratios considered, larger values of the mean velocity are observed. The initial interface location is highlighted by a dashed line.

To give a better insight of the modifications produced by the interface and by the viscosity ratio, in Fig. 4.3, for the cases SP,S1,S3, colormaps of the instantaneous streamwise velocity u^+ on a $y^+ - z^+$ section of the channel are reported. Compared to the single phase case, Fig. 4.3(a), the behaviour of the multiphase flow is very different. Considering the case S1 ($\lambda = 1.00$ and Fig. 4.3(b)), the deformable interface decreases the turbulence activity at the top wall. By opposite, since the flow is driven a mean pressure gradient, at the bottom wall the activity is increased. Decreasing the viscosity of the thin layer, case S3 ($\lambda = 1.00$ and Fig. 4.3(c)), at the top wall the turbulence is partially restored, but the lower viscosity (higher local Re) decreases the characteristic size of the turbulent structures. Even for this case (S3), at the bottom wall the turbulent activity increases.

To quantify the previous observations, the Root Mean Square (RMS) of the velocity vector fluctuations $\langle RMS(u'^+)\rangle$, $\langle RMS(v'^+)\rangle$ and $\langle RMS(w'^+)\rangle$ have been considered. The computation of these statistics in the upper part requires the definition of non-standard decomposition and has been omitted. Indeed, in the upper part, the averaging procedure is affected by the contemporary presence of both the phases and by the flow perturbations induced by the interface.

In Fig. 4.4(a) the RMS of the three velocity components are reported. The results are computed using the wall-units scaling system, based on the reference Reynolds number Re_τ. For all the three components, streamwise (continuous line), spanwise (dashed line) and wall normal (dotted line), an increase of the turbulence activity can be observed. Indeed the steeper

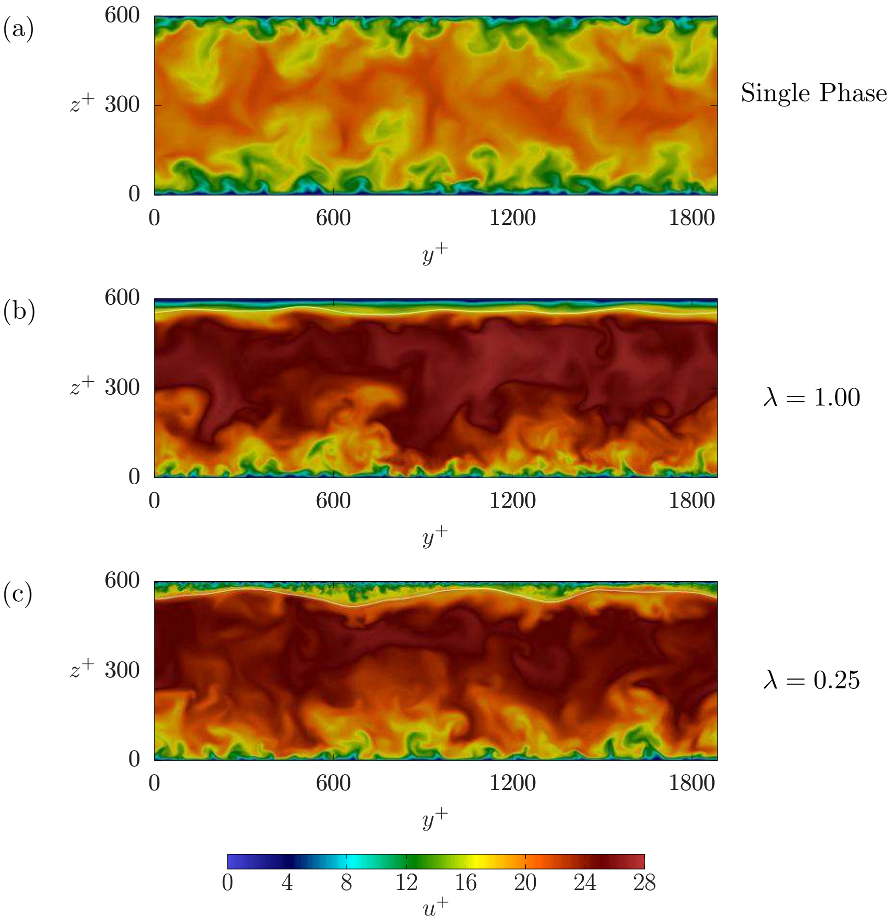

FIGURE 4.3 – Colormap of the instantaneous streamwise velocity u^+ in a $y-z$ section of the channel. Panel (a) refers to the single phase case (SP), panel (b) to the case S1, $\lambda = 1.00$, and panel (c) to the case S3, $\lambda = 0.25$. The interface, iso-contour $\phi = 0$, is reported with a white line. Compared to the single phase, the flow is asymmetric, a decrease of the turbulent activity can be observed for $\lambda = 1.00$. Decreasing the viscosity ratio, $\lambda = 0.25$, turbulence is partially restored and the structures are smaller.

gradient of the mean velocity $\langle u^+ \rangle$ enhances the production of turbulent kinetic energy. In addition, the peak of $\langle RMS(u'^+) \rangle$ is shifted towards the bottom wall (from $z^+ \simeq 12$ to $z^+ \simeq 10$). The results obtained, following [132, 131, 134], can be rescaled using the semi-local Reynolds number, Re_*, defined as follows:

$$Re_*^1 = (Re_\tau/\lambda)\sqrt{|\langle \tau_w^1 \rangle| / |\langle \tau_w^{SP} \rangle|} \qquad \text{Top wall} \qquad (4.7)$$

$$Re_*^2 = Re_\tau \sqrt{|\langle \tau_w^2 \rangle| / |\langle \tau_w^{SP} \rangle|} \qquad \text{Bottom wall} \qquad (4.8)$$

Sim.	λ	Re_*^1	Re_*^2
SP	-	300	300
S1	1.00	363	236
S2	0.50	351	480
S3	0.25	352	930

Table 4.3 – Values of the semi-local Reynolds number at the two walls. The superscript 1 identifies the bottom wall and the superscript 2 the top wall. At the bottom wall, the increased mean wall shear stress marginally increase Re_*. By opposite, at the top wall, mean wall shear stress are reduced but the low viscosity leads to an increase of Re_* ($\lambda = 0.50$ and $\lambda = 0.25$).

The semi-local Reynolds accounts for the change in the friction velocity and in the viscosity at the two walls. The values of Re_* for the different cases have computed and are reported in Tab. 4.3 Using the semi-local scaling system, the different quantities are rescaled as follows (for the bottom wall):

$$\mathbf{x}^* = \frac{Re_\tau}{Re_*}\mathbf{x}^+ \qquad \mathbf{u}^* = \frac{Re_\tau}{Re_*}\mathbf{u}^+ \tag{4.9}$$

In Fig. 4.4(b) the rescaled RMS are reported. It can be observed that after the rescaling the results are in good agreement with the ones obtained from a single phase flow (black line). The slight difference between the profiles is due to a Reynolds number effect, since the single phase statistics refers to a lower shear Reynolds number, $Re_\tau = 300$. Overall, at the bottom wall, the turbulence is not affected by the interface and the lower behaves as a single phase but with a slight larger Reynolds.

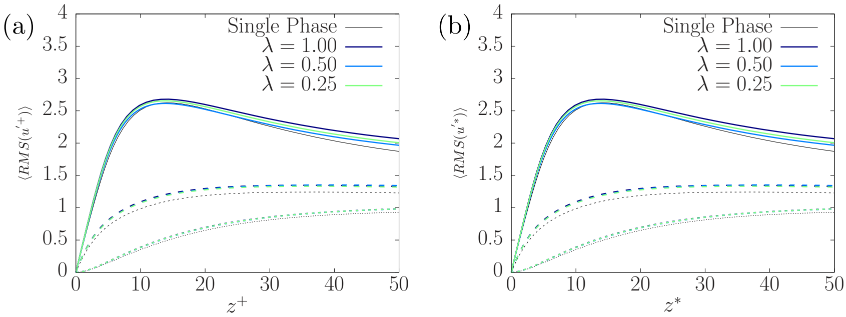

Figure 4.4 – Root Mean Square (RMS) of the velocity fluctuations in the lower part of the channel. In the panel (a) the results are obtained using the wall units scaling system, based on the reference Reynolds number Re_τ. In the panel (b) the results are shown using the semi-local scaling system, based on the semi-local Reynolds number Re_*^1. Streamwise component (continuous line), spanwise component (dashed line) and wall-normal (dotted line). The increase of the mean wall shear stress at the bottom wall increases Re_*^1. Rescaling the results, panel (b), a good agreement with the single phase statistics is found.

4.3.3 Wall shear stress distribution

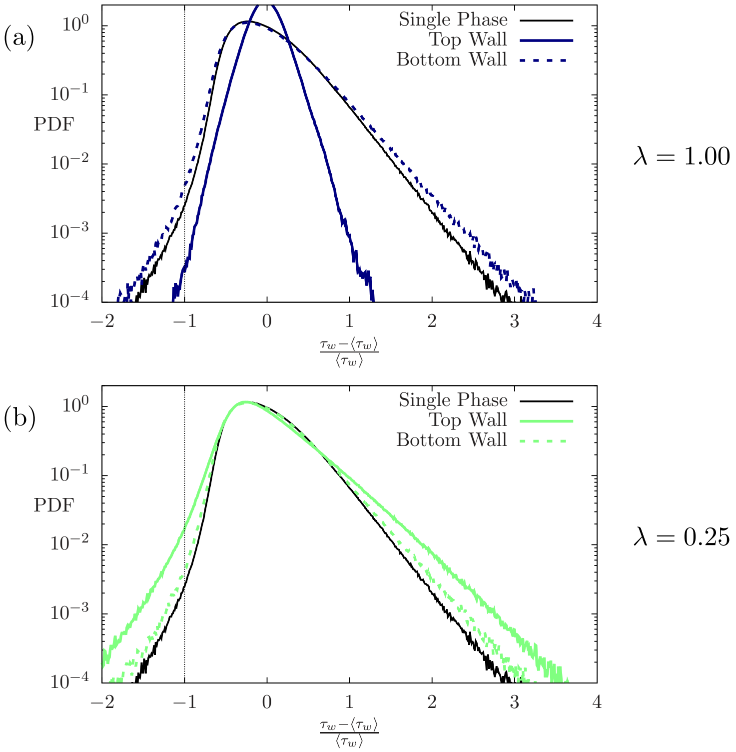

FIGURE 4.5 – Probability Density Function (PDF) of the normalised wall shear stress τ'_w. Panel (a) refers to $\lambda = 1.00$, panel (b) refers to $\lambda = 0.25$. A thin black line identify the results obtained from a single phase case at the same reference Re_τ. At the bottom wall, for both the cases, the behaviour is similar at the single phase case. At the top wall, for $\lambda = 1.00$, the interface modifies the shape of the PDF, the most probable events occurs at. For $\lambda = 0.25$, the turbulence at the top wall is recovered and the PDF shown a behaviour similar at the single phase profile.

To characterise the influence of the liquid-liquid interface on the near wall turbulence, the Probability Density Function (PDF) of the wall shear stress at the top and bottom wall have been computed, Fig. 4.5. In particular, we consider the normalised deviations of the wall shear stress with respect to the mean value at the corresponding wall, i.e. $\tau'_w = (\tau_w - \langle\tau_w\rangle)/\langle\tau_w\rangle$. In Fig. 4.5(a)-(b), the PDFs at the top and at the bottom wall for $\lambda = 1.00$ (blue) and $\lambda = 0.25$ (green) are reported. A thin continuous line identifies the PDF obtained from a single phase flow. For all the cases reported, the PDF is asymmetric, with the most probable value occurring for $\tau'_w \simeq -0.1$ (top wall, $\lambda = 1.00$) or $\tau'_w \simeq -0.3$ (other cases). In addition, positive normalised wall shear stresses being larger and more probable than the negative

ones [97, 183, 76, 61].
Larger modifications are observed at the top wall for $\lambda = 1.00$; the occurrence of larger wall shear stress fluctuations of τ'_w is reduced. This indicates that the wall shear stress fluctuations are largely reduced by the liquid-liquid interface, which acts as a barrier to the turbulent generation cycle (hence reducing the wall shear stress fluctuations). These interface-induced modifications are weaker when $\lambda = 0.25$ is considered. The low viscosity promotes a recover of the near-wall turbulence and the occurrence of larger wall shear stress fluctuations is increased. Considering the bottom wall, for both the cases, only few differences are observed between the multiphase and single phase case, a slight increase of the probability of large fluctuations can be observed. The increased occurrence of large shear stress fluctuations can be linked to the different values of the semi-local shear Reynolds number. This behaviour reported is in good agreement with the findings of [76, 107, 21]. Lastly, the presence of back-flow regions (areas in which τ_w and $\langle \tau_w^{1/2} \rangle$ have different sign and thus $\tau'_w < -1$) can be observed. The occurrence of these events increase with Re^* [107]. A qualitative picture of a back-flow region close to the bottom wall is shown in Fig. 4.6. The figure reports the instantaneous streamlines on a x^+-y^+ slice located at $z^+ = 0.3$ $w.u.$ The shape of this area is circular [107] and has an extension of 20 $w.u.$

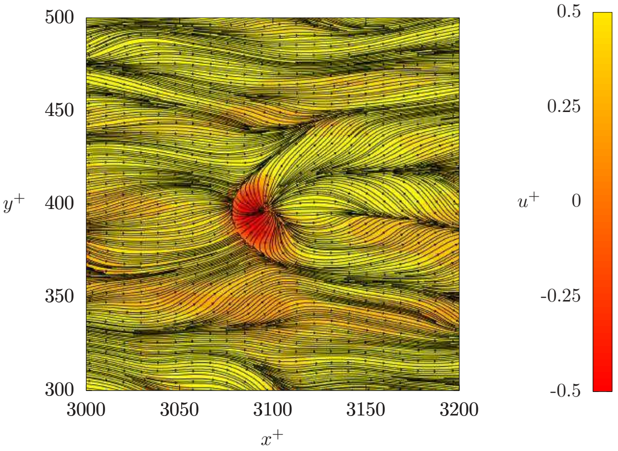

FIGURE 4.6 – Back-flow region located near the bottom wall. The section refers to a x^+-y^+ slice located at 0.6 $w.u.$ from the wall. The instantaneous streamlines based on the spanwise and streamwise velocity components are used to visualise the flow. On the background the streamwise velocity u^+ is shown.

4.3.4 Interface-near wall turbulence interactions

The mechanism, by which the interface interacts with the near-wall turbulence, can be elucidated further examining the instantaneous interface

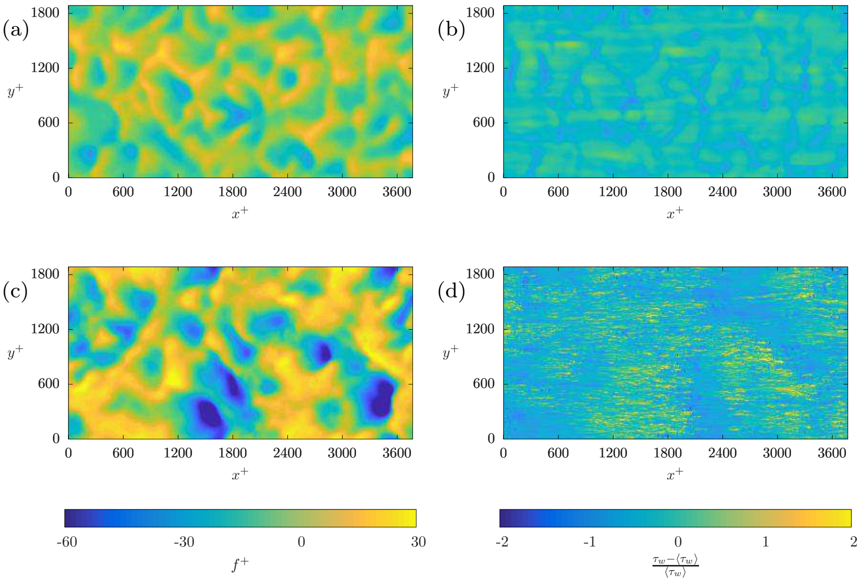

FIGURE 4.7 – Joint Probability Density Function (joint PDF) between the normalised wall shear stress τ'_w at the top wall and the interface elevation f^+. Panel (a) refers to $\lambda = 1$ and panel (b) to $\lambda = 0.25$. Decreasing λ, the peak move towards $\tau'_w \simeq 0.35$, $f^+ \simeq 20$ and the shape become rounded. Furthermore the slopes at the bottom and at the right sides are increased.

elevation and the wall shear stress at the top wall. A qualitative picture showing the behaviour of τ'_w and f^+ is given in Fig. 4.7.

In panels (a)-(c), the dark-blue colour identifies a negative interface elevation, f^+, (interface far from the wall) vice versa for the yellow (interface close to the wall). In panels (b)-(d), the dark-blue colour identifies negative wall shear stress fluctuations, $\tau'_w < 0$, and vice versa for the yellow. Considering the panels (a)-(b), $\lambda = 1.00$, a correlation between positive interface elevations and negative wall shear stress fluctuations can be observed. When the case $\lambda = 0.25$ is considered, panels (c)-(d), the correlation is less clear.

To give these observations a more quantitative slant, the joint Probability Density Function of the normalised wall shear stress τ'_w at the top wall and the interface elevation f^+ has been computed for the cases $\lambda = 1$, Fig. 4.8(a) and $\lambda = 0.25$, Fig. 4.8(b). Considering $\lambda = 1$, the results seem to confirm the qualitative behaviour previously observed. An asymmetry can be noted, in particular in the 4^{th} quadrant ($f^+ > 0$ and $\tau'_w < 0$). The interface, moving towards the wall, induces negative wall shear stress fluctuations. Decreasing the viscosity of the thin liquid layer, $\lambda = 0.25$, these interactions are weaker and indeed the joint PDF is less asymmetric. For this case, as seen before in Fig. 4.5, the low viscosity increases the wall shear stress fluctuations, the turbulence is partially restored and the interface-wall turbulence interaction

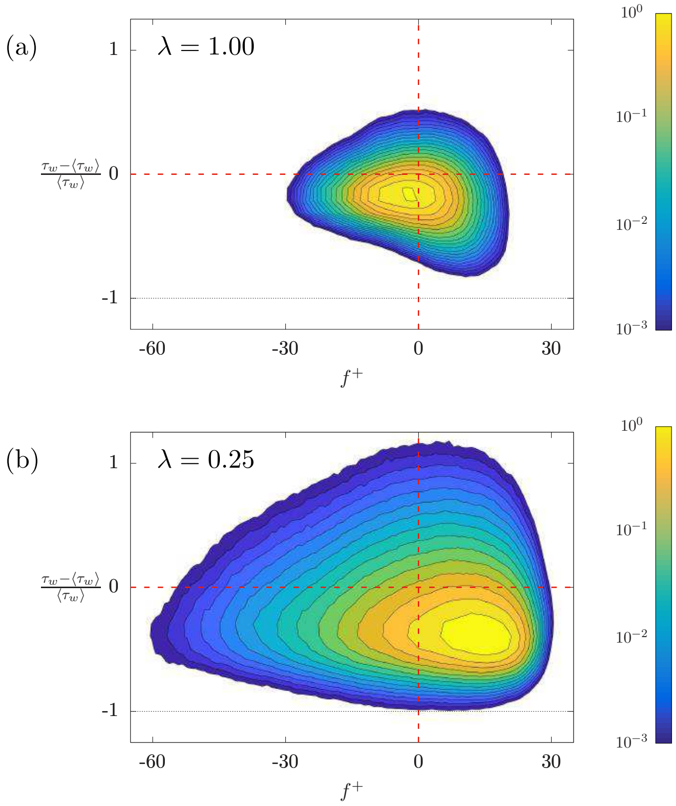

FIGURE 4.8 – Joint Probability Density Function (joint PDF) between the normalised wall shear stress τ'_w at the top wall and the interface elevation f^+. Panel (a) refers to $\lambda = 1.00$ and panel (b) to $\lambda = 0.25$. Decreasing λ, the peak move towards $\tau'_w \simeq 0.35$, $f^+ \simeq 20$ and the shape become rounded. Furthermore the slopes at the bottom and at the right sides are increased.

is weaker.

4.4 Conclusions

Using direct numerical simulation of Navier-Stokes and Cahn-Hilliard equations, a viscosity stratified flow has been analysed. A thin low viscosity layer is used to reduce the friction loss and increase the flow rate. For the range of viscosity ratios λ considered, the drag reduction (DR) performance is only slightly affected by the viscosity ratio λ.

The interaction between the interface and the near-wall turbulence structures plays a crucial role. For the case $\lambda = 1.00$, the interface is able to largely annihilate the near-wall turbulence at the top wall. Consequently, the mean wall shear stress on this wall are reduced and since the flow is driven by a constant mean pressure gradient the flow rate increases. Decreasing the viscosity of the thin layer (decreasing λ) the interface-near wall turbulence interaction is weaker, near-wall turbulence is partially recovered. Despite this, the low viscosity balances out the turbulence recovery and the mean wall shear stress are similar at the ones obtained for the case $\lambda = 1.00$.

Conclusions and further developments

Direct Numerical Simulation of multiphase system have been performed to characterise the interactions between deformable interface and turbulence. In Chap. 2, the time behaviour of a swarm of large deformable drops released in a turbulent channel flow has been analysed. Different values of the surface tension and of the viscosity ratios between the two phases have been considered. The drops, interacting with the flow and with the neighbour drops, coalesce and breakup, after an initial transient an equilibrium between the two phenomena is observed. The steady-state number of drops and their average dimension do not depend only on the surface tension, but also the internal viscosity play a crucial role. The role played by the internal viscosity is particularly enhanced when low surface tension values are considered. The mean drop diameter, has been compared against the results obtained by [69, 26, 179, 180]. For $\lambda < 1$, case considered in the experiments, a good agreement has been found.

In Chap. 3, the effects of the surfactant in the interaction between two colliding droplets in a shear flow has been considered. The interface shape and the surfactant concentration have been tracked using a phase field method approach. Starting from a two-order parameters Ginzburg-Landau free energy functional [171, 52], the time behaviour of ϕ (phase distribution) and ψ (surfactant concentration) can be efficiently described. The framework proposed, coupled with the Navier-Stokes equation is able to accurately describe the flow-interface-surfactant interactions. Considering the problem of two colliding droplets in shear flow, the surfactant, increasing the droplet's deformability, and giving rise to tangential stress along the interface can inhibit the coalescence. The mechanism is effective only when the surfactant concentration and the elasticity number are large enough.

In Chap. 4, the turbulent flows of two immiscible and viscosity stratified fluids has been considered. The setup adopted mimics a core annular flow where a low viscosity fluid, as for example water, is used to help the transport of crude oil [33, 12]. The interactions between the interface and near-wall turbulence structures play a crucial role and even when the viscosity of the two phases is matched, an increase of the flow rate is observed (up to $\simeq 16\%$). In particular, the interface is able to modulate the turbulence and a decrease of the mean wall shear stress is observed. Decreasing the viscosity ratio, the turbulence-interface interactions are weakened but at the same time the low viscosity promote a further increase of the flow rate. The sum of these two effects leads to an increase of the flow rate for all the range of viscosity ratio analysed. The increase is only slightly influenced by the viscosity ratio.

Overall, in this thesis, the turbulence-interface interactions have been analysed in different flow configurations. The work has been performed with the aid of Direct Numerical Simulation (DNS) coupled with a Phase Field Method (PFM) to track the interface and the surfactant concentration. The mathematical framework proposed is extremely powerful and can accurately describe the behaviour of turbulent multiphase flow.

A

Publications, courses and projects

A.1 Referred journals

J1 **Roccon, A.**, Zonta F. and Soldati, A. Turbulence annihilation with viscosity stratified fluids, *Journal of Fluid Mechanics*, in preparation.

J2 Soligo, G., **Roccon, A.** and Soldati, A. Interaction of turbulence with a large deformable bubble, *Acta Mechanica*, in preparation.

J3 Soligo, G., **Roccon, A.** and Soldati, A. Phase Field Method to predict coalescence of clean and surfactant-laden droplets, *Journal of Computational Physics*, in preparation.

J4 Ahmadi, S., **Roccon, A.**, Zonta, F. and Soldati, A. (2017). Turbulent drag reduction by a near wall surface tension active interface, *Flow, Turbulence & Combustion*, submitted.

J5 Ahmadi, S., **Roccon, A.**, Zonta, F. and Soldati, A. (2017). Turbulent drag reduction in channel flow with viscosity stratified fluids, *Computers & Fluids*, in press.

J6 **Roccon, A.**, De Paoli, M., Zonta, F. and Soldati, A. (2017). Viscosity-modulated breakup and coalescence of large drops in bounded turbulence, *Physical Review Fluids*, Volume 2(8).

A.2 Referred conferences

C1 **Roccon, A.**†, M. De Paoli, Zonta, F. and Soldati A., (2017) Viscosity-modulated breakup and coalescence of large drops in bounded turbulence *APS-DFD Annual Meeting*, Denver (CO, USA), November 19-21, 2017.

C2 Ahmadi, S., **Roccon, A.**, Zonta, F. and Soldati A.[†], (2017) Turbulent annihilation in surface tension stratified flow *APS-DFD Annual Meeting*, Denver (CO, USA), November 19-21, 2017.

C3 Soligo, G.[†], **A. Roccon** and Soldati A., (2017) Turbulence interactions with large bubbles *APS-DFD Annual Meeting*, Denver (CO, USA), November 19-21, 2017.

C4 M. De Paoli[†], **A. Roccon** and Soldati A., (2017) A phase-field method to analyze the dynamics of immiscible fluids in porous media *APS-DFD Annual Meeting*, Denver (CO, USA), November 19-21, 2017.

C5 **Roccon, A.**, Zonta, F.[†] and Soldati A., (2016) Viscosity-modulated breakup and coalescence of large drops in bounded turbulence *TSFP10*, Chicago (IL,USA), July 6-9, 2017.

C6 **Roccon, A.**, Zonta, F. and Soldati A.[†], (2016) Viscosity-modulated breakup and coalescence of large drops in bounded turbulence *ICNMMF-III*, Tokyo (Japan), May 26-29, 2017.

C7 **Roccon, A.**[†], Zonta, F. and Soldati A., (2016) Viscosity-modulated breakup and coalescence of large drops in bounded turbulence *PRACE Days 17*, Barcelona (Spain), May 15-18, 2017.

C8 **Roccon, A.**, Zonta [†], F. and Soldati A., (2016) Viscosity-modulated breakup and coalescence of large drops in bounded turbulence *ETPFGM53*, Gdansk (Poland), April 22-24, 2017.

C9 **Roccon, A.**[†], Zonta, F. and Soldati A., (2016) Energy Transfers in channel flow with viscosity stratified fluids *EDRFCM*, Monte Porzio Catone (Italy), April 3-6, 2017.

C10 **Roccon, A.**, Zonta [†], F. and Soldati A., (2016) Viscosity-modulated breakup and coalescence of large drops in bounded turbulence *Austrian HPC Metting*, Grundlsee (Austria), March 1-3, 2017.

C11 **Roccon, A.**[†], Zonta, F. and Soldati A., (2016) Viscosity-modulated breakup and coalescence of large drops in bounded turbulence *APS-DFD Annual Meeting*, Portland (OR, USA), November 20-22, 2016.

C12 Ahmadi, S., **Roccon, A.**, Zonta, F. and Soldati A.[†], (2016) Turbulent drag reduction in channel flow with viscosity stratified fluids, *APS-DFD Annual Meeting*, Portland (OR, USA), November 20-22, 2016.

C13 **Roccon, A.**[†], Zonta, F. and Soldati A., Turbulent drag reduction in channel flow with viscosity stratified fluids, *Ercoftac Meeting*, Linz (Austria), November 13, 2016.

C14 **Roccon, A.**[†], Zonta, F. and Soldati A., (2016) Coalescence and break-up of large, deformable droplets with different viscosities in turbulent channel flow. *International Conference on Multiphase Flow*, Florence (Italy), May 22-27, 2016.

C15 **Roccon, A.**[‡], Zonta, F. and Soldati A., (2016) Coalescence and break-up of droplets, Poster Session, *International Conference on Multiphase Flow*, Florence (Italy), May 22-27, 2016.

C16 **Roccon, A.**[‡], Zonta, F. and Soldati A., (2016) Coalescence and break-up of droplets, Poster Session, *PRACE Days 2016*, Prague (Czech Republic), May 10-12, 2016.

C17 **Roccon, A.**[†], Zonta, F. and Soldati A., (2015) Coalescence and break-up of large, deformable droplets with different viscosities in turbulent channel flow, *Ercoftac Meeting*, Ljubljana (Slovenia), November 13, 2016.

[†] Presentation speaker. [‡] Poster speaker.

A.3 HPC projects

P1 **Viscosity-modulated breakup and coalescence of large drops in bounded turbulence**, Project ID: DD VIMODETU, Vesta, Argonne National Laboratory, Chicago (USA), 2017.

P2 **Viscosity stratified fluids in turbulent channel flow**, Project ID: 71026, VSC3 (Tier 0), Vienna (Austria), 2017.

P3 **VIscosity STRAtified Fluids in TUrbulent channel flow - VISTRATU**, Project ID: ISCRA B HP10BCFP82, CINECA Supercomputing Centre, Marconi (Tier 0), Bologna (Italy), 2017.

P4 **INfluence of VIscosity on the dinamics of DEformable droplets in TUrbulence - INVIDETU**, Project ID: ISCRA B HP10B9TXF1, CINECA Supercomputing Centre, Marconi (Tier 0), Bologna (Italy), 2016.

P5 **SPInodal DEcomposition in multiphase flows with large viscosity Ratio - SPIDER**, Project ID: ISCRA C HP10CFQYYH, CINECA Supercomputing Centre, Fermi (Tier 0), Bologna (Italy), 2015.

A.4 Advanced courses

A1 **Argonne Training Program On Extreme-Scale Computing**, Q-Center, Chicago (IL,USA), August, 2017.

A2 **Introduction to OpenMP**, TU Wien (Austria), June, 2017.

A3 **Introduction to MPI**, TU Wien (Austria), May, 2017.

A4 **Wall-Bounded Turbulence**, International Centre for Mechanical Sciences (CISM), Udine (Italy), July, 2016. Coordinated by: Prof. S. Pirozzoli.

A5 **Small Scale Modeling and Simulation of Turbulent Multiphase Flows**, International Centre for Mechanical Sciences (CISM), Udine (Italy), July, 2015. Coordinated by: Prof. S. Vincent and Prof. J. L. Estivalezes.

A6 **Mixing and Dispersion in Flows Dominated by Rotation and Buoyancy**, International Centre for Mechanical Sciences (CISM), Udine (Italy), July, 2015. Coordinated by: Prof. H. Clercx and Prof. G. J. van Heijst.

A7 **Dynamic of Bubbly flows**, International Centre for Mechanical Sciences (CISM), Udine (Italy), June, 2015. Coordinated by: Prof. F. Risso and Prof. C. Sun.

A8 **Advanced CFD techniques for turbulent flows: theory and applications**, Universiyt of Udine, Udine (Italy), May, 2015. Coordinated by: Prof. U. Piomelli (Queen's University, Canada).

Bibliography

[1] S. Adami, X.Y. Hu, and N.A. Adams. A conservative sph method for surfactant dynamics. *J. Comput. Phys.*, 229(5):1909–1926, 2010.

[2] A.W. Adamson and A.P. Gast. *Physical chemistry of surfaces.* Interscience publishers New York, 1967.

[3] S. Ahmadi, A. Roccon, F. Zonta, and A. Soldati. Turbulent drag reduction in channel flow with viscosity stratified fluids. *Comput. Fluids*, 2016.

[4] A. Alke and D. Bothe. 3D numerical modeling of soluble surfactant at fluidic interfaces based on the volume-of-fluid method. *Fluid Dyn. Mater. Process*, 5, 2009.

[5] D.M. Anderson, G.B. McFadden, and A.A. Wheeler. Diffuse interface methods in fluid mechanics. *Annu. Rev. Fluid Mech.*, 30(1):139–165, 1998.

[6] R. Andersson and B. Andersson. On the breakup of fluid particles in turbulent flows. *AIChE J.*, 52(6):2020–2030, 2006.

[7] K. Arai, M. Konno, Y. Matunaga, and S. Saito. Effect of dispersed-phase viscosity on maximum stable drop size for breakup in turbulent-flow. *J. Chem. Eng. Jpn.*, 10(4):325–330, 1977.

[8] U.M. Ascher, S.J. Ruuth, and B.T.R. Wetton. Implicit-explicit methods for time-dependent partial differential equations. *SIAM J. Numer. Anal.*, 32(3):797–823, 1995.

[9] N. Ashgriz and J.Y. Poo. Coalescence and separation in binary collisions of liquid drops. *J. Fluid Mech.*, 221:183, 1990.

[10] V.E. Badalassi, H.D. Ceniceros, and S. Banerjee. Computation of multiphase systems with phase field models. *J. Comput. Phys.*, 190(2):371–397, 2003.

[11] V.E. Badalassi, H.D. Ceniceros, and S. Banerjee. Computation of multiphase systems with phase field models. *J. Comput. Phys*, 190(2):371–397, 2003.

[12] R. Bai, K. Chen, and D.D. Joseph. Lubricated pipelining: stability of core—annular flow. part 5. experiments and comparison with theory. *J. Fluid Mech.*, 240:97–132, 1992.

[13] G.K. Batchelor. *An Introduction to Fluid Dynamics.* Cambridge University Press, 2000.

[14] M. Bayareh and S. Mortazavi. Binary collision of drops in simple shear flow at finite reynolds numbers: Geometry and viscosity ratio effects. *Adv. in Eng. Softw.*, 42(8):604–611, 2011.

[15] M. Bayareh and S. Mortazavi. Binary collision of drops in simple shear flow at finite reynolds numbers: Geometry and viscosity ratio effects. *Advances in Engineering Software*, 42(8):604–611, 2011.

[16] I. B Bazhlekov, P.D. Anderson, and H.E. Meijer. Numerical investigation of the effect of insoluble surfactants on drop deformation and breakup in simple shear flow. *Journal of colloid and interface science*, 298(1):369–394, 2006.

[17] W. Bo and J.W. Grove. A volume of fluid method based ghost fluid method for compressible multi-fluid flows. *Comput. Fluids*, 90:113–122, 2014.

[18] M.R. Booty and M. Siegel. A hybrid numerical method for interfacial fluid flow with soluble surfactant. *J. Comp. Physics*, 229(10):3864–3883, 2010.

[19] J. P. Boyd. *Chebyshev and Fourier spectral methods.* Courier Dover Publications, 2001.

[20] J.U. Brackbill, D.B. Kothe, and C. Zemach. A continuum method for modeling surface tension. *J. Comput. Phys.*, 335354, 1992.

[21] C. Brücker. Evidence of rare backflow and skin-friction critical points in near-wall turbulence using micropillar imaging. *Phys. Fluids*, 27(3):031705, 2015.

[22] B. Bunner. Direct numerical simulations of three-dimensional bubbly flows. *Phys. Fluids*, 11(8), 1999.

[23] J.W. Cahn and J.E. Hilliard. Free Energy of a Nonuniform System. i. Interfacial Free Energy. *J. Chem. Phys*, 28:258–267, 1958.

[24] J.W. Cahn and J.E. Hilliard. Free energy of a nonuniform system. ii. thermodynamic basis. *J. Chem. Phys*, 30(5):1121–1124, 1959.

[25] J.W. Cahn and J.E. Hilliard. Free energy of a nonuniform system. iii. nucleation in a two-component incompressible fluid. *J. Chem. Phys*, 31:688, 1959.

[26] R.V. Calabrese, T.P.K. Chang, and P.T. Dang. Drop breakup in turbulent stirred-tank contactors. Part I: Effect of dispersed-phase viscosity. *AIChE J.*, 32(4):657–666, 1986.

[27] H.D. Ceniceros. The effects of surfactants on the formation and evolution of capillary waves. *Phys. Fluids*, 15(1):245–256, 2003.

[28] C. Chang and E. Franses. Adsorption dynamics of surfactants at the air/water interface: a critical review of mathematical models, data, and mechanisms. *Colloids and Surfaces A: Physicochemical and Engineering Aspects*, 100:1–45, 1995.

[29] L. Changzhi and G. Liejin. Experimental study of drop deformation and breakup in simple shear flows. *Chin. J. Chem. Eng.*, 15(1):1–5, 2007.

[30] F. Charru and E.J. Hinch. Phase diagram of interfacial instabilities in a two-layer couette flow and mechanism of the long-wave instability. *J. Fluid Mech.*, 414:195–223, 2000.

[31] H.T. Chen and S. Middleman. Drop size distribution in agitated liquid-liquid systems. *AIChE J.*, 13(5):989–995, 1967.

[32] K. Chen, R. Bai, and D.D. Joseph. Lubricated pipelining. Part 3 Stability of core-annular flow in vertical pipes. *J. Fluid Mech.*, 214:251–286, 1990.

[33] K. Chen, R. Bai, and D.D. Joseph. Lubricated pipelining. part 3 stability of core-annular flow in vertical pipes. *J. Fluid Mech.*, 214:251–286, 1990.

[34] A.K. Chesters. The modelling of coalescence processes in fluid-liquid dispersions: a review of current understanding. *Chemical engineering research & design*, 69(A4):259–270, 1991.

[35] P.H. Clay. The Mechanism of emulsion formation in turbulent flow Part I. *Proc.R.Acad.Sci*, 43, 1940.

[36] P.H. Clay. The Mechanism of emulsion formation in turbulent flow Part II. *Proc.R.Acad.Sci*, 43, 1940.

[37] R.D. Cohen. Brief communication. *Int. J. Multiph. Flow*, 20(1):211–216, 1994.

[38] S.B. Collins and J.G. Knudsen. Drop-size distributions produced by turbulent pipe flow of immiscible liquids. *AIChE J.*, 16(6):1072–1080, 1970.

[39] R.G. Cox. The deformation of a drop in a general time-dependent fluid flow. *J. Fluid Mech.*, 37(3):601–623, 1969.

[40] B. Dai and L.G. Leal. The mechanism of surfactant effects on drop coalescence. *Phys. Fluids*, 20(4):040802, 2008.

[41] P.K. Das. Prediction of maximum stable diameter of viscous drops in a turbulent dispersion. *Chem. Eng. Technol.*, 19(1):39–42, 1996.

[42] R.H. Davis, J.A Schonberg, and J.M. Rallison. The lubrication force between two viscous drops. *Phys. Fluids*, 1(1):77–81, 1989.

[43] P. De Bruyn, R. Cardinaels, and P. Moldenaers. The effect of geometrical confinement on coalescence efficiency of droplet pairs in shear flow. *Journal of colloid and interface science*, 409:183–192, 2013.

[44] K.H. De Haas, C. Blom, D. Van den Ende, M.H.G. Duits, and J. Mellema. Deformation of giant lipid bilayer vesicles in shear flow. *Phys. Rev. E*, 56(6):7132, 1997.

[45] W.C. de Jesus, A.M. Roma, M.R. Pivello, M.M. Villar, and A. da Silveira-Neto. A 3D front-tracking approach for simulation of a two-phase fluid with insoluble surfactant. *J. Comput. Phys.*, 281:403–420, 2015.

[46] J.J. Derksen and H.E.A. Van Den Akker. Multi-scale simulations of stirred liquid-liquid dispersions. *Chem. Eng. Res. Des.*, 85(5):697–702, 2007.

[47] O. Desjardins, V. Moureau, and H. Pitsch. An accurate conservative level set / ghost fluid method for simulating turbulent atomization. *J. Comput. Phys.*, 227:8395–8416, 2008.

[48] E. Dickinson. Hydrocolloids as emulsifiers and emulsion stabilizers. *Food hydrocolloids*, 23(6):1473–1482, 2009.

[49] M.S. Dodd and A. Ferrante. On the interaction of Taylor length scale size droplets and isotropic turbulence. *J. Fluid Mech.*, 806:356–412, 2016.

[50] M.A. Drumright-Clarke and Y. Renardy. The effect of insoluble surfactant at dilute concentration on drop breakup under shear with inertia. *Phys. Fluids*, 16(1):14–21, 2004.

[51] C.D. Eastwood, L. Armi, and J.C. Lasheras. The breakup of immiscible fluids in turbulent flows. *J. Fluid Mech.*, 502:309–333, 2004.

[52] S. Engblom, M. Do-Quang, G. Amberg, and A.K. Tornberg. On diffuse interface modeling and simulation of surfactants in two-phase fluid flow. *Communications in Comp. Physics*, 14(4):879–915, 2013.

[53] C.A. Escalante-Velázquez, M.A. Huesca-Reyes, I.Y. Rosas, and E. Geffroy. Drop deformation in two-roll mills considering wall effects. *Journal of Physics: Conference Series*, 582(1):012014, 2015.

[54] H. Farhat, F. Celiker, T. Singh, and J.S. Lee. A hybrid lattice boltzmann model for surfactant-covered droplets. *Soft Matter*, 7(5):1968–1985, 2011.

[55] R.P. Fedkiw, T. Aslam, Merriman B., and S. Osher. A non-oscillatory eulerian approach to interfaces in multimaterial flows (the ghost fluid method). *J. Comput. Phys.*, 152(2):457–492, 1999.

[56] G. Finotello, T. P. Johan, Niels G. Deen, Alfred Jongsma, Fredrik Innings, and J. A. M. Kuipers. Effect of viscosity on droplet-droplet collisional interaction. *Phys. Fluids*, 29(6):067102, 2017.

[57] C. Focke and D. Bothe. Direct numerical simulation of binary off-center collisions of shear thinning droplets at high weber numbers. *Phis. Fluids*, 24:1–19, 2012.

[58] S. Frijters, F. Günther, and J. Harting. Effects of nanoparticles and surfactant on droplets in shear flow. *Soft Matter*, 8(24):6542–6556, 2012.

[59] F. Gibou and R. Fedkiw. A Second Order Accurate Symmetric Discretization of the Poisson Equation on Irregular Domains. *J. Sci. Comput*, pages 1–35, 2001.

[60] R. Govindarajan and K.C. Sahu. Instabilities in viscosity-stratified flow. *Annu. Rev. Fluid Mech.*, 46:331–353, 2014.

[61] S. Grosse and W. Schröder. Wall-shear stress patterns of coherent structures in turbulent duct flow. *J. Fluid Mech.*, 633:147–158, 2009.

[62] S. Gu, H. Zhang, and Z. Zhang. An energy-stable finite-difference scheme for the binary fluid-surfactant system. *J. Comp. Physics*, 270:416–431, 2014.

[63] D. Gueyffier, J. Li, A. Nadim, R. Scardovelli, and S. Zaleski. Volume-of-fluid interface tracking with smoothed surface stress methods for three-dimensional flows. *J. Comput. Phys.*, 152(2):423–456, 1999.

[64] S. Guido and F. Greco. Dynamics of a liquid drop in a flowing immiscible liquid. *Rheology Reviews*, 99:99–142, 2004.

[65] S. Guido and M. Simeone. Binary collision of drops in simple shear flow by computer-assisted video optical microscopy. *J. Fluid Mech.*, 357:1–20, 1998.

[66] R. Gunn. Collision characteristics of freely falling water drops. *Science*, 150(3697):695–701, 1965.

[67] A.K. Gunstensen, D.H. Rothman, S. Zaleski, and G. Zanetti. Lattice boltzmann model of immiscible fluids. *Phys. Rev. A*, 43(8):4320, 1991.

[68] E.J. Hinch. A note on the mechanism of the instability at the interface between two shearing fluids. *J. Fluid Mech.*, 144:463–465, 1984.

[69] J.O. Hinze. Fundamentals of the hydrodynamic mechanism of splitting in dispersion processes. *AIChE J.*, 1(3):289–295, 1955.

[70] C.W. Hirt and B.D. Nichols. Volume of fluid (vof) method for the dynamics of free boundaries. *J. Comput. Phys.*, 39(1):201–225, 1981.

[71] W.J. Howarth. Coalescence of drops in a turbulent flow field. *Chem. Eng. Sci.*, 19(1):33 – 38, 1964.

[72] L.P. Hsiang and G.M. Faeth. Near-limit drop deformation and secondary breakup. *Int. J. Multiph. Flow*, 18(5):635–652, 1992.

[73] H.H. Hu, T.S. Lundgren, and D.D. Joseph. Stability of core-annular flow with a small viscosity ratio. *Phys. Fluids.*, 2(11):1945–1954, 1990.

[74] Y.T. Hu and A. Lips. Estimating surfactant surface coverage and decomposing its effect on drop deformation. *Phys. Rev. Lett.*, 91(4):044501, 2003.

[75] Y.T. Hu, D.J. Pine, and L.G. Leal. Drop deformation, breakup, and coalescence with compatibilizer. *Phys. Fluids*, 12(3):484–489, 2000.

[76] Z. Hu, C.L. Morfey, and N.D. Sandham. Wall pressure and shear stress spectra from direct simulations of channel flow. *AIAA J.*, 44(7):1541–1549, 2006.

[77] J.C.R. Hunt, A.A. Wray, and P. Moin. Eddies, streams, and convergence zones in turbulent flows. In *Studying Turbulence Using Numerical Simulation Databases, 2*, volume 1, pages 193–208, 1988.

[78] M. Huo, S. Lin, H. Liu, and F.L. Chia-fon. Study on the spray and combustion characteristics of water–emulsified diesel. *Fuel*, 123:218–229, 2014.

[79] D. Jacqmin. Calculation of two-phase navier–stokes flows using phase-field modeling. *J. Comput. Phys.*, 155(1):96–127, 1999.

[80] A.J. James and J. Lowengrub. A surfactant-conserving volume-of-fluid method for interfacial flows with insoluble surfactant. *J. Comput. Phys.*, 201(2):685–722, 2004.

[81] D. Jamet, D. Torres, and J. U. Brackbill. On the theory and computation of surface tension: the elimination of parasitic currents through energy conservation in the second-gradient method. *J. Comput. Phys.*, 182(1):262–276, 2002.

[82] D.D. Joseph, M. Renardy, and Y. Renardy. Instability of the flow of two immiscible liquids with different viscosities in a pipe. *J. Fluid Mech.*, 141:309–317, 1984.

[83] D.D. Joseph, M. Renardy, and Y. Renardy. Instability of the flow of two immiscible liquids with different viscosities in a pipe. *J. Fluid Mech.*, 141:309–317, 1984.

[84] T. Kadota and H. Yamasaki. Recent advances in the combustion of water fuel emulsion. *Progress in energy and combustion science*, 28(5):385–404, 2002.

[85] M. Kang. A Boundary Condition Capturing Method for Multiphase Incompressible Flow. *J. Sci. Comput*, 2000.

[86] V.V. Khatavkar, P.D. Anderson, and H.E.H. Meijer. On scaling of diffuse–interface models. *Chem. Eng. Sci.*, 61(8):2364–2378, 2006.

[87] S. Khatri and A.K. Tornberg. A numerical method for two phase flows with insoluble surfactants. *Comput. Fluids*, 49(1):150–165, 2011.

[88] D. Kiefhaber, C.J. Zappa, and B. Jähne. Influence of natural surfactants on short wind waves in the coastal peruvian waters. *Ocean Sci.*, 12(4):1291–1325, 2015.

[89] H. Kim and D.J. Burgess. Prediction of interfacial tension between oil mixtures and water. *J. Colloid Interface Sci.*, 241(2):509–513, 2001.

[90] J. Kim. A continuous surface tension force formulation for diffuse-interface models. *J. Comput. Phys*, 204(2):784–804, 2005.

[91] J. Kim. Phase-Field Models for Multi-Component Fluid Flows. *Commun. Comput. Phys.*, 12(3):613–661, 2012.

[92] J. Kim, P. Moin, and R. Moser. Turbulence statistics in fully developed channel flow at low reynolds number. *J. Fluid Mech.*, 177(1):133–166, 1987.

[93] A.E. Komrakova, D. Eskin, and J.J. Derksen. Numerical study of turbulent liquid-liquid dispersions. *AIChE J.*, 61(8):2618–2633, 2015.

[94] S. Komura and H. Kodama. Two order parameter model for an oil-water-surfactant system. *Phys. Rev. E*, 55(2):1722–1727, 1997.

[95] D.J. Korteweg. Sur la forme que prennent les ´equations du mouvements des fluides si l'on tient compte des forces capillaires caus´ees par des variations de densit´e consid´erables mais continues et sur la th´eorie de la capillarit´e dans l'hypoth‘ese d'une variation continue de la densite. *Archives Neerlandaises des Sciences Exactes et Naturelles*, 6:1–24, 1901.

[96] C. Kouris and J. Tsamopoulos. Dynamics of axisymmetric core-annular flow in a straight tube. i. the more viscous fluid in the core, bamboo waves. *Phys. Fluids*, 13(4):841–858, 2001.

[97] H.P. Kreplin and H. Eckelmann. Behavior of the three fluctuating velocity components in the wall region of a turbulent channel flow. *Phys. Fluids*, 22(7):1233–1239, 1979.

[98] N. Kurata, K. Vella, B. Hamilton, M. Shivji, A. Soloviev, S. Matt, A. Tartar, and W. Perrie. Surfactant-associated bacteria in the near-surface layer of the ocean. *Sci. Rep.*, 6:19123, 2016.

[99] M.C. Lai, Y.H. Tseng, and H. Huang. An immersed boundary method for interfacial flows with insoluble surfactant. *J. Comput. Phys.*, 227(15):7279–7293, 2008.

[100] M.C. Lai, Y.H. Tseng, H. Huang, et al. Numerical simulation of moving contact lines with surfactant by immersed boundary method. *Commun. Comput. Phys.*, 8(4):735, 2010.

[101] B. Lalanne, L. R. Villegas, S. Tanguy, and F. Risso. On the computation of viscous terms for incompressible two-phase flows with Level Set / Ghost Fluid Method. *J. Comput. Phys.*, 301:289–307, 2015.

[102] A.G. Lamorgese and R. Mauri. Diffuse-interface modeling of phase segregation in liquid mixtures. *Int. J. Multiph. Flow*, 34(10):987–995, 2008.

[103] A.G. Lamorgese, D. Molin, and R. Mauri. Phase field approach to multiphase flow modeling. *Milan J. Math.*, 79(2):597–642, 2011.

[104] M. Laradji, H. Guo, M. Grant, and M. J. Zuckermann. The effect of surfactants on the dynamics of phase separation. *J. Phys. Condens. Matter*, 6715(32), 1991.

[105] L.G. Leal. Flow induced coalescence of drops in a viscous fluid. *Phys. Fluids*, 16(6):1833–1851, 2004.

[106] A. Lee, A. Münch, and E. Süli. Sharp-interface limits of the cahn-hilliard equation with degenerate mobility. *SIAM J. Appl. Math.*, 76(2):433–456, 2016.

[107] P. Lenaers, Q. Li, G. Brethouwer, P. Schlatter, and R. Örlü. Rare backflow and extreme wall-normal velocity fluctuations in near-wall turbulence. *Phys. Fluids*, 24(3):035110, 2012.

[108] V.G. Levich and R.J. Seeger. Physicochemical hydrodynamics. *Am. J. Phys.*, 31(11):892–892, 1963.

[109] R. Levy, D. Uminsky, A. Park, and J. Calambokidis. A theory for the hydrodynamic origin of whale flukeprints. *Int. J. Non Linear Mech.*, 46(4):616–626, 2011.

[110] J. Li and Y. Renardy. Direct simulation of unsteady axisymmetric core–annular flow with high viscosity ratio. *J. Fluid Mech.*, 391:123–149, 1999.

[111] J. Li, Y.Y. Renardy, and M. Renardy. Numerical simulation of breakup of a viscous drop in simple shear flow through a volume-of-fluid method. *Phys. Fluids*, 12(2):269–282, 2000.

[112] Y. Li and J. Kim. A comparison study of phase-field models for an immiscible binary mixture with surfactant. *Eur. J. Phys. B.*, 2012.

[113] T. G. Liu, B. C. Khoo, and C. W. Wang. The ghost fluid method for compressible gas-water simulation. *J. Comput. Phys.*, 204:193–221, 2005.

[114] M. Loewenberg and E.J. Hinch. Collision of two deformable drops in shear flow. *J. Fluid Mech.*, 338:299–315, 1997.

[115] M. Loewenberg and E.J. Hinch. Collision of two deformable drops in shear flow. *J. Fluid Mech.*, 338:299–315, 1997.

[116] J. Lowengrub and L. Truskinovsky. Quasi–incompressible cahn–hilliard fluids and topological transitions. *Proc. Royal Soc. A*, 454(1978):2617–2654, 1998.

[117] J. Lu, M. Muradoglu, and G. Tryggvason. Effect of insoluble surfactant on turbulent bubbly flows in vertical channels. *Int. J. Multiph. Flow*, 95:135–143, 2017.

[118] J. Lu, M. Muradoglu, and G. Tryggvason. Effect of insoluble surfactant on turbulent bubbly flows in vertical channels. *Int. J. Multiph. Flow*, 95:135–143, 2017.

[119] J. Lu and G. Tryggvason. Effect of bubble deformability in turbulent bubbly upflow in a vertical channel. *Phys. Fluids*, 20(4), 2008.

[120] F. Magaletti, F. Picano, M. Chinappi, L. Marino, and C.M. Casciola. The sharp-interface limit of the Cahn–Hilliard/Navier–Stokes model for binary fluids. *J. Fluid Mech.*, 714:95–126, 2013.

[121] G Marrucci. A theory of coalescence. *Chem. Eng. Sci.*, 24(6):975–985, 1969.

[122] T. Menard, S. Tanguy, and A. Berlemont. Coupling level set / VOF / ghost fluid methods : Validation and application to 3D simulation of the primary break-up of a liquid jet. *Int. J. Multiph. Flow*, 33:510–524, 2007.

[123] P. Moin and K. Mahesh. Direct numerical simulation: a tool in turbulence research. *Annu. Rev. Fluid Mech.*, 30(1):539–578, 1998.

[124] M. Muradoglu and G. Tryggvason. A front-tracking method for computation of interfacial flows with soluble surfactants. *J. Comput. Phys.*, 227:2238–2262, 2008.

[125] M. Muradoglu and G. Tryggvason. Simulations of soluble surfactants in 3d multiphase flow. *J. Comput. Phys.*, 274:737–757, 2014.

[126] R. Nagarajan. Amphiphilic surfactants and amphiphilic polymers: principles of molecular assembly. In *Amphiphiles: Molecular Assembly and Applications*, pages 1–22. ACS Publications, 2011.

[127] E. Olsson and G. Kreiss. A conservative level set method for two phase flow. *J. Comput. Phys.*, 210(1):225–246, 2005.

[128] S. Osher and J. Sethian. Fronts Propagating with Curvature-Dependent Speed:Algorithms Based on Hamilton-Jacobi Formulations. *J. Comput. Phys.*, 49:12–49, 1988.

[129] S. Osher and J. Sethian. A Level Set Approach for computing solutions to incompressible Two-Phase Flow. *J. Comput. Phys.*, 114:12–49, 1994.

[130] K.L. Pan, Y.H. Tseng, J.C. Chen, K.L. Huang, C.H. Wang, and M.C. Lai. Controlling droplet bouncing and coalescence with surfactant. *J. Fluid Mech.*, 799:603–636, 2016.

[131] A. Patel, B.J. Boersma, and R. Pecnik. The influence of near-wall density and viscosity gradients on turbulence in channel flows. *J. Fluid Mech.*, 809:793–820, 2016.

[132] A. Patel, J.W.R. Peeters, B.J. Boersma, and R. Pecnik. Semi-local scaling and turbulence modulation in variable property turbulent channel flows. *Phys. Fluids*, 27(9):095101, 2015.

[133] J.D. Paulsen, R.K. Carmigniani, A. Kanman, J.C. Burton, and S.R. Nagel. Coalescence of bubbles and drops in an outer fluid. *Nat. Commun.*, 5:3182, 2014.

[134] R. Pecnik and A. Patel. Scaling and modelling of turbulence in variable property channel flows. *J. Fluid Mech.*, 823, 2017.

[135] P. Perlekar, L. Biferale, and M. Sbragaglia. Droplet size distribution in homogeneous isotropic turbulence. *Phys. Fluids*, 065101:1–10, 2012.

[136] S Popinet. Numerical models of surface tension. *Annu. Rev. Fluid Mech.*, 50:1–28, 2018.

[137] C. Pozrikidis. *Introduction to theoretical and computational fluid dynamics.* Oxford university press, 2011.

[138] A. Prosperetti and G. Tryggvason. *Computational Methods for Multiphase Flow.* Cambridge Press, 2009.

[139] D. Qian, J. B. McLaughlin, K. Sankaranarayanan, S. Sundaresan, and K. Kontomaris. Simulation of bubble breakup dynamics in homogeneous turbulence. *Chem. Eng. Commun.*, 193(8):1038–1063, 2006.

[140] J. Qian and C.K. Law. Regimes of coalescence and separation in droplet collision. *J. Fluid Mech.*, 331:59–80, 1997.

[141] Y. Renardy, M. Renardy, and V. Cristini. A new volume-of-fluid formulation for surfactants and simulations of drop deformation under shear at a low viscosity ratio. *Eur. J. Mech. B-Fluid*, 21(1):49–59, 2002.

[142] A. Roccon, M. De Paoli, F. Zonta, and A. Soldati. Viscosity-modulated breakup and coalescence of large drops in bounded turbulence. *Phys. Rev. Fluids*, 2, 2017.

[143] A. Rutherford. *Vectors, Tensors and the Basic Equations of Fluid Mechanics.* Dover Publications, 1989.

[144] M.D. Saroka, N. Ashgriz, and M. Movassat. Numerical investigation of head-on bynary drop collisions in a dynamically inert environment. *J. Appl. Fluid Mech.*, 5:23–37, 2012.

[145] L. Scarbolo, F. Bianco, and A. Soldati. Coalescence and breakup of large droplets in turbulent channel flow. *Phys. Fluids*, 27(7):073302, 2015.

[146] L. Scarbolo, F. Bianco, and A. Soldati. Turbulence modification by dispersion of large deformable droplets. *Eur. J. Mech. B-Fluid*, 55:294–299, 2016.

[147] R. Scardovelli and S. Zaleski. Direct numerical simulation of free-surface and interfacial flow. *Ann. Rev. Fluid Mech.*, pages 567–603, 1999.

[148] R. Scardovelli and S. Zaleski. Direct numerical simulation of free-surface and interfacial flow. *Annu. Rev. Fluid Mech.*, 31(1):567–603, 1999.

[149] J.A. Sethian and P. Smereka. Level set methods for fluid interfaces. *Ann. Rev. Fluid Mech.*, 35(1):341–372, 2003.

[150] J. Shaikh, R. Bhardwaj, and A. Sharma. A Ghost Fluid Method based Sharp Interface Level Set Method for Evaporating Droplet. *Procedia IUTAM*, 15:124–131, 2015.

[151] M. Shapira and S. Haber. Low reynolds number motion of a droplet in shear flow including wall effects. *Int. J. Multiphase Flow*, 16(2):305–321, 1990.

[152] O. Shardt, J.J. Derksen, and S. K. Mitra. Simulations of droplet coalescence in simple shear flow. *Langmuir*, 29(21):6201–6212, 2013.

[153] S. Shen and X. Yang. Decoupled energy stable schemes for phase-field models of two-phase complex fluids. *SIAM J. Sci. Comput.*, 36(1):B122–B145, 2014.

[154] R. Shinnar. On the behaviour of liquid dispersions in mixing vessels. *J. Fluid Mech.*, 10(02):259, 1961.

[155] V. Sibillo, G. Pasquariello, M. Simeone, V. Cristini, and S. Guido. Drop deformation in microconfined shear flow. *Phys. Rev. Lett.*, 97(5):054502, 2006.

[156] R.K. Singh and K. Sarkar. Effects of viscosity ratio and three dimensional positioning on hydrodynamic interactions between two viscous drops in a shear flow at finite inertia. *Phys. Fluids*, 21(10):103303, 2009.

[157] R. Skartlien, E. Sollum, and H. Schumann. Droplet size distributions in turbulent emulsions: Breakup criteria and surfactant effects from direct numerical simulations. *J. Chem. Phys.*, 139(17), 2013.

[158] C.A. Sleicher. Maximum stable drop size in turbulent flow. *AIChE J.*, 8(4):471–477, 1962.

[159] H.A. Stone. Dynamics of drop deformation and breakup in viscous fluids. *Annu. Rev. Fluid Mech.*, 26(1):65–102, 1994.

[160] H.A. Stone. A simple derivation of the time dependent convective diffusion equation for surfactant transport along a deforming interface. *Phys. Fluids*, 111(1990):2–4, 2007.

[161] H.A. Stone and L.G. Leal. The effects of surfactants on drop deformation and breakup. *J. Fluid Mech.*, 220:161–186, 1990.

[162] Y. Sun and C. Beckermann. Sharp interface tracking using the phase-field equation. *J. Comput. Phys.*, 220(2):626–653, 2007.

[163] N. Takada, A. Tomiyama, and S. Hosokawa. Lattice boltzmann simulation of drops in a shear flow. *Proc. 4th ASME/JSME joint fluids engineering conference*, 2003.

[164] S. Takagi and Y. Matsumoto. Surfactant effects on bubble motion and bubbly flows. *Ann. Rev. Fluid Mech.*, 43:615–636, 2011.

[165] S. Takagi, T. Ogasawara, and Y. Matsumoto. The effects of surfactant on the multiscale structure of bubbly flows. *Philos. Trans. A. Math. Phys. Eng. Sci.*, 366(1873):2117–2129, 2008.

[166] S. Tangui, T. Menard, and A. Berlemont. A Level Set Method for vaporizing two-phase flows. *J. Comput. Phys.*, 221:837–853, 2007.

[167] G.I. Taylor. The formation of emulsions in definable fields of flows. *Proc. Royal Soc. A*, 146:501–523, 1934.

[168] K.E. Teigen, P. Song, J. Lowengrub, and A. Voigt. A diffuse-interface method for two-phase flows with soluble surfactants. *J. Comp. Physics*, 230(2):375–393, 2011.

[169] P. Than, L. Preziosi, D.D. Joseph, and M. Arney. Measurement of interfacial tension between immiscible liquids with the spinning road tensiometer. *J. Colloid Interface Sci.*, 124(2):552–559, 1988.

[170] E.F. Toro. *Godunov Methods, Theory and applications.* Springer Science, 2001.

[171] G.I. Tóth and B. Kvamme. Analysis of ginzburg-landau-type models of surfactant-assisted liquid phase separation. *Phys. Rev. E*, 91(3):032404, 2015.

[172] D.C. Tretheway and L.G. Leal. Surfactant and viscoelastic effects on drop deformation in 2-d extensional flow. *AIChE J.*, 45(5):929–937, 1999.

[173] G. Tryggvason, B. Bunner, A. Esmaeeli, D. Juric, W. Tauber, J. Han, S. Nas, and Y. Jan. A front-tracking method for the computations of multiphase flow. *J. Comput. Phys.*, 759:708–759, 2001.

[174] S. Unverdi and G. Trygvasson. A Front-Tracking Method for Viscous , Incompressible , Multi-fluid Flows. *J. Comput. Phys.*, 1992.

[175] E. Uzgoren, J. Sim, and W. Shyy. Marker-based, 3-d adaptive cartesian grid method for multiphase flow around irregular geometries. *Commun. Comput. Phys*, 2008.

[176] R.G.M. Van Der Sman and S. Van Der Graaf. Diffuse interface model of surfactant adsorption onto flat and droplet interfaces. *Rheol. Acta*, 46(1):3–11, 2006.

[177] P.M. Vlahovska, J. Blawzdziewicz, and M. Loewenberg. Small-deformation theory for a surfactant-covered drop in linear flows. *J. Fluid Mech.*, 624:293–337, 2009.

[178] G.A. Voth and A. Soldati. Anisotropic particles in turbulence. *Annu. Rev. Fluid Mech.*, 49(1):249–276, 2017.

[179] C.Y. Wang and R.V. Calabrese. Drop breakup in turbulent stirred-tank contactors. Part II: Relative influence of viscosity and interfacial tension. *AIChE J.*, 32(4):667–676, 1986.

[180] C.Y. Wang, R.V. Calabrese, and N.P. Bryner. Drop breakup in turbulent stirred-tank contactors. Part III: Correlations for mean size and drop size distribution. *AIChE J.*, 32(4):667–676, 1986.

[181] C.Y. Wang, C.B. Zhang, X.Y. Huang, X.D. Liu, and Y.P. Chen. Hydrodynamics of passing-over motion during binary droplet collision in shear flow. *Chin. Phys. B*, 25(10):108202, 2016.

[182] C.E. Weatherburn. *Differential geometry of three dimensions*, volume 1. Cambridge University Press, 2016.

[183] A. Wietrzak and R.M. Lueptow. Wall shear stress and velocity in a turbulent axisymmetric boundary layer. *J. Fluid Mech.*, 259:191–218, 1994.

[184] J. Wu, J. Lu, C. Wilson, Y. Lin, and H. Lu. Effective liquid-liquid extraction method for analysis of pyrethroid and phenylpyrazole pesticides in emulsion-prone surface water samples. *J. Chromatogr. A*, 1217(41):6327–6333, 2010.

[185] F. Xie, X. Zheng, M.S. Triantafyllou, Y. Constantinides, Y. Zheng, and G. Em Karniadakis. Direct numerical simulations of two-phase flow in an inclined pipe. *J. Fluid Mech.*, 825:189–207, 2017.

[186] J.J. Xu. A level-set method for interfacial flows with surfactant. *J. Comput. Phys.*, 212:590–616, 2006.

[187] J.J. Xu, Z. Li, J. Lowengrub, and H. Zhao. Numerical study of surfactant-laden drop-drop interactions. *Comm. Comp. Phys.*, 10(2):453–473, 2011.

[188] J.J. Xu and W. Ren. A level-set method for two-phase flows with moving contact line and insoluble surfactant. *J. Comput. Phys.*, 263:71–90, 2014.

[189] J.J. Xu, Y. Yang, and J. Lowengrub. A level-set continuum method for two-phase flows with insoluble surfactant. *J. Comput. Phys.*, 231(17):5897–5909, 2012.

[190] J.J. Xu and H.K. Zhao. An eulerian formulation for solving partial differential equations along a moving interface. *SIAM J. Sci. Comput.*, 19(1):573–594, 2003.

[191] X. Yang. *An arbitrary Lagrangian-Eulerian method for interfacial flows with insoluble surfactants.* University of Minnesota, 2007.

[192] Y.N. Young, M.R. Booty, M. Siegel, and J. Li. Influence of surfactant solubility on the deformation and breakup of a bubble or capillary jet in a viscous fluid. *Phys. Fluids*, 21(7):072105, 2009.

[193] P. Yue, J.J. Feng, C. Liu, and J. Shen. A diffuse-interface method for simulating two-phase flows of complex fluids. *J. Fluid Mech.*, 515(1):293–317, 2004.

[194] P. Yue, J.J. Feng, C. Liu, and J. Shen. Diffuse-interface simulations of drop coalescence and retraction in viscoelastic fluids. *J. Nonnewton. Fluid Mech.*, 129(3):163–176, 2005.

[195] P. Yue, C. Zhou, and J.J. Feng. Spontaneous shrinkage of drops and mass conservation in phase-field simulations. *J. Comput. Phys.*, 223(1):1–9, 2007.

[196] P. Yue, C. Zhou, and J.J. Feng. Sharp-interface limit of the Cahn–Hilliard model for moving contact lines. *J. Fluid Mech.*, 645(8):279, 2010.

[197] A. Yun, Y. Li, and J. Kim. A new phase-field model for a water–oil-surfactant system. *Appl. Math. Comput.*, 229:422–432, 2014.

[198] J. Zhang, D. M. Eckmann, and P. S. Ayyaswamy. A front tracking method for a deformable intravascular bubble in a tube with soluble surfactant transport. *J. Comput. Phys.*, 214(1):366–396, 2006.

[199] F. Zonta, C. Marchioli, and A. Soldati. Modulation of turbulence in forced convection by temperature-dependent viscosity. *J. Fluid Mech.*, 697:150–174, 2012.